Preferential Oxidation of Carbon Monoxide in Hydrogen-rich Gases over Supported Cobalt Oxide Catalysts

by

Thulani Mvelo Nyathi

BSc Chemistry & Biochemistry, University of Cape Town (2012)

BSc(Hons) Chemistry, University of Cape Town (2013)

Dissertation submitted to the University of Cape Town
in partial fulfilment of the requirements
for the degree of

MSc(Eng) in Chemical Engineering

Centre for Catalysis Research
Department of Chemical Engineering
University of Cape Town
South Africa

December 2015

“Learn from yesterday, live for today, hope for tomorrow. The important thing is not to stop questioning.”

_Albert Einstein

Declaration

I, Mr. Thulani Mvelo Nyathi, certify that this submission is my own, unaided work, except for the information obtained from literature sources and my prescribed supervisors. All sources of information have been adequately acknowledged and referenced. I have not received assistance from any other source in completing this submission.

Signature: Signed by candidate
Signature Removed

Date: **17 December 2015**

Mr. T. M. Nyathi

Acknowledgements

I would firstly like to thank God for the strength and drive which enabled me to complete this project. All of this would not have been possible without His will and grace.

A very special thanks goes to my supervisors, Prof. Michael Claeys and Dr. Nico Fischer, for giving me the opportunity to complete my degree under their supervision and also for their constant support, their knowledge and the time they dedicated to this project. I would like to also thank Dr. Andrew York from the Johnson Matthey Technology Centre (UK) for initiating a collaboration with Prof. Claeys and also for his constant advice throughout the duration of this work.

To the current and past members of Prof Claeys's research group (*i.e.,* 2014 – 2015); their assistance in the lab and constant motivation is greatly appreciated. I wish each of them the best of luck in the future.

Special thanks also goes to the National Research Foundation (NRF) for offering me the Scarce Skills Masters Scholarship and to Johnson Matthey for providing funding for the operational costs of the project. Additional funding from the NRF/DST Centre of Excellence in Catalysis Research (*c**change) via UCT's Chemical Engineering department is also greatly appreciated.

My gratitude also extends to the team in the Analytical Laboratory of the Chemical Engineering department for their assistance with H_2-TPR. I would also like to thank the team at the Centre for Imaging and Analysis of UCT for their assistance with TEM and EDX.

Most of all, I would like to thank my family back in Durban for their constant love and support throughout my schooling and varsity life. Without them, I would not be where I am today. I would also like to thank my girlfriend for her love, patience and support during these two years. Finally, I dedicate this dissertation to my late paternal grandfather and maternal grandmother who both past away this year (2015). I will forever love and miss them.

Conference Contributions

2015

T. Nyathi, N. Fischer, A. York and M. Claeys

"*Effect of crystallite size on the preferential oxidation of CO in H_2-rich gases over Co_3O_4/Al_2O_3 catalysts*"

Oral presented at the *"26th Annual Conference of the Catalysis Society of South Africa (CATSA)"*, Arabella Hotel & Spa, Kleinmond, South Africa.

**** Was the recipient of the Clariant Best Student Oral Presentation Award***

T. Nyathi, H. Kotze, N. Fischer, and M. Claeys

"*Effect of crystallite size on the preferential oxidation of CO in H_2-rich gases using γ-Al_2O_3-supported Co_3O_4 nano-catalysts*"

Poster presented at the *"2nd International Syngas Convention"*, organised by the *DST-NRF Centre of Excellence in Catalysis (c*change)*, Vineyard Hotel, Newlands, South Africa.

Synopsis

The preferential oxidation of CO (CO-PROX) has been identified as one route of further reducing the trace amounts of CO (approx. 0.5 – 1 vol%) in the H_2-rich reformate gas after the high- and low-temperature water-gas shift reactions. CO-PROX makes use of air to preferentially oxidise CO to CO_2, reducing the CO content to below 10 ppm while minimising the loss of H_2 to H_2O.

In this study, a Co_3O_4/γ-Al_2O_3 model catalyst was investigated as a cheaper alternative to the widely used noble metal-based ones. The CO oxidation reaction in the absence of hydrogen has been reported to be crystallite size-dependent when using Co_3O_4 as the catalyst. However, studies looking at the effect of crystallite size during the CO-PROX reaction are very few. Metal-support interactions also play a significant role on the catalyst's performance. Strong metal-support interactions (SMSI) in Co_3O_4/Al_2O_3 catalysts give rise to irreducible cobalt aluminate-like species. Under CO oxidation and CO-PROX reaction conditions, such strong interactions in a similar catalyst can have a negative effect on the performance of Co_3O_4 but can keep its chemical phase intact *i.e.,* help prevent the reduction of the Co_3O_4 phase.

The catalysts used to investigate these two effects (*i.e.,* crystallite size and metal-support interactions) were synthesised using the reverse micelle technique from which nanoparticles with a narrow size distribution were obtained. Certain properties of the microemulsions prepared were altered to obtain five catalysts with varying Co_3O_4 crystallite sizes averaging between 3.0 and 15.0 nm. Four other catalysts with different metal-support interactions were also synthesised by altering the method for contacting the support with the cobalt precursor. The crystallite size of Co_3O_4 in these four catalysts was kept in the 3.0 – 5.0 nm size range.

Catalytic tests for the first series of catalysts showed that the mass-specific CO oxidation activity increased with a decrease in the starting crystallite size of Co_3O_4. However, the surface area-specific CO_2 formation rate increased with an increase in the crystallite size up to 8.5 nm. Above 8.5 nm, the crystallites possess relatively few surface active sites due to their low mass-specific surface areas. *In situ* characterisation in the UCT-developed magnetometer and PXRD capillary cell instruments at temperatures between 50 and 350 °C revealed that at elevated temperatures the catalysts were partially reduced to metallic Co with CoO being the other cobalt

phase present. The formation of metallic cobalt resulted in the formation of methane and in the decrease of the CO_2 selectivity. Larger crystallites were reduced to a greater extent compared to smaller crystallites possibly due to the existence of weaker metal-support interactions in the catalysts with the large crystallites. Upon decreasing the reaction temperature to below 350 °C, both *in situ* techniques also revealed that all the catalysts were partially re-oxidised to CoO with no Co_3O_4 observed. The complete re-oxidation of the surface metallic Co species terminated the formation of methane and restored the exclusive conversion of CO to CO_2. It is possible that at the end of each experiment the catalysts possess crystallites with a double-shell structure *i.e.,* crystallites with a CoO core, a metallic Co inner-shell and a CoO outer-shell.

For the second series of catalysts, those that had SMSI were much harder to reduce to metallic Co as expected, with the methane yields observed barely reaching 20% at 350 °C (as opposed to reaching 100% as observed with the first series of catalysts). When decreasing the reaction temperature to below 350 °C, the CO oxidation activity over these catalysts was restored but was unexpectedly higher than the activity initially observed along the heating profile. The reason for this enhanced activity may be that the nanoparticles had segregated from the support along the heating profile as they were being partially reduced. The segregation weakened the metal-support interactions availing more active surface area. The catalysts with weaker metal-support interactions displayed higher mass-specific CO oxidation activities but were much easier to reduce to metallic Co and as a result, formed much more methane along the heating profile (*i.e.,* 50 - 350 °C). These catalysts were later partially re-oxidised at decreased reaction temperatures (*i.e.,* below 350 °C) and were also thought to have crystallites with a double-shell structure at the end of the tests.

Contents

List of Figures

List of Tables

Nomenclature

Abbreviations

3WV	Three-way valve
4WV	Four-way valve
BPR	Back pressure regulator
CO-PROX	Preferential oxidation of CO (carbon monoxide)
DFT	Density functional state theory
DOR	Degree of reduction
EDX	Energy-dispersive X-ray spectroscopy
fcc	Face-centred cubic
FIC	Flow indicator and control
GC	Gas chromatography
hcp	Hexagonal closed packed
H_2-TPR	Hydrogen temperature-programmed reduction
HRTEM	High resolution transmission electron microscopy
MFC	Mass flow controller
NTP	Normal temperature and pressure (298.15 K and 1.013 bar)
NV	Needle valve
PEGDE	Penta-ethyleneglycol-dodecylether
PIC	Pressure indicator and control
PONKCS	Partial or no known crystal structures
PR	Pressure regulator
PXRD	Powder X-ray diffraction
RWGS	Reverse water-gas shift
SMSI	Strong metal-support interactions
TCD	Thermal conductivity detector

TEM	Transmission electron microscopy
TIC	Temperature indicator and control
WGS	Water-gas shift
XRD	X-ray diffraction

Chemical formulas

Al_2O_3	Aluminium oxide (Alumina)
Ar	Argon
Au	Gold
CH_4	Methane
CeO_2	Ceruim dioxide
Co	Cobalt
CO	Carbon monoxide
$Co(NO_3)_2 \cdot 6H_2O$	Cobalt(II) nitrate hexahydrate
$Co(OH)_2$	Cobalt(II) hydroxide
CO_2	Carbon dioxide
Co_3O_4	Cobalt(II, III) oxide
$CoAl_2O_4$	Cobalt(II) aluminate
CoO	Cobalt(II) oxide
CuO	Copper(II) oxide
H_2	Molecular hydrogen
H_2O	Water
He	Helium
MnOOH	Manganese(III) oxyhydroxide
N_2	Molecular nitrogen
NH_3	Ammonia
Ni	Nickel
NiO	Nickel(II) oxide
O_2	Molecular oxygen

Pd	Palladium
Pt	Platinum
Rh	Rhodium
Ru	Ruthenium
SiC	Silicon carbide
SiO_2	Silicon dioxide (Silica)
ZrO_2	Zirconium dioxide

Notations

A	Area in chromatogram
d	Diameter, in nm
F	Response factor
H	Enthalpy, in kJ/mol or; external magnetic field, in kOe or T
k_B	Boltzman constant, $1.38065048 \cdot 10^{-16}$ erg/K
M	Sample magnetisation, in emu or; mass loading, in g
M_{rem}	Remnant magnetisation, in emu
M_S	Saturation magnetisation, in emu
n	Molar amount or; molar flow rate, in mol/min
N_A	Avogadro's number, $6.022141 \cdot 1023$ mol^{-1}
S	Selectivity, in %
T	Temperature, in °C or K
T_{50}	Temperature for a CO conversion of 50%, in °C
T_C	Curie temperature, in K
$T_{Hüttig}$	Hüttig temperature, in K
$T_{melting}$	Melting temperature, in K
T_N	Néel temperature, in K
T_{Tamman}	Tamman temperature, in K
TOF	Turn over frequency, in s^{-1}
X	Conversion, in %

Y	Yield, in %

Greek notations

γ	Magnetic material displaying remnant magnetisation, wt.-%
θ	Diffraction angle, in °
λ	Wavelength, in Å
ρ	Density, in g/cm^3
σ	Mass specific magnetisation, in emu/g or; standard deviation, in nm
ω	Water to surfactant molar ratio

Chapter 1: Introduction

Hydrogen (H_2) is the main component of the universe, more specifically it represents 74 wt% of the sun. However the sun's hydrogen disappears every second by fusion to form helium and energy, and part of this energy reaches the earth (Greenwood & Earnshaw, 1984). On Earth, the main processes for producing hydrogen are coal gasification (Kaneko *et al.*, 2001) and steam reforming of hydrocarbons and alcohols (Armor, 1999; Bion *et al.*, 2008). Hydrogen is then used for example in large-scale processes including the Haber-Bosch process, Fischer-Tropsch synthesis and also for the small-scale operation of proton exchange membrane- and polymer electrolyte membrane fuel cells (PEMFC). Steam reforming, for example, produces significant amounts of carbon monoxide (CO). The decrease in the CO content is important for the operation of PEMFC's where hydrogen of high purity is required (Vielstich *et al*., 2003).

In industry, the CO content present in the reformate gas is reduced via the water-gas shift (WGS) reaction which consequently increases the hydrogen and carbon dioxide content. After the application of the WGS process, the CO content in the hydrogen-rich WGS product remains in the 0.5 – 1 vol% range as shown in Figure 1. This amount of CO has shown to be poisonous to the platinum catalyst on the anode side of PEMFC's by preventing the dissociative adsorption of H_2 and the subsequent charge transfer process (Rodrigues *et al.*, 1997). Now great effort is going towards finding ways of further reducing this CO amount to below 10 ppm.

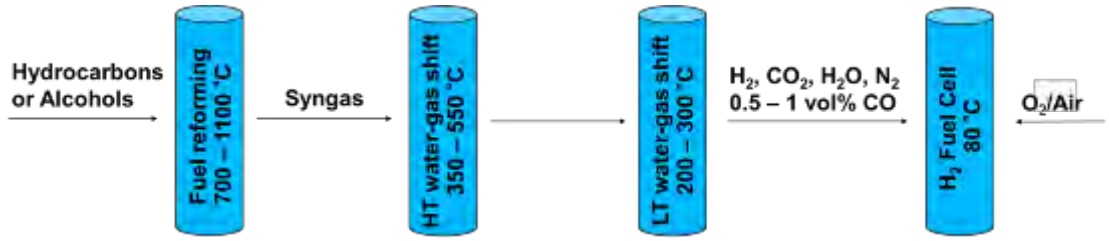

Figure 1.1*: The processes involved in the production of H_2-rich reformate gas leading to a typical PEMFC operation unit.*

Several processes have been proposed and evaluated for this purpose *viz.,* pressure swing gas adsorption, H_2-selective membrane separation, selective CO methanation and preferential oxidation of CO (CO-PROX) (Mishra & Prasad, 2011; Park *et al*., 2009). Separation of H_2 from the reformate gas mixture using pressure swing adsorption (PSA) is based on a changing pressure gradient. The gases are either adsorbed on a single adsorber or multiple adsorbers which then means that PSA can either be performed as a batch process or as a continuous flow process, respectively (Mishra & Prasad, 2011; Sircar & Golden, 2000). In this process, high pressures are used in order to obtain high CO removal efficiencies. The high pressures needed make the design process complicated and also makes the process more expensive.

H_2-selective membranes are also an efficient method for the removal of CO. This process makes use of a semi-permeable membrane which should ideally allow H_2 to go through and prevent the permeation of the other gases. Relatively high pressures are required and currently, the best membranes are Pd-based ones and this then makes the use of this membrane technology expensive (Adhikari & Fernando, 2006; Sakamoto *et al.*, 1996). Also these membranes tend to undergo embrittlement and can also form hydrides which results in the loss of selectivity (Adams & Mickalonis, 2007).

Selective methanation is also among the widely explored methods and in this process, the hydrogen present in the reformate gas is used to remove the CO by converting it to CH_4. The usual catalysts used here are either ruthenium- or nickel-based (Brown Jr. *et al.*, 1960; Rehmat & Randhava, 1970). There are a few main drawbacks with this process. The first being that to convert the CO to CH_4, hydrogen is required. This reduces the amount of hydrogen which could potentially be used in the PEMFC since three moles of H_2 are required to remove one mole of CO. The second drawback is that since there is CO_2 present in relatively higher amounts than CO in the H_2-rich reformate, this presents selectivity issues because CO_2 can also undergo

methanation. The methanation of one mole of CO_2 requires four moles of H_2, which then increases the penalty altogether (Golunski, 1998). Even though the methanation of CO can be performed at slightly lower temperatures, the temperature window for achieving complete methanation of CO only is very narrow (Edwards *et al.*, 1998).

The preferential oxidation of CO (CO-PROX) shown in Figure 1.2 involves the oxidation of CO to CO_2 in the presence of hydrogen (Mishra & Prasad, 2011; Park *et al.*, 2009). This is done over a heterogeneous catalyst either a metal- or metal oxide-based. Metal oxides are preferred over noble metal-based catalysts as these are cheap and readily available but based on activity and stability, noble metals have been shown to be superior over metal oxide-based. Nonetheless, CO-PROX has been identified as the most cost-effective industrial process among all four processes already mentioned (Gray & Petch, 2000). Relatively low operational pressures (*i.e.,* 1 – 2 bar) and temperatures (80 – 250 °C) are required for CO-PROX. Since CO-PROX does not make use of hydrogen to convert CO, this makes it a more preferable process over selective methanation. (Edwards *et al.*, 1998; Mishra & Prasad, 2011).

However, CO-PROX requires a highly selective (heterogeneous) catalyst to oxidise CO to CO_2 with minimal loss of H_2 through its oxidation to water. Also, finding a cheap, active and stable catalyst for this reaction is of great importance as the catalyst must remain active and stable over a wide temperature range *i.e.,* 80 – 250 °C (Huang *et al*., 2009). This is because CO-PROX is the intermediate reaction between the low temperature WGS process, which is operated between 200 and 250 °C; the operation of a PEMFC, which is operated approximately at 80 °C as shown in Figure 1.2 (Huang *et al*., 2009).

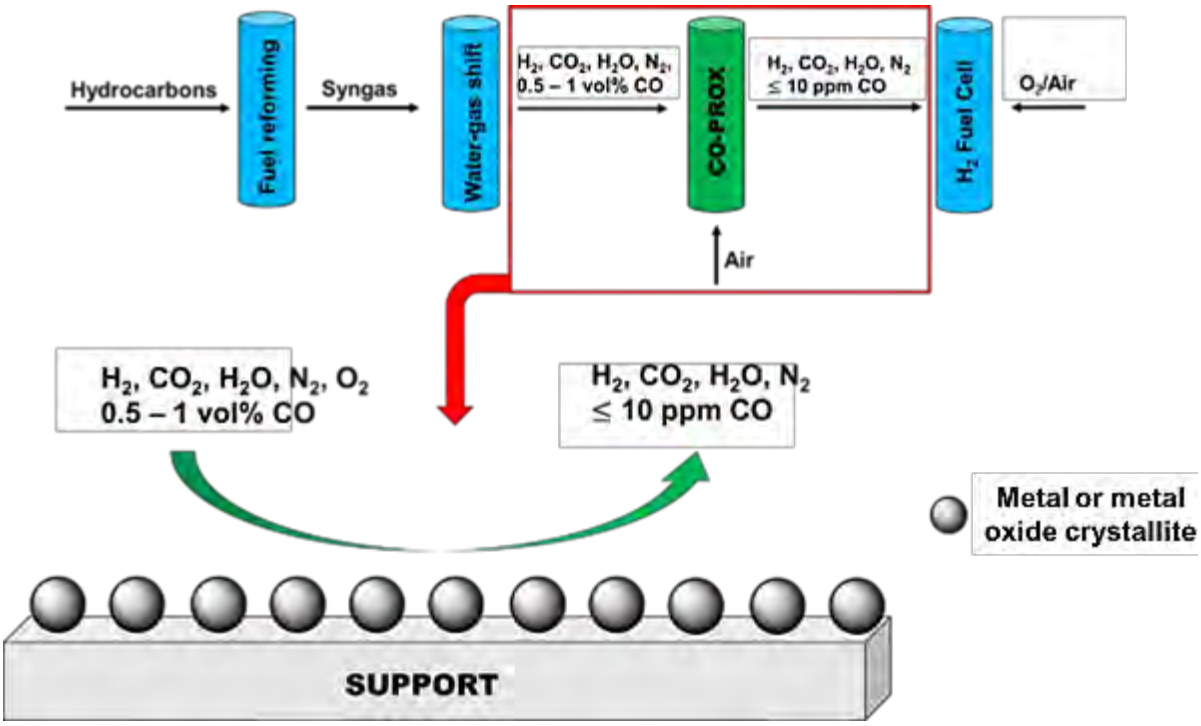

Figure 1.2: *The processes involved in the production of H_2-rich reformate gas but now including a CO-PROX unit between a typical WGS unit and a PEMFC unit.*

The study presented herein aimed at investigating a model $Co_3O_4/\gamma\text{-}Al_2O_3$ catalyst as a cheaper and promising candidate for the CO-PROX reaction. Specifically, the effect of the crystallite size of Co_3O_4 on the mass- and surface area-specific reaction rates was investigated. Cuenya & Behafarid (2015) classified the CO oxidation (in the absence of hydrogen) as being a structure-sensitive reaction. Studies by Liu *et al.* (2013) and Wang *et al.* (2005) have shown that an increase in the mass-specific activity can be expected when the crystallite size of Co_3O_4 is decreased. Crystallite size-effects on the surface area-specific rates were not reported. Iablokov (2011) performed a more in-depth investigation on the effect of Co_3O_4 crystallite size during CO oxidation. He concluded that Co_3O_4 crystallites with a 5 – 8 nm size showed the highest surface area-specific rates amongst crystallites with varying sizes between 3 and 12.5 nm. However, crystallites with a size below 6 nm generally displayed higher mass-specific rates due to their relatively high exposed surface area per gram of catalyst. Studies investigating the effect of the crystallite size of Co_3O_4 under CO-PROX conditions are not known to date.

The effect of metal-support interactions on the catalytic performance and reducibility of the Co_3O_4/Al_2O_3 model catalysts was also investigated. The presence of strong metal-support interactions in $Co_3O_4/\gamma\text{-}Al_2O_3$ is generally associated with low reducibility of the Co_3O_4 phase

(Arnoldy & Moulijn, 1985; Fischer *et al.*, 2012; Sirijaruphan *et al.*, 2003; Wang *et al.*, 2006). Wang *et al.* (2006) showed that by altering the metal-support interactions in three Co_3O_4/γ-Al_2O_3 catalysts, the CO oxidation activity (in the absence of hydrogen) of each catalyst was affected. Strong metal-support interactions (SMSI) decreased the CO oxidation activity. Under the H_2-rich CO-PROX environment, Zhao and co-workers (2008) reported that the presence of SMSI in a Co_3O_4/γ-Al_2O_3 catalyst offers resistance towards the reduction of the Co_3O_4 phase but these interactions decrease the CO oxidation activity of the catalyst.

The supported Co_3O_4 catalysts investigated in this study were synthesised using the reverse micelle technique as it is known for producing nanoparticles with a narrow size distribution (Eriksson *et al.*, 2004). The catalysts were tested and characterised *in situ* using novel in-house developed instruments *viz.,* the magnetometer (Claeys *et al.*, 2010; Fischer *et al.*, 2014) and powder X-ray diffraction capillary cell (Claeys & Fischer, 2013; Fischer *et al.*, 2014). These complementary *in situ* techniques allowed for on-line monitoring of the changes in the crystallite size and bulk chemical phases within the catalyst during the CO-PROX reaction as a function of temperature while kinetic data were recorded.

Chapter 2: Literature Review

2.1. Industrial applications of CO-PROX

The preferential oxidation of CO in H_2-rich streams dates back to the 1960's where it was first proposed as a commercial process for purifying H_2 for the Haber-Bosch process (*i.e.,* ammonia synthesis). Before CO-PROX, industrial companies including Mississippi Chemical Corporation for example, were employing the methanation process for removing CO by converting it to CH_4 (Brown Jr. *et al.*, 1960; Brown & Green, 1963). Figure 2.1 is the process flow diagram for Mississippi Chemical Corporation's H_2 manufacturing and clean up units utilised upstream of the ammonia synthesis plant. The H_2-rich gas for the ammonia synthesis was obtained via steam reforming of natural gas to syngas at 871 °C (1600 °F). The syngas was then taken through a two-step CO conversion process (*i.e.,* water-gas shift) and after each of the two steps, the gas was cooled to approximately 88 °C (190 °F) and then the CO_2 formed was subsequently removed by absorption in monoethanolamine.

The resulting CO concentration (approximately 2 – 4 vol%) was further reduced via methanation over either a nickel- or ruthenium-based catalysts, or by using ammonia synthesis catalysts (Brown Jr. *et al.*, 1960; Brown & Green, 1963). During the methanation process, CO reacted with H_2 to form CH_4 at approximately 316 °C (600 °F). This process did reduce the CO levels, however, there was a penalty of 3 units of H_2 for every unit of CO converted (see Equation 2.1). Also after employing the absorption processes for the removal of CO_2, there would still be a significant amount of the CO_2 still in the methanation feed, and so the CO_2 would also react with the hydrogen to form methane (see Equation 2.2). The conversion of CO_2 to methane had a negative effect on the conversion of CO to methane and further decreased the H_2 concentration (Brown Jr. *et al.*, 1960; Brown & Green, 1963).

$$CO(g) + 3H_2(g) \rightarrow CH_4(g) + H_2O(g) \qquad \Delta H^o_{298K} = -205.8\ \text{kJ.mol}^{-1} \qquad \textbf{Equation 2.1}$$

$$CO_2(g) + 4H_2(g) \rightarrow CH_4(g) + 2H_2O(g) \qquad \Delta H^o_{298K} = -164.6\ \text{kJ.mol}^{-1} \qquad \textbf{Equation 2.2}$$

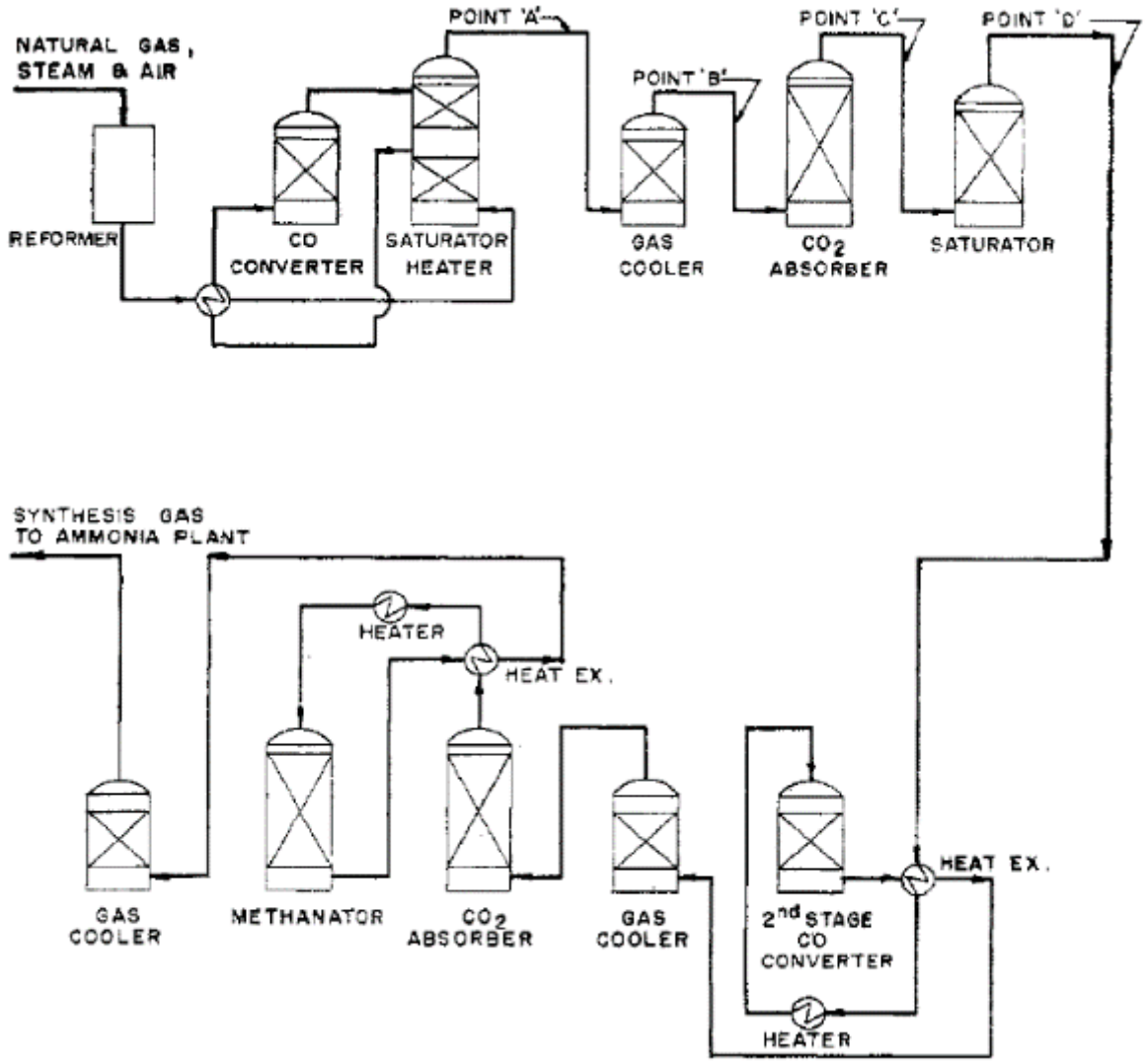

Figure 2.1: *Mississippi Chemical Corporations' process flow diagram for the production and clean-up of H_2 for the ammonia synthesis. [From Brown Jr. et al. (1960)].*

Engelhard Industries Inc. investigated CO-PROX as a cheaper alternative to the methanation process for the reduction of CO in the H_2-rich reformate gas. Laboratory and pilot plant studies were conducted where they looked at different O_2/CO ratios, different concentrations of H_2O and CO_2, and space velocities just to mention a few parameters. For the CO-PROX process, different platinum-group metals as mono- and bi-metallic catalysts were investigated (Brown Jr. *et al.*, 1960; Brown & Green, 1963; Cohn, 1965). For all these catalysts they found that

above 177 °C (350 °F), the catalysts started to lose their CO_2 selectivity even when the O_2 conversion was increasing. They attributed this to the onset of H_2 oxidation to water. There was also evidence of the reverse water-gas shift reaction (see Equation 2.3) taking place which increased the CO concentration. Therefore, Engelhard went on to propose a two-stage CO-PROX clean-up process which would offer good temperature and CO_2 selectivity control. The process was called the Selectoxo™ process (Brown Jr. *et al.*, 1960; Brown & Green, 1963; Cohn, 1965).

$$\boldsymbol{CO_2(g) + H_2(g) \rightarrow CO(g) + H_2O(g)} \qquad \boldsymbol{\Delta H^o_{298K} = 41.2\ kJ.mol^{-1}} \qquad \textbf{Equation 2.3}$$

Figure 2.2 shows their process flow diagram which includes the H_2 manufacturing and clean-up units. Note that inclusion of the two-stage CO-PROX units reduced the number of water-gas shift units from two to one (see Figure 2.1 which shows two of these units) and also that the CO-PROX reactors were very small compared to the ones used for water-gas shift and for methanation (see also Figure 2.1). They proposed that the first stage was to be performed within the 120 – 177 °C (250 – 350 °F) temperature range and in this range, 90% of the CO would be removed using a 1.5:1 O_2/CO ratio. In the second stage, a 1:1 O_2/CO ratio and a temperature of 160 °C (320 °F) could be used to further reduce the CO levels to below 10 ppm (Brown Jr. *et al.*, 1960; Brown & Green, 1963; Cohn, 1965).

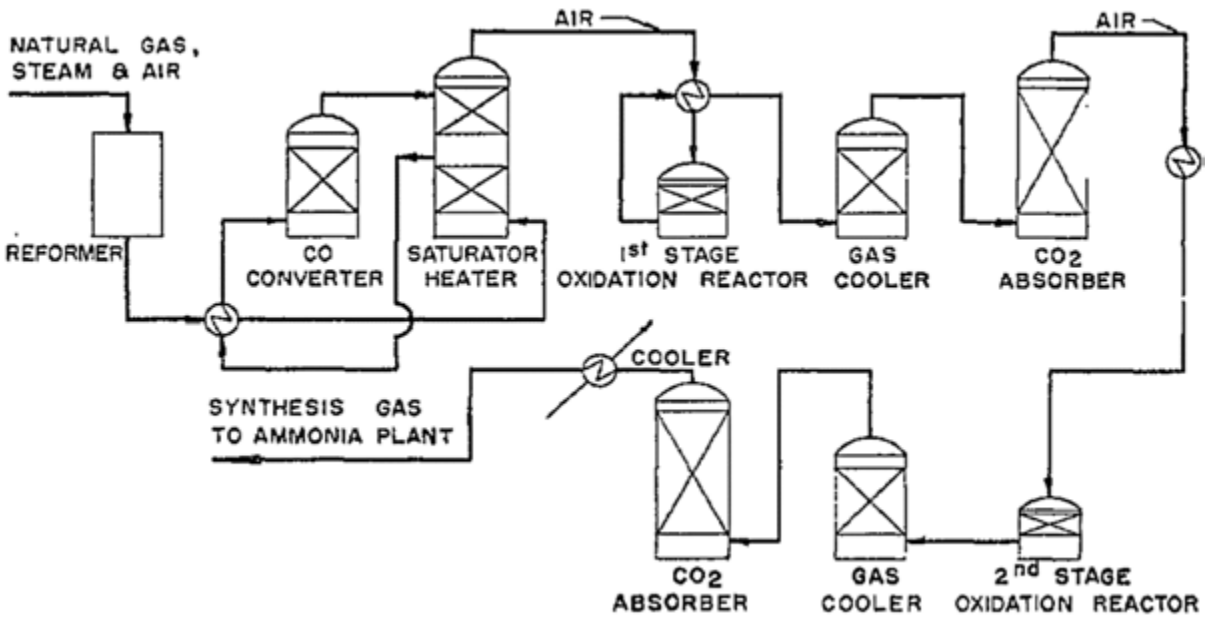

Figure 2.2: *Engelhard Industries Inc. process flow diagram showing their H_2 production and clean-up units. More importantly, this flow diagram shows the proposed two-stage CO-PROX units for replacing the methanation unit used at Mississippi Chemical Corporation. [From Brown Jr. et al. (1960)].*

In the 1980's, Johnson Matthey invented a new fuel processor for the manufacture of H_2 for solid polymer fuel cells (SPFC's). This reformer was known as the HotSpot™ Fuel Processor (Golunski, 1998). Methanol was chosen as the fuel but other hydrocarbon fuels can also be used in the place of methanol. Nonetheless, methanol was a better starting fuel because it has a high atomic H/C ratio and it is produced from renewable resources. Methanol itself is a relatively clean fuel in its composition and production; more importantly, methanol reforming (using their technology) produces about 2 – 3 vol% of CO at steady-state conditions (Golunski, 1998; Edwards *et al.*, 1998). This meant that the water-gas shift process was no longer required for further reducing this CO concentration but instead, other methods were considered *viz.,* selective methanation, selective membranes and CO-PROX.

Out of these three, CO-PROX was chosen to be the best method in terms of both cost effectiveness and clean-up efficiency (Gray & Petch, 2000). Figure 2.3 shows their process flow diagram which includes among other things, the methanol fuel processing unit and the CO clean-up unit, respectively. The CO clean-up unit is 40% of the size of the fuel processing unit and consists of multiple small reactors (not shown in this figure) as opposed to having one big reactor. Between the reactors, the reformate product is cooled before being taken to the next reactor. The CO clean-up unit was designed as such because the temperature control proved to

be difficult when the CO clean-up was done in a single reactor which in turn, decreased its efficiency. The current design of the CO clean-up unit is called the Demonox™ system and makes it possible to decrease the CO concentration to below 5 – 10 ppm (Edwards *et al.*, 1998; Gray & Petch, 2000).

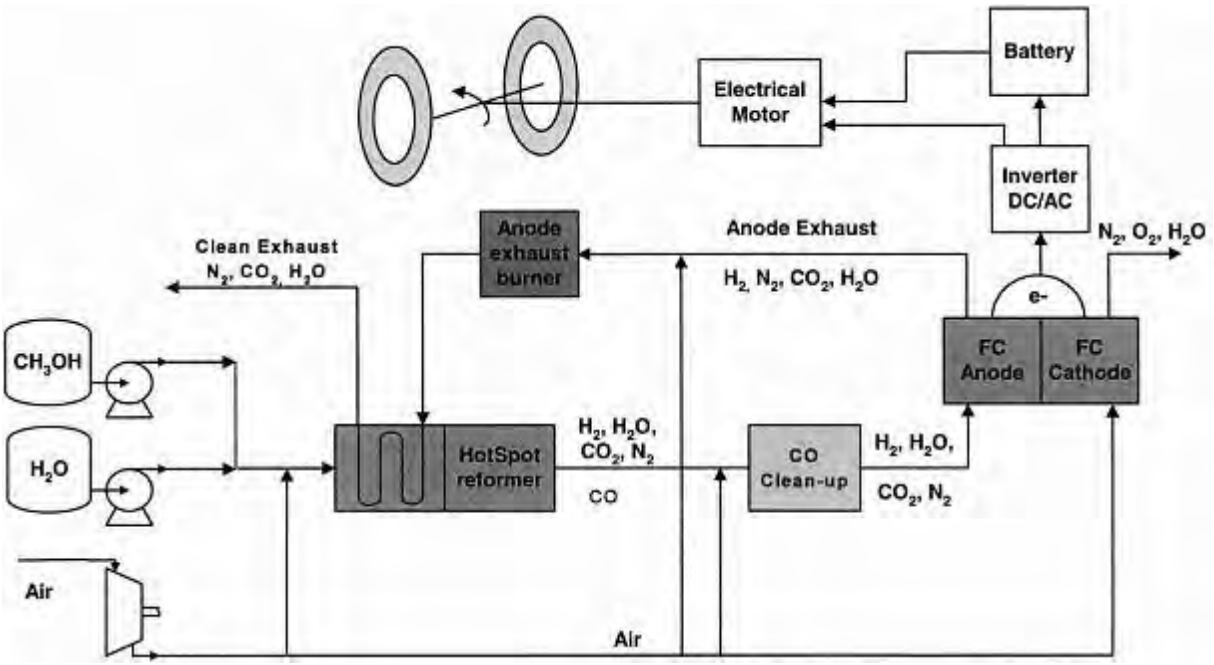

Figure 2.3: *Johnson Matthey's process flow diagram including their methanol HotSpot™ Fuel processing unit and a CO clean-up unit consisting of multiple CO-PROX reactors upstream of the fuel cell unit. Note that there is no WGS process unit after the reformer. [From Edwards et al. (1998)].*

2.2. Selectivity in CO-PROX

2.2.1. CO oxidation and H_2 oxidation

The hydrogen-rich reformate gas produced after the low-temperature WGS process typically has 0.5 – 1.0 vol% CO, 15 – 25 vol% CO_2, 15 – 30 vol% H_2O, 40 – 75 vol% H_2 and 0 – 25 vol% N_2 (Ghenciu, 2002). The O_2 co-fed as the species that should convert CO to CO_2 can also oxidise H_2 to H_2O at high enough temperatures which then reduces the CO_2 selectivity and the CO conversion. Both the CO oxidation and H_2 oxidation are exothermic reactions as shown by Equations 2.4 and 2.5 but CO oxidation takes place at relatively low temperatures. In principle, this means that conversions and selectivities close to 100% could be obtained at temperatures lower than those required for the oxidation of H_2. Over most catalysts, the optimal temperature range for obtaining very high CO conversions and CO_2 selectivities is 80 – 177 °C (Mishra & Prasad, 2011). However, it should be noted that this range could be wider or narrower depending on the chemical and physical characteristics of the catalyst being used and how these characteristics influence its performance.

$$2CO(g) + O_2(g) \rightarrow 2CO_2(g) \qquad \Delta H^o_{298K} = -283.0\ \text{kJ.mol}^{-1} \qquad \textbf{Equation 2.4}$$

$$2H_2(g) + O_2(g) \rightarrow 2H_2O(g) \qquad \Delta H^o_{298K} = -241.8\ \text{kJ.mol}^{-1} \qquad \textbf{Equation 2.5}$$

2.2.2. Reverse water-gas shift and methanation

The oxidation of CO and H_2 may not be the only reactions taking place during CO-PROX. The reverse water-gas shift reaction (RWGS) shown as Equation 2.3 (see section 2.1) is also possible leading to the formation of CO and H_2O from CO_2 and H_2. It has been reported that this reaction does take place usually after a full conversion of CO has been reached (Brown Jr. *et al.*, 1960; Woods *et al.*, 2010; Yung *et al.*, 2008). This may suggest that the observed increase in water is a cumulative result of the contributions from the H_2 oxidation reaction and the RWGS reaction as shown in Figure 2.4. However, the extent to which the RWGS reaction occurs is quite little according to the results reported by Woods *et al.* (2010) shown in Figure

2.4. Therefore, its contribution to the water concentration is minor. The RWGS reaction is observed in the temperature range from 177 – 250 °C above which both the levels of CO and CO_2 start to decrease much rapidly. This steep decrease in the CO and CO_2 levels above 250 °C is a result of the hydrogenation of CO (see Equation 1) forming methane (CH_4) which consequently decreased the CO_2 selectivity.

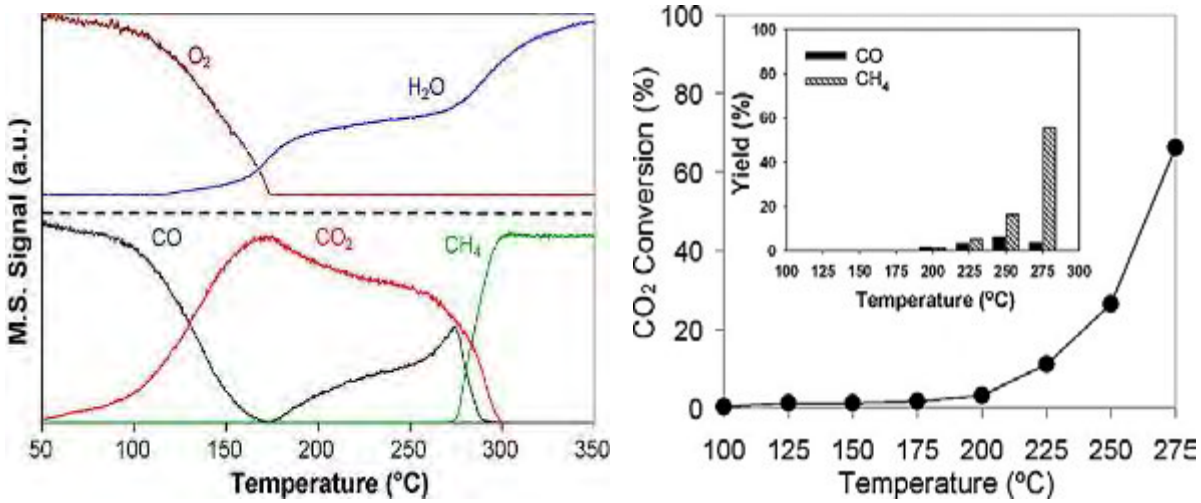

Figure 2.4: ***(left)*** *GC-MS CO-PROX product spectrum. Reaction conditions: 10 wt.-% CoO_x/CeO_2, 1 vol% CO, 1 vol% O_2, 60 vol% H_2 in He.* ***(right)*** *The extent to which the RWGS and methanation take place over the same catalyst. Reaction conditions: 1% CO_2, 60% H_2 in He. [Both from Woods et al. (2010)].*

2.3. Catalysts used in CO-PROX

2.3.1. Noble metal catalysts

For many years CO-PROX has been performed over noble metal-based catalysts including Pt (Cohn, 1965; Oh & Sinkevitch, 1993; Wootsch *et al.*, 2004), Rh (Kim *et al.*, 2009; Oh & Sinkevitch, 1993), Ru (Kim *et al.*, 2009; Oh & Sinkevitch, 1993) and Au (Ko *et al.*, 2006; Luengnaruemitchai *et al.*, 2004). These catalysts exhibit high catalytic activity and selectivity under CO-PROX reaction conditions. Their catalytic activity and selectivity both depend on the

type of metal used, the metal loading and their dispersion. The selectivity of these catalysts is further affected by the relative amounts of CO, O_2 and H_2 adsorbed on the metal surface since the mechanism of the CO-PROX reaction over metal catalysts has been reported to go via a competitive Langmuir-Hinshelwood mechanism (Kim & Lim, 2002; Wootsch *et al*., 2004). It is named so because all the reactants compete for active sites on the catalysts.

This kind of mechanism is usually observed when the metal particles are supported on an irreducible support material like γ-Al_2O_3. At low temperatures (below 177 °C), the CO:H_2 ratio on the metal surface is high and so this enhances both the conversion of CO and the selectivity towards the formation of CO_2. At high temperatures (above 177 °C), this ratio decreases and the conversion of CO decreases as well as the selectivity towards CO_2 formation (Wootsch *et al*., 2004). This temperature-dependent adsorption behaviour is depicted in Figure 2.5.

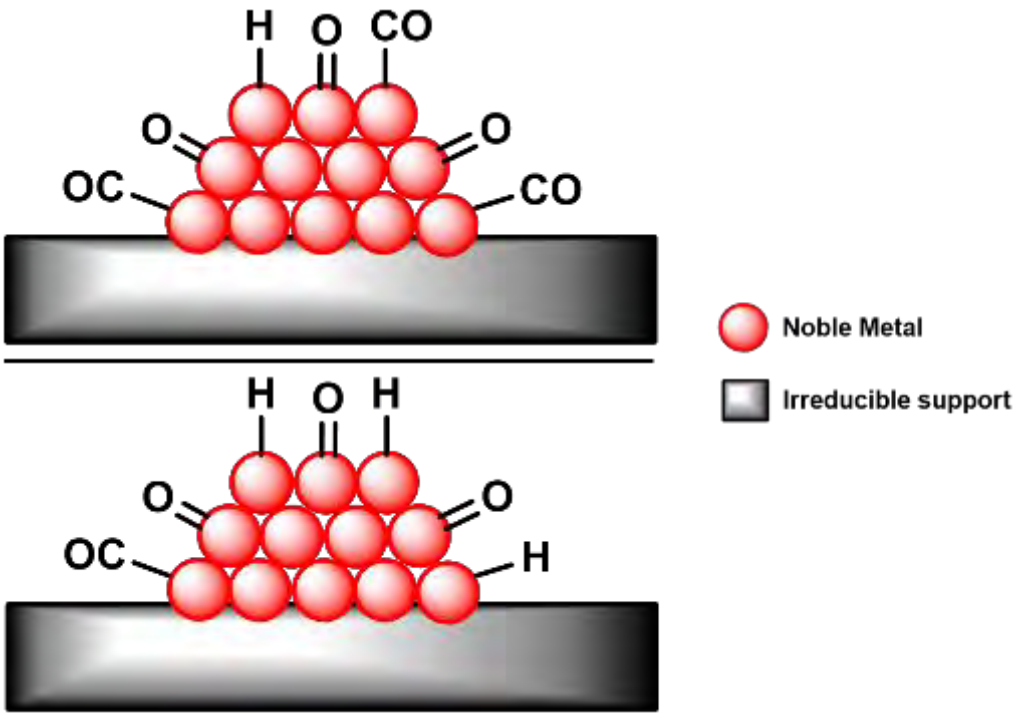

Figure 2.5: *Surface concentrations of CO, O and H at (**top**) low temperatures (< 177 °C) and at (**bottom**) high temperatures (> 177 °C) over a noble metal-based catalyst supported on an irreducible metal oxide.*

When noble metal particles are deposited on reducible support materials *viz.,* CeO_2 or ZrO_2, a different mechanism is observed which is referred to as a non-competitive Langmuir-Hinshelwood mechanism (Kim & Henkelman, 2013; Cargnello *et al.*, 2013; Wootsch *et al*., 2004). In this mechanism, the support material actually takes part in the oxidation by supplying its lattice oxygen present on its surface to the metal with an adsorbed CO molecule. In this way, the adsorption and dissociation processes for O_2 have a minor contribution to the overall reaction rate and O_2 or O competes to a lesser extent with CO (and/or H_2) for active sites. The support material is also seen as a promoter for the metal as it assists in the oxidation of CO (Wootsch *et al*., 2004). When lattice oxygen leaves the support, its surface is momentarily left partially reduced, however, the oxygen present in the feed re-oxidises the surface and regenerates it for another catalytic cycle. This kind of redox cycle observed on the surface of the support is known as the Mars-van Krevelen mechanism (Mars & van Krevelen, 1954; Perti *et al*., 1985) and is depicted in Figure 2.6. The oxidation of CO over noble metal catalysts supported on reducible support materials occurs at the interface between the support and the metal particle.

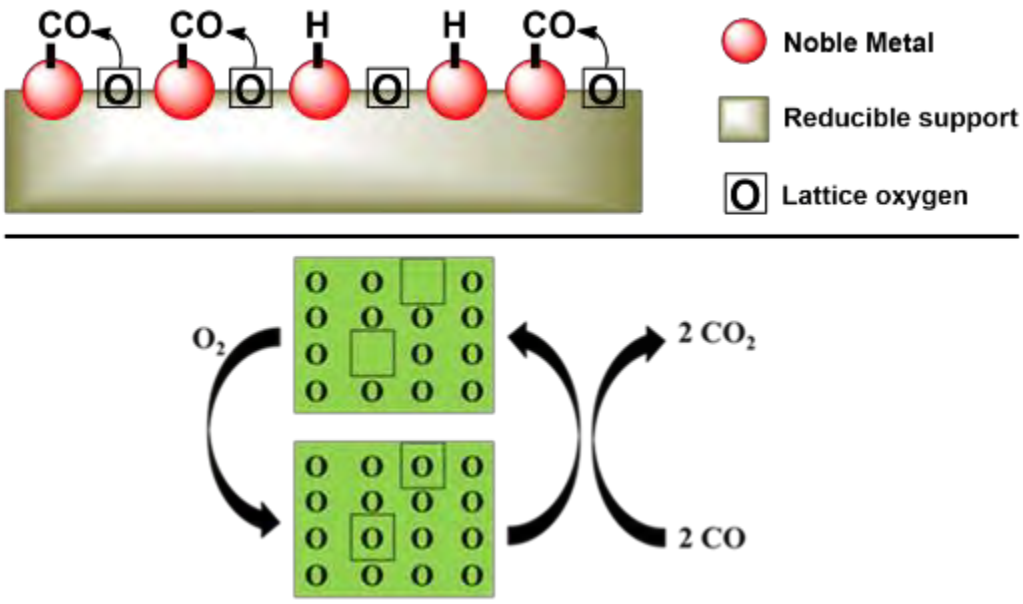

Figure 2.6: *(**top**) Non-competitive Langmuir-Hinshelwood mechanism for CO-PROX where CO adsorbed on a metal active site gets oxidised by oxygen species emanating from the reducible support material. (**bottom**) Mars-van Krevelen-type mechanism observed on the surface of the support.*

There has been use of bimetallic catalysts in CO-PROX and in such systems, the so-called bimetallic mechanism is observed. In this mechanism, the one metal adsorbs CO (or H) and the other metal adsorbs O; the proximity of the two metal atoms with adsorbed species becomes one of the factors controlling the reaction rate (Watanabe & Motoo, 1975; Yajima *et al.*, 2004). This mechanism is also illustrated in Figure 2.7. Parinyaswan *et al.* (2006) investigated the effect of the Pt:Pd ratio in their Pt-Pd/CeO_2 catalyst and observed that increased activity and selectivity is achieved when the Pt:Pd ratio is minimised *i.e.,* when the amount of Pd is greater than that of Pt. Naknam *et al.* (2007) investigated the effect of adding gold onto platinum catalysts and observed that adding gold improved the oxidation of CO in excess hydrogen at low temperatures. Yan *et al.* (2004) improved the activity and selectivity of their Pt/γ-Al_2O_3 catalysts by adding varying amounts of cobalt.

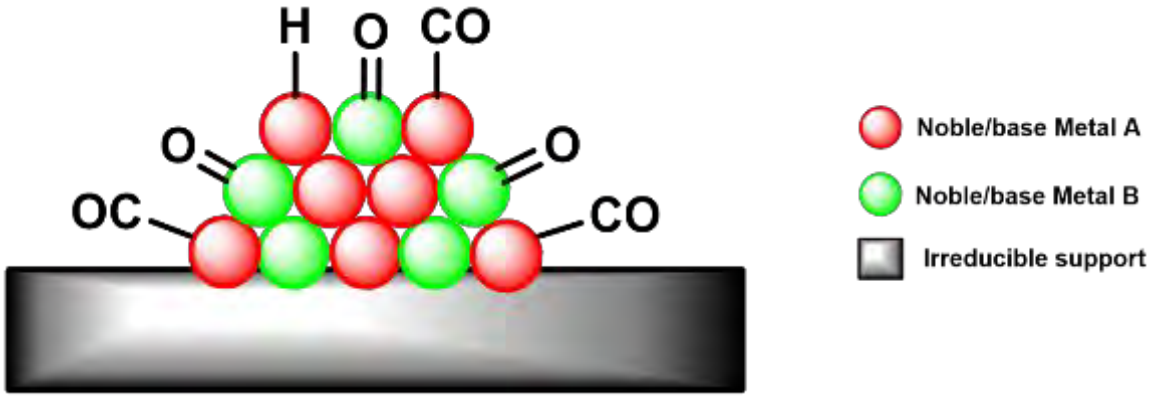

Figure 2.7: *Bimetallic mechanism observed for CO-PROX over bimetallic-based catalysts. Notice that metal A only adsorbs CO and H whereas metal B only adsorbs O.*

2.3.2. Base metal oxide catalysts

Metal oxide-based catalysts have been viewed as potential replacements of noble metal-based catalysts since the latter is expensive and generally limited in its availability (Mishra & Prasad, 2011; Park *et al*., 2009; Varghese *et al.*, 2012). The oxidation of CO, using base metal oxide catalysts, is thought to go via the Mars-van Krevelen mechanism (Mars & van Krevelen, 1954; Perti *et al*., 1985). This mechanism involves the active participation of the catalyst in the reaction *i.e.,* the supported nanoparticles offer adsorption sites for the substrate CO and also

provide the active oxygen species for oxidising it. If the catalyst is supported on an irreducible catalyst, the oxidation can be expected to take place purely on the surface of the base metal oxide catalyst. However, if the catalyst is supported on a reducible support, the oxidation can once again be expected to occur at the catalyst-support interface (Kang *et al*., 2003).

Extensive studies have been performed using copper oxide (CuO) catalysts supported and/or promoted by support materials like ceria (CeO_2) (Gamarra *et al.*, 2007; Park *et al.*, 2004 and Ratnasamy *et al.*, 2004), zirconia (ZrO_2) (Ratnasamy *et al.*, 2004), γ-alumina (γ-Al_2O_3) (Park *et al.*, 2004) and cobalt oxide (Co_3O_4) (Varghese *et al.*, 2012). These copper oxide catalysts have been shown to have very good activity and selectivity for CO-PROX at low temperatures (below 177 °C) but exhibit a decline in the CO_2 selectivity at higher temperatures due to the dominance of the H_2 oxidation reaction (as seen with the noble metal-based catalysts). The studies conducted using copper oxide-based catalysts focused mostly on the effect of the support material used. As seen with noble metal-based catalysts, reducible supports supply the oxygen species required to oxidise the CO molecules adsorbed on Cu ions whereas irreducible supports do not part-take in the reaction (Gamarra *et al.*, 2007; Ratnasamy *et al.*, 2004).

Other studies have focused on the various deactivation mechanisms of CuO-based catalysts, for instance, the effect of CuO reduction to metallic Cu on the catalytic performance under CO-PROX conditions. It has been observed that CuO tends to reduce at higher temperatures to metallic Cu (Gamarra *et al.*, 2007; Teng *et al.*, 1999). Gamarra *et al.* (2007) reported that the onset of CuO reduction to Cu_2O could be directly correlated with the onset of H_2 oxidation at 400 K as shown in Figure 2.8. Further CuO (and/or Cu_2O) reduction to metallic Cu resulted in increased water formation. It is worth mentioning that the formation of methane was not observed during this experiment. A study done by Marbán *et al.* (2009) identified sintering and the formation of surface carbonates as a deactivation mechanism of CeO_2-supported CuO catalysts.

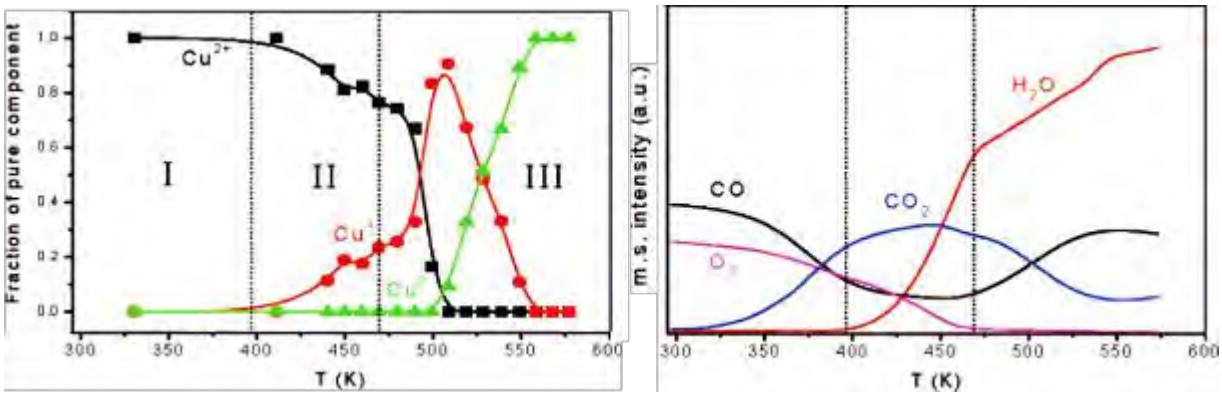

Figure 2.8: *(**left**) Cu ions identified as a function of temperature during in situ XANES CO-PROX experiments. (**right**) CO-PROX product spectrum obtained from online GC-MS analysis. [Both from Gamarra et al. (2007)].*

The other base metal oxide which has recently been looked for use in CO-PROX is cobalt(II, III) oxide *i.e.,* Co_3O_4. This is because Co_3O_4 has been shown very good catalytic activity for the CO oxidation reaction in the absence of hydrogen (Liu *et al.*, 2013; Teng *et al.*, 2011; Wang *et al.*, 2005). Co_3O_4 has a normal spinel structure with two Co^{3+} and one Co^{2+} species (Jansson *et al.*, 2002; Omata *et al.*, 1996) and this makes it a good oxidation catalyst since it can attain different oxidation states in fulfilment of the Mars-van Krevelen cycle. DFT studies (Broqvist *et al.*, 2002; Wang *et al.*, 2012) as well as experimental *ex situ* and *in situ* spectroscopic techniques *viz.,* XPS (X-ray photoelectron spectroscopy), XANES (X-ray Absorption Near-Edge Structure), XRD (X-ray diffraction) (Jansson *et al.*, 2002; Omata *et al.*, 1996) have been performed so to offer insights on the kind of active species involved in the oxidation of CO in the absence of hydrogen. The studies revealed that the cobalt species mostly responsible for the oxidation of CO is Co^{3+}. This species plays an important role in strongly adsorbing CO compared to Co^{2+} as illustrated in Figure 2.9 and also rapidly releases its neighbouring oxygen for oxidising the adsorbed CO (Broqvist *et al.*, 2002). This result then implies that an increase in the number of Co^{3+} ions on the catalysts surface would enhance the catalytic performance of cobalt oxide catalysts (Jansson *et al.*, 2002; Omata *et al.*, 1996).

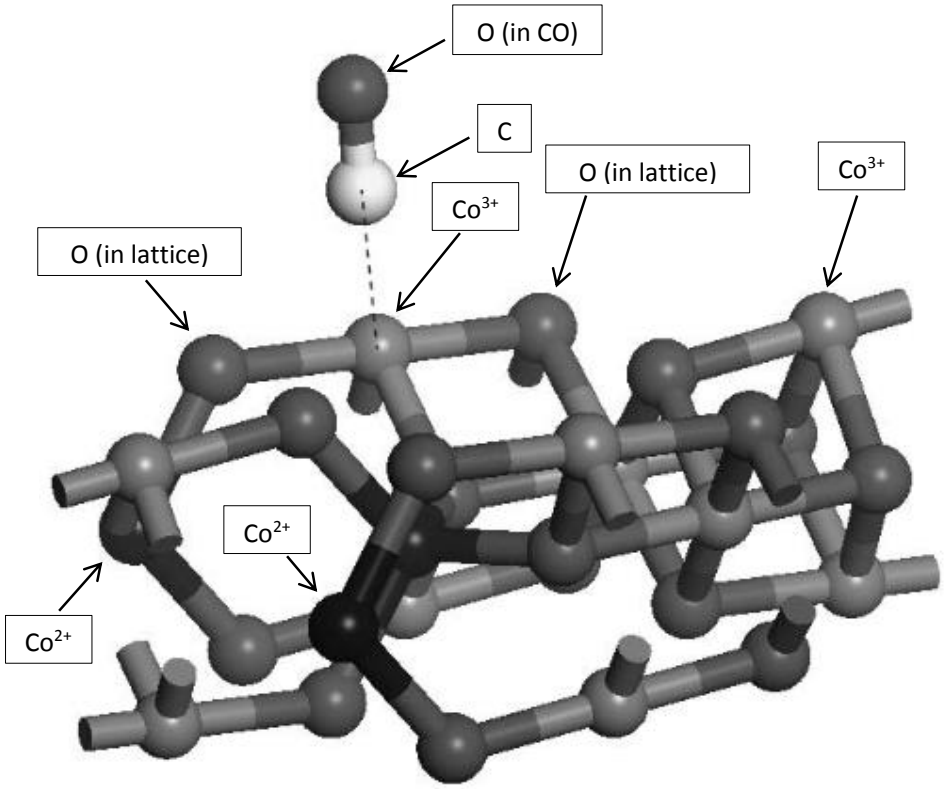

Figure 2.9: *A DFT-derived favourable adsorption mechanism for molecular CO on a Co_3O_4 surface. The CO is shown having a preference for the Co^{3+} ion species of Co_3O_4. [Adapted from Broqvist et al. (2002)].*

Unlike noble metal-based and CuO-based catalysts, Co_3O_4-based catalysts have not been studied as extensively in CO-PROX but of the few studies that do exist; these have looked at the use of different support materials including ZrO_2 (Zhao *et al.*, 2008; Zhao *et al.*, 2011), CeO_2 (Gawade *et al.*, 2012; Guo & Liu, 2007 and Yan *et al.*, 2014) and a mesh of wire (Marbán *et al.*, 2008) and how these support materials affect the performance of Co_3O_4. What has been observed with cobalt-based (ruthenium- and nickel-based catalysts too (Kim *et al.*, 2009; Malwadkar *et al.*, 2012)) is that at temperatures above 200 – 250 °C, they start to form CH_4 (Teng *et al.*, 1999, Woods *et al.*, 2010; Yung *et al.*, 2008). Teng *et al.* (1999), based on post-run PXRD analysis, reported that Co_3O_4 had fully reduced to metallic Co above 473 K which explained the formation of CH_4 as this has been previously observed over pure metallic Co catalysts (Herranz *et al.*, 2009; Tuxen *et al.*, 2013). The onset temperature for the reduction of Co_3O_4 may depend on certain physical characteristics of the catalyst like crystallite size (Liu *et al.*, 2013; Wang *et al.*, 2005) and/or the strength of the interaction between the nanoparticles and the support (Fischer *et al.*, 2012; Zhao *et al.*, 2008).

2.4. Catalyst deactivation mechanisms

Supported nanocrystalline catalysts can be expected to have a finite life-span during which numerous changes in their structural and chemical features; catalytic performance will take place over time. Catalysts deactivate via numerous pathways and there could be one or more pathways involved, with either all occurring simultaneously or each deactivation pathway being facile under certain conditions. There are two broad classes of catalyst deactivation *viz.,* inherent deactivation and operational deactivation (van Steen & Claeys, 2008). Inherent deactivation implies reduced catalytic activity over time due to changes in the catalyst's formulation under the normal reaction conditions. Some examples of inherent deactivation mechanisms include coking, sintering and transformations of the catalytically active phase. There may be strategies in place to deal with this kind of deactivation which could have been developed from past experiences with the same catalyst under the same reaction conditions. Operational deactivation is usually observed in industry where the applied conditions (for e.g., impure feed or mechanical deactivation) during a particular process are not close to ideal (van Steen & Claeys, 2008). Therefore, some examples of operational deactivation mechanisms include fouling, poisoning and attrition/crushing.

2.4.1. Deactivation by poisoning

Poisoning is a well-known deactivation mechanism whereby the feed for a particular reaction contains impurities which chemisorb on the catalyst's surface. Upon chemisorption, the catalytically active phase can become inaccessible to the desired reactants (Argyle & Bartholomew, 2015; Moulijn *et al.*, 2001). The chemisorption of poisons can also result in electronic and/or geometric changes of the surface. When using the gas product from the low-temperature WGS process as a feed for CO-PROX; CO_2, H_2O and H_2 can negatively affect the CO oxidation activity of the catalyst being used. At temperatures below 177 °C, CO_2 and H_2O have been shown to have an overall negative effect on the CO conversion to CO_2 (Guo & Liu, 2007; Monyanon *et al.*; 2007; Park *et al.*, 2004). This is indicated by a decrease in the CO conversion compared to that observed in the absence of CO_2 and H_2O. CO_2 and H_2O compete with the CO and O_2 for adsorption sites on the surface of the catalyst and as a result block the

access to these sites (Monyanon *et al.*; 2007; Park *et al.*, 2004). The adsorption of CO_2 has been also found to result in the formation of surface carbonates which also block access to the active sites (Marbán *et al*., 2009). CO_2 can react with H_2 to consequently increase the CO concentration in the product stream via the RWGS reaction (Brown Jr. *et al.*, 1960; Manaslip & Gulari, 2002; Woods *et al.*, 2010).

2.4.2. Deactivation by gas/vapour-solid reactions

When supported nanocrystalline catalysts are exposed to highly reducing (e.g. H_2 or CO) or oxidising (e.g. O_2 or H_2O) environments and elevated temperatures, phase changes in the catalyst can be expected (Argyle & Bartholomew, 2015; Fischer *et al.*, 2015; Sadasivan *et al*., 2013 and Teng *et al.*, 1999). The phase changes occur when gas species in the feed or products react with the catalyst or catalytically active species. A loss in activity and/or selectivity can be expected if the most active phase of the catalyst is lost as a result of a phase transformation *i.e.,* a reduction or an oxidation. The phase change might be dependent on the size of the crystallites as very small crystallites are more likely to undergo phase changes as compared to relatively larger crystallites (Fischer *et al.*, 2015; Liu *et al.*, 2013; Sadasivan *et al*., 2013). The phase change could also be dependent on the strength of interaction between the nanoparticles and the support (Fischer *et al.*, 2012; Scarlett & Madsen, 2006; Todorova *et al*., 1996).

Under CO-PROX conditions, there has been no mention of bulk phase changes (via oxidation) occurring when using noble metal-based catalysts. However, when using metal oxide catalysts, these can undergo reduction to intermediate oxide phases or down to their metallic phases due to the presence of H_2 in the feed (Gamarra *et al.*, 2007; Teng *et al.*, 1999). Teng *et al.* (1999) looked at different oxide catalysts and among these were Co-, Cu- and Ni-based based ones. Table 2.1 summarises some of the main results they obtained from performing post-run PXRD analyses which showed that these metal oxide-based catalysts reduced under CO-PROX conditions mainly to their metallic form. Over the Co- and Ni-based catalysts, the formation of methane was observed above 473 – 523 K which also confirmed that the corresponding oxides had reduced (Bartholomew *et al*., 1980; Herranz *et al.*, 2009; Tuxen *et al.*, 2013).

Table 2.1: *Showing the chemical phases present before and after CO-PROX; the onset of methane formation reported by Teng et al. (1999) for different metal oxide-based catalysts.*

Catalyst (before reaction)	Mass-specific surface area (m^2/g)	Temperature for CH_4 production (K)	Catalyst (after reaction)
CoO	13.5	> 523	Co, CoO
Co_3O_4	16.7	> 473	Co
CuO	9.2	-	Cu
NiO	53.1	> 473	Ni, NiO

2.4.3. Deactivation by sintering

Sintering is more facile for (very small) nano-sized crystallites due to their high surface energy. The driving force for the sintering process is therefore, the minimisation of this surface energy (Moulijn *et al*., 2001). Atoms on surfaces of crystallites (Ostwald ripening) or whole crystallites can migrate in numerous pathways to fuse with other crystallites to make larger ones as shown in Figure 2.10. This process is largely dependent on temperature, specifically on the melting point of the solid material, which in turn dictates the mobility of either the surface species or bulk species. Surface species/atoms migrate at relatively lower temperatures than bulk species which then makes this process largely driven by surface species (Buffat & Borel, 1976; Moulijn *et al*., 2001). The temperature at which surface species migrate is called the Hüttig Temperature ($T_{Hüttig} = 0.3 \times T_{melting}$) and the temperature at which the bulk species migrate is the Tamman Temperature ($T_{Tamman} = 0.5 \times T_{melting}$).

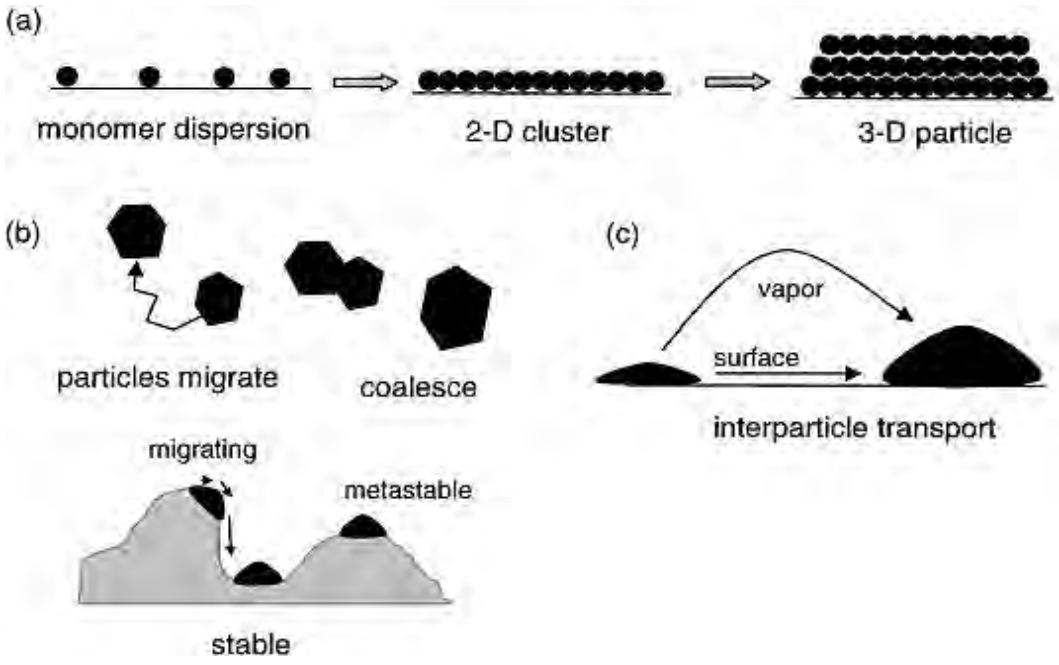

Figure 2.10: *Various pathways [(a), (b) and (c)] leading to crystallite size growth i.e sintering. [From Moulijn et al. (2001)].*

Since different kinds of materials (*i.e.,* metals and metal oxides), either used as catalysts or supports, have different melting points; this means that they will also have different Hüttig and Tamman Temperatures. Table 2.2 shows the melting points, $T_{Hüttig}$ and T_{Tamman} of different noble metals, base metals and metal oxides that have been explored in the CO-PROX reaction. It should be noted that the melting temperature, $T_{Hüttig}$ and T_{Tamman} of nanoparticles may be much less than the values given in Table 2.2 and so it is very important to immobilise these nanoparticles on thermally stable supports like Al_2O_3, SiO_2, CeO_2 and ZrO_2 (Moulijn *et al*., 2001).

To add on temperature, sintering can also be enhanced by the environment in which the reaction is being performed or by species introduced with the feed or by products formed in the reaction. For instance, water vapour and O_2 are known for inducing sintering of metal nanoparticles while H_2-rich environments are known to induce sintering of metal oxide nanoparticles and can also lead to a loss in the surface area of metal oxide supports (Argyle & Bartholomew, 2015; Marbán *et al*., 2009 and Zeng *et al.*, 2014). The use of low surface area support materials can also induce sintering as high enough dispersion of the catalytically active phase cannot be achieved (Moulijn *et al*., 2001).

Table 2.2: *$T_{melting}$, $T_{Hüttig}$ and T_{Tamman} values for some CO-PROX catalysts.*

Chemical Species	$T_{melting}$ (in K)	$T_{Hüttig}$ (in K)	T_{Tamman} (in K)
Pt[a]	2028	608	1014
Pd[a]	1828	548	914
Rh[a]	2258	677	1129
Ru[a]	2723	817	1362
Co[a]	1753	526	877
Ni[a]	1725	518	863
CoO[b]	2073[c]	622	1037
Co_3O_4[b]	1223[c]	369	612
NiO[a]	2228	668	1114
CuO[a]	1599	480	800

[a] obtained from Moulijn *et al*. (2001).

[b] obtained from Perry & Green (1997).

[c] decomposes at this temperature.

2.4.4. Other deactivation mechanisms

In the literature, there are other deactivation mechanisms that have been observed and some of these mechanisms are possible under certain reactions and with some only possible under certain reaction conditions. Fouling is a well-known deactivation mechanism where there may be materials either in the feed or products that physically adsorb on the surface of the catalyst and thus block access to the active sites and/or pores e.g. the formation of coke deposits. Mechanical deactivation (also called attrition) is also possible in instances where the catalyst, usually in fluidised or slurry bed reactors, is exposed to harsh conditions and breaks into fine particles which can end up leaving the reactor with the products (Argyle & Bartholomew, 2015; Moulijn *et al*., 2001). In the studies that have been done for the CO-PROX reactions, these

deactivation mechanisms have not been reported. It should also be noted that CO-PROX has not yet been widely commercialised and so it may be possible that some of these deactivation mechanisms will only be observed at industrial scale; not necessarily in laboratory-scale experiments.

2.5. Catalyst preparation

Choosing a method to employ for synthesising a catalyst is a task of great importance as the preparation method has an effect on the structural features of the synthesised catalyst. The structural features of the catalyst *i.e.,* its crystallite size, surface area, surface structure, dispersion of the nanoparticles on the support, the interaction between the nanoparticles and the support and the shape of the nanoparticles all have an effect on the catalytic performance (Rameswaran & Bartholomew 1989). There have been numerous synthetic methods that have been developed for synthesising heterogeneous catalysts and all of these have their own advantages and disadvantages. Therefore, it remains as the researcher's task to be able to decide on an appropriate method to employ depending on the parameters that need to be investigated for a certain reaction and catalyst.

2.5.1. Conventional synthetic methods for obtaining heterogeneous catalysts

2.5.1.1. Wetness and incipient wetness impregnation

Wetness and incipient wetness impregnation are the two widely used techniques for depositing catalytically active material on a support. Wetness impregnation involves firstly dissolving a catalyst precursor in water and contacting or impregnating the support material with this solution. After some time, the excess water is evaporated to obtain the impregnated solid catalyst. In incipient wetness impregnation, the precursor is dissolved in a volume of water

equal to (or slightly less than) the pore volume of the support being used (Adesina, 1996; Marceau *et al.*, 2008). The term "incipient wetness" therefore, refers to the point at which the pores of the support are just completely filled with the solution.

After impregnating the support, there is usually a drying and calcination process (Marceau *et al.*, 2008). Drying refers to the removal of the solvent (usually water) from the solid and calcination refers to a high-temperature immobilisation of the catalyst precursor in the form of crystallites. This calcination process is also conducted so to chemically and/or physically transform the catalyst precursor into a more durable form for storage or a form desired for its catalytic use. This process is normally conducted under air or O_2 and therefore, yields nanoparticles in their oxidic form (Marceau *et al.*, 2008). At the high temperatures used for this treatment, care must be taken so as to prevent sintering which would lead to crystallite sizes larger than those targeted.

2.5.1.2. Precipitation and co-precipitation

Precipitation generally means forming an insoluble solid from a homogeneous solution. This is mainly achieved with using a precipitating agent. This process is dependent on numerous factors like pH, precipitating agent, temperature, solvent and the composition of the solution just to mention a few (Schueth *et al*., 2008). Co-precipitation is when two different metal ions in a mixed solution are precipitated to form hydroxides or carbonates of two different metal ions (Fischer, 2011; Geus & van Dillen 2008). After the precipitation/co-precipitation, the normal drying and calcination processes are followed to obtain the target catalyst.

With these conventional methods, *i.e.,* impregnation and precipitation, the major disadvantage is that there is little control on the size of the crystallites in the final catalyst (Reuel & Bartholomew; 1984 and Fu & Bartholomew, 1985) and in the case of impregnation, it is difficult to obtain nanoparticles with a narrow size distribution (Anderson, 1984; Dry, 1981; Adesina 1996). Therefore, finding or developing a method which would enable the formation of crystallites with a consistent and tuneable size is also important. A method which has been considered and reported in the literature as being able to offer reasonably enough size control over the catalysts synthesised is the microemulsion technique which is discussed in detail in the following section.

2.5.2. The microemulsion technique

A microemulsion is a thermodynamically stable and optically clear system of three liquids *i.e.,* a non-polar, amphiphilic and polar phase (Danielsson & Lindman, 1981). The optical clarity of this system is largely controlled by the amphiphilic phase, which has properties enabling it to partly dissolve in both the non-polar and polar phases (Klier *et al.*, 2000). Temperature also plays a role in the stability of the microemulsion (Schwuger *et al*., 1995; Mabaso, 2005; Fischer, 2011) as it allows for the correct proportions of the amphiphilic phase to be dissolved in both the non-polar and polar phases, respectively. This ensures that an optically clear system is obtained when all three phases are mixed. It is therefore, crucial that the temperature at which a stable microemulsion system is formed remains unaltered at least until the nanoparticles have been liberated from the system by precipitation (Schwuger *et al*., 1995; Mabaso, 2005; Fischer, 2011).

There are two types of microemulsions *viz.,* micelles and reverse micelles. A micelle system is when the polar phase is much more abundant compared to the amphiphilic and non-polar phase. On the other hand, a reverse micelle is formed when the non-polar phase is present in large amounts relative to the amphiphilic and polar phase. In both systems, the phase present in low amounts relative to the amphiphilic phase forms small droplets in the microemulsion (Eriksson *et al.*, 2004) and these droplets are stabilised by the amphiphilic phase as shown in Figure 2.11.

Figure 2.11: *(**left**) Stable micelle and (**right**) reverse micelle system, respectively.*

When preparing microemulsions, different amphiphilic phases, mainly surfactants, can be used (Boutonnet *et al*., 2008 and Eriksson *et al.*, 2004). These surfactants are either ionic or non-ionic. Examples of ionic surfactants include sodium bis-(2-ethylhexyl)sulfosuccinate (AOT), cetyltrimethylammonium bromide (CTAB) and non-ionic surfactants include poly(oxyethylene)$_x$, nonylphenol ether (NP-X) and pentaethylene glycol dodecyl ether (PEGDE). The use of ionic and/or sulphur-containing surfactants is a disadvantage in that during the drying of metal nanoparticles, the residual surfactant on the nanoparticles can decompose and deposit on the particle to form catalyst poisons of sulfur-containg compounds and also deposition of metallic ions is possible which can be incorporated into the particles (Cheang, 2009; Fischer, 2011). Therefore, the use of non-ionic surfactants is preferred over ionic ones for catalyst preparation using the reverse micelle method.

2.5.2.1. Preparation of nanocrystallites using the reverse micelle technique

Nanoparticles have been prepared using the reverse micelle technique and used in many important chemical reactions. The nanoparticles formed using this method generally have a narrower size distributions compared to nanoparticles prepared using conventional synthetic methods (Boutonnet *et al*., 2008). As mentioned earlier, a reverse micelle is formed when the non-polar/oil phase is more abundant than the both the surfactant and water phase, with the surfactant more abundant than the water phase. This means that in a reverse micelle, water is present in the form of small droplets (Eriksson *et al.*, 2004) and these droplets are seen as nanoreactors because this is where the precipitation of the metal precursor will occur.

There are two ways of synthesising nanoparticles using the reverse micelle as shown in Figure 2.12 (Eriksson *et al.*, 2004). The first one involves preparing two similar stable reverse micelle systems but one will have the water phase containing the metal precursor and the reverse micelle would have the precipitating agent dissolved in the water phase. After preparing the reverse micelles, they would then be mixed together and during the mixing, the reverse micelles with the metal precursor would collide with those containing the precipitating agent which will result in the formation of an insoluble nanoparticle.

The other way of preparing nanoparticles is to just prepare a single stable reverse micelle system with the water phase containing the metal precursor. The precipitating agent is then introduced

as an aqueous solution into the reverse micelle system and it makes its way to the water droplets containing the metal precursor in order to precipitate the metal precursor and form a nanoparticle (Eriksson *et al.*, 2004).

The formed nanoparticles from using either of the two routes discussed are still confined in the droplets of the reverse micelle and so the next step is a flocculation step whereby substances like acetone or tetrahydrofuran (THF) are added to the reverse micelle system so to destabilise it and liberate the nanoparticle (Eriksson *et al.*, 2004). The flocculating agent would need to be added a couple more times as a washing procedure to remove the surfactant around the nanoparticles. After extensively washing the nanoparticles, they could be then adhered to a support material and that itself can be done in various ways (Cheang, 2009; Fischer *et al.*, 2012).

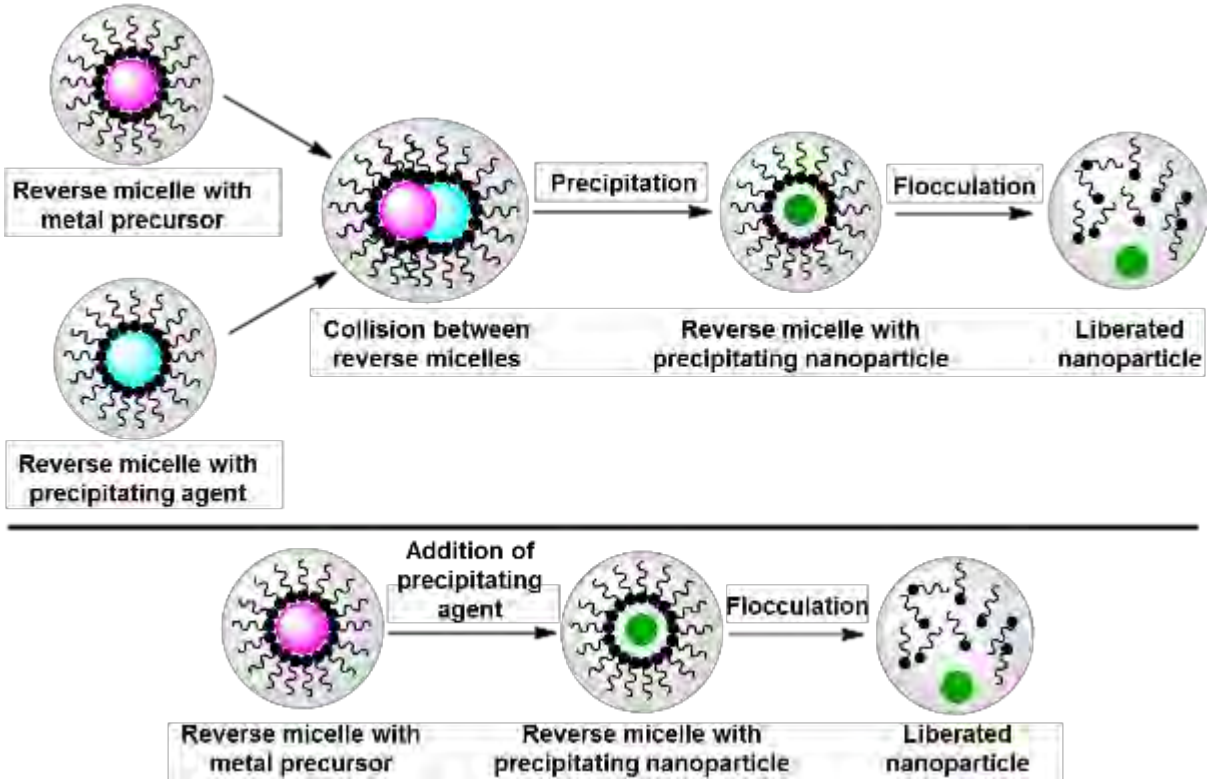

Figure 2.12: *Formation of nanoparticles from (**top**) colliding two reverse micelle solutions and also from (**bottom**) a single reverse micelle solution.*

2.5.2.2. Factors that influence crystallite size when using the reverse micelle technique

When synthesising nanoparticles using the reverse micelle technique there are three essential parameters that affect the final crystallite size of the catalysts (Boutonnet *et al*., 2008 and Eriksson *et al.*, 2004) and these are:

i) The non-polar phase-to-amphiphilic phase ratio;
ii) The polar phase-to-amphiphilic phase ratio (ω) and;
iii) The concentration and/or strength of the precipitating agent to be used.

Both the first and second factors are crucial to consider since the amphiphilic phase (usually a surfactant) dissolves in both the non-polar and polar phases in different proportions. Also since the polar phase is present in small volumes relative to the non-polar phase in a typical reverse micelle system, the polar phase will form droplets in the system and these should be stabilised by the surfactant. So a careful minimisation of the two ratios mentioned above in i) and ii), respectively, will ensure that a significant amount of the surfactant is available for stabilising the droplets. The size of the droplets is largely influenced by ω and so a minimisation of ω will increase the number droplets formed and consequently decrease the size of the droplets (Lisiecki & Pileni, 1993). Inside these droplets formed by the polar phase, there are ionic species of the catalyst precursor which had been dissolved prior to mixing the polar phase with the other two phases to form the microemulsion. The microemulsion system is dynamic, and so micelles are constantly colliding and coalescing, allowing for the aggregation of ions/atoms to occur and form the final particle. The rate of particle growth is hindered by the presence of the surfactant around the droplet which prevents the nuclei from growing too quickly. The particles will then grow at the same rate, producing particles with a narrow size distribution (Eriksson *et al.*, 2004).

As already mentioned above, the solid nanoparticles that form in these droplets are obtained as result of adding a precipitating agent (usually basic in nature). The concentration and/or strength of the precipitating agent plays an important role in the onset of the precipitation of the metal hydroxide. Generally, fast nucleation will result in smaller particles and so high concentrations and/or strength of the precipitating agent will encourage a fast nucleation process and prevent further collisions of ions/atoms with already formed nuclei in the droplet (Boutonnet *et al.*, 1982). A faster nucleation will therefore, result in the formation of small particles with a narrow

size distribution. The use of precipitating agents with no metals or metal ions is preferred over the ones with metallic species due to the possible deposition of unwanted metallic species on the catalyst particles during the precipitation step (Fischer, 2011).

2.6. Effect of crystallite size and metal-support interactions on the catalytic CO oxidation and CO-PROX activity

As pointed out in section 2.5, the task of choosing a technique for synthesising nanoparticles is a very important one as it can influence the performance of the nanoparticles used as the catalyst (Rameswaran & Bartholomew 1989). Different techniques or methods can produce nanoparticles having different crystallite sizes and/or different particle shapes. Other techniques can allow for the alteration of the strength of the interaction between the metal and the support (Cheang, 2009; Fischer *et al.*, 2012). Depending on the reaction to be carried out, the conditions and desired products, the aforementioned characteristics of supported nanoparticles used as catalysts are important to consider. The crystallite size is one important subject that has been discussed for decades and has led to the classification of heterogeneously catalysed reactions as either being structure/size dependent or independent (Cuenya & Behafarid, 2015; van Santen, 2009). The effect of metal-support interactions is also an important subject and can be closely linked to crystallite size (Cuenya & Behafarid, 2015). Support materials are generally regarded as inert and should only help in preventing or slowing down the sintering of the nanoparticles and offer them mechanical strength (Delmon, 2008). However in some other reactions, especially oxidation reactions, the support can directly influence the performance of nanoparticles used as catalysts through the presence of significant metal-support interactions (Cuenya & Behafarid, 2015).

2.6.1. Crystallite size effects

When speaking about the "effect of crystallite size", this normally refers to how the performance of each atom/active site present on the surface is affected by the crystallite size size (or its change thereof). It is therefore, common practice to normalise the observed activity for each catalyst sample by its surface area to obtain a descriptor commonly known as the turnover frequency (TOF) or surface area-specific activity (Cuenya & Behafarid, 2015). CO oxidation in the absence of H_2 is generally regarded as a structure/size dependent reaction. However, depending on the metal or metal oxide used as the active phase, the activity trends with changing crystallite sizes can be different.

For example, Valden *et al.* (1998) looked at TiO_2-supported Au nanoparticles with varying crystallite sizes from 2 to 6.5 nm for the oxidation of CO in the absence of hydrogen. They observed a volcano-type size dependency of the TOF, with Au nanoparticles with an average size of 3.5 nm showing the highest TOF at 350 K. Boubnov *et al.* (2012) investigated γ-Al_2O_3 supported Pt nanoparticles with varying crystallite sizes from 1 to 10 nm for the same reaction and also observed a volcano-type size dependency of the TOF. Pt nanoparticles within the 2 – 3 nm size range showed the highest TOF and those with an average size of 5 nm showed the lowest TOF between reaction temperatures of 40 and 90 °C. Joo *et al.* (2010) reported that the TOF of their Ru nanoparticles increased as their crystallite sizes were increased from 2 to 6 nm within the 180 - 240 °C temperature range during CO oxidation. Jia *et al.* (2010) also observed a steady increase of the TOF with increasing crystallite size of CeO_2-supported CuO nanoparticles from 2 to 31 nm during the same reaction. Liu *et al.* (2013) and Wang *et al.* (2005) investigated different sizes of Co_3O_4 nanoparticles and reported that decreasing the crystallite size of Co_3O_4 increased their mass-specific CO oxidation activity in the absence of hydrogen. Changes in the TOF with Co_3O_4 crystallite size were not reported.

Iablokov (2011) looked at the CO oxidation activity of Co_3O_4 in the absence of hydrogen with crystallite sizes varying between 3.5 and 12.5 nm. Iablokov showed that there exists a volcano-type size dependency of the surface- and mass-specific rate at 423 K. Crystallites with sizes ranging from 5 to 8 nm displayed the highest surface area-specific rate as shown in Figure 2.13.

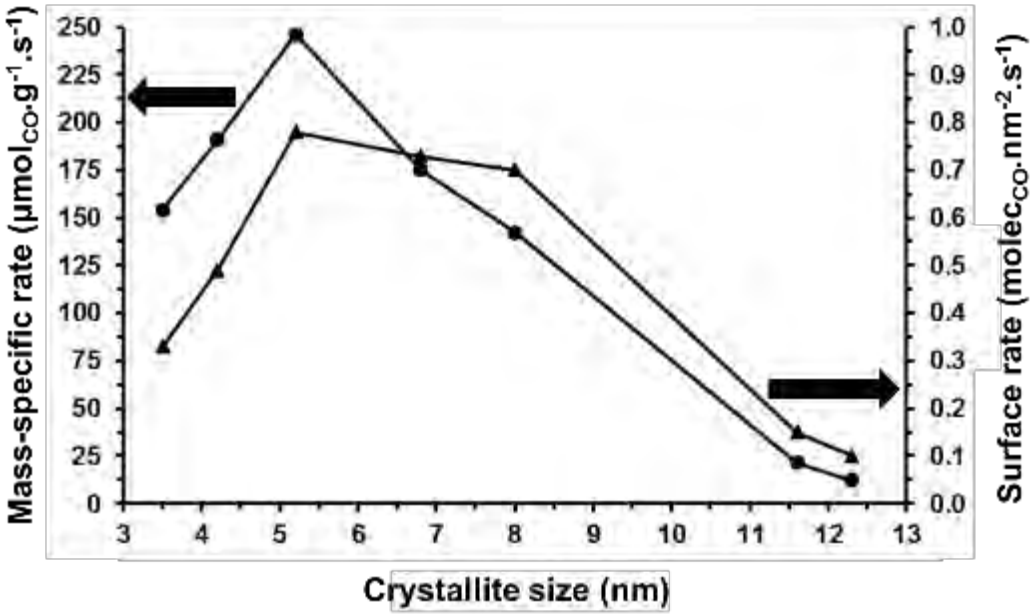

Figure 2.13: *Mass- and surface area-specific rates as a function of the starting crystallite size of Co_3O_4 at 423 K under CO oxidation conditions. [Replotted the data from Iablokov (2011)].*

Iablokov further confirmed that the CO oxidation reaction over Co_3O_4 catalyst proceeds via the Mars-van Krevelen mechanism by performing a Steady-State Isotopic Transient Kinetic Analysis (SSITKA). For this kind of analysis or experiment, the catalyst was firstly exposed to a gas mixture of $^{16}O_2$/CO/Ar until steady-state was reached. Thereafter, this gas mixture was abruptly replaced with a mixture of $^{18}O_2$/CO/Ar. The partial pressure of each gas in the two mixtures remained exactly the same and therefore, the overall reaction remained at steady state after the switch. However, there was a transient concentration change in the fraction of ^{16}O- and ^{18}O-labelled species exiting the reactor. This then allowed for the measurement of the oxygen-exchange rates on the surface of each Co_3O_4 catalyst. Figure 2.14 shows the oxygen-exchange rates over Co_3O_4 catalysts of different crystallite sizes. What was observed is that the exchange rates displayed a volcano-type size dependency similar to that displayed by the TOF and the mass-specific rate. Iablokov attributed the decrease in the specific reaction rates and O_2-exchange rates below 5 – 8 nm to the changes in the electronic structure of Co_3O_4 *i.e.,* the Co-O bond becomes too strong in the case very small crystallites. This in turn decreases the CO conversion to CO_2.

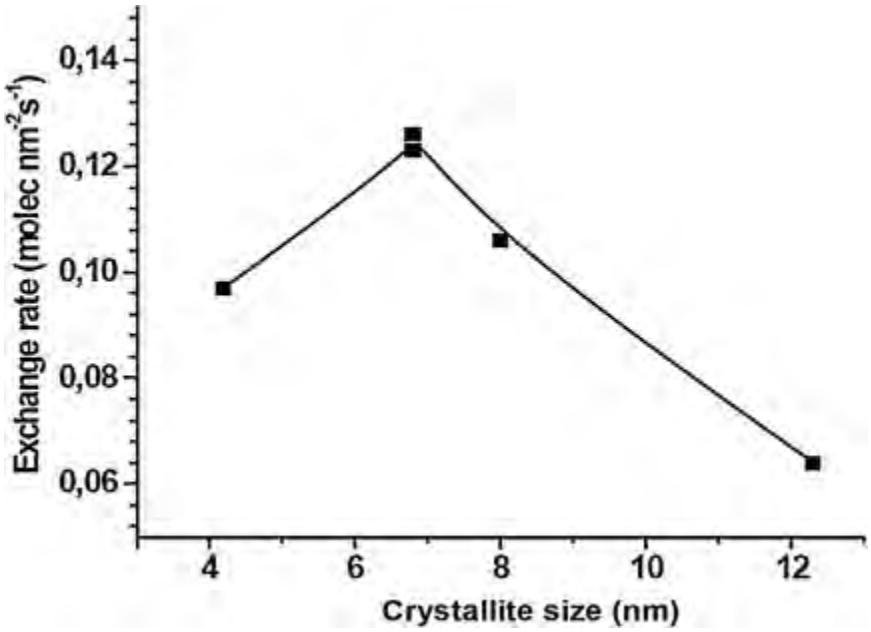

Figure 2.14: *Oxygen-exchange rates on the surface of Co_3O_4 as a function of crystallite size measured during SSITKA experiments at 623 K under CO oxidation conditions. [From Iablokov (2011)].*

In CO-PROX, very few studies have looked at the effect of crystallite size on the catalyst's performance and among these is a study by Zeng *et al.* (2013) were they looked at an inverse catalyst system with CeO_2 nanoparticles supported on CuO. After varying the crystallite size of CeO_2 between 4 and 11 nm, they observed that at 90 °C the TOF increased with an increase in the crystallite size of CeO_2. However, the total CO conversion at this temperature was generally higher when small crystallites were used as shown in Figure 2.15. Finally, a study done by Kim *et al.* (2012) showed that between two Al_2O_3-supported Ru catalysts of 4.9 and 6.5 nm average size, the 6.5 nm Ru catalyst showed a higher TOF under CO-PROX conditions between 333 and 375 K.

The subject of crystallite size effects on CO oxidation and CO-PROX is still a very complex one. As discussed above in this sub-section, the dependency of the TOF on crystallite size can vary with the type of metal or metal oxide being used. Reliable conclusions on the size-dependency of the TOF could also be limited by the crystallite size range used for the study (Cuenya & Behafarid, 2015).

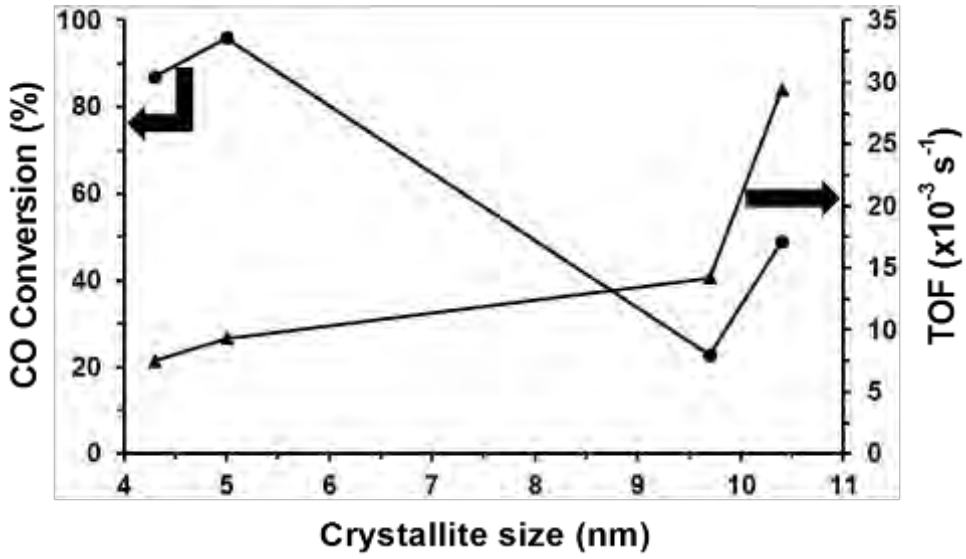

Figure 2.15: *CO conversion and TOF both as a function of crystallite size under CO-PROX conditions at 90 °C. [Replotted the data from Zeng et al. (2013)].*

2.6.2. Effects of metal-support interactions

Support materials are commonly used in heterogeneous catalysis, for example, to offer mechanical strength for nanoparticles against attrition, and also to immobilise and disperse the nanoparticles on it to prevent or slow down sintering. Common support materials are usually oxidic supports like Al_2O_3, TiO_2, ZrO_2 and CeO_2 etc. (Cuenya & Behafarid, 2015). There are numerous methods of adding nanoparticles onto support materials and depending on the method used, strong or weak interactions could be inflicted between the nanoparticles and the support (Cheang, 2009; Fischer *et al.*, 2012). The strength of this interaction can have positive or negative effects on the performance of the nanoparticles. CO oxidation or CO-PROX involves a reaction between CO and O_2 to form CO_2. The mechanism of this reaction depends on the whether a metal or metal oxide-based catalyst is used and also depends on whether a reducible or irreducible oxidic support is used (Wootsch *et al*., 2004; Zhao *et al*., 2008).

CeO_2, ZrO_2 and MgO, for example, are generally regarded as reducible and Al_2O_3 and TiO_2 are regarded as irreducible (Cuenya & Behafarid, 2015, Wang *et al.*, 2006; Zhao *et al*., 2008). Therefore, strong metal-support interactions (SMSI) in CeO_2-, ZrO_2- or MgO-supported catalysts can mean enhanced CO oxidation activity since these supports can offer oxygen species that can oxidise CO via the Mars-van Krevelen mechanism (Molina & Hammer, 2003;

Zhao *et al*., 2008). SMSI in Al_2O_3- and TiO_2-supported catalysts for instance may not be beneficial as these supports are reducible and cannot offer the required oxygen species for oxidising CO (Wang *et al.*, 2006; Zhao *et al*., 2008).

Zhao and co-workers (2008) evaluated the reducibility of Co_3O_4 catalysts supported on CeO_2, ZrO_2, SiO_2, TiO_2 and γ-Al_2O_3, respectively. They found that the onset of reduction of Co_3O_4 when supported CeO_2, ZrO_2, SiO_2 was at lower temperatures (*i.e.,* 320 – 330 °C) as shown in Table 2.3. The reduction of Co_3O_4 when supported on TiO_2 and γ-Al_2O_3 was at higher temperatures (*i.e.,* 390 °C and 470 °C, respectively). The delayed reduction of the TiO_2- and Al_2O_3-supported catalysts was attributed to the existence of SMSI. They also tested these five catalysts for CO-PROX activity and found that over the TiO_2- and Al_2O_3-supported catalysts, less CO was converted to CO_2 as a function of temperature as shown in Figure 2.16. However, they found that the CeO_2-, ZrO_2- and SiO_2-supported catalysts began to form methane at relatively low temperatures as a result of the reduction of Co_3O_4 to metallic Co. From these experiments they concluded that the SMSI in catalysts supported on irreducible supports can negatively affect the catalyst's performance. However, these supports can help improve the stability of the metal oxide-based catalyst by preventing its reduction to less active bulk phases under CO-PROX conditions.

Table 2.3: *Temperature at which the first reduction peak of Co_3O_4 was observed during H_2-TPR. [Adapted from Zhao et al. (2008)].*

Co_3O_4/CeO_2	Co_3O_4/ZrO_2	Co_3O_4/SiO_2	Co_3O_4/TiO_2	$Co_3O_4/\gamma\text{-}Al_2O_3$
320 °C	330 °C	330 °C	390 °C	470 °C

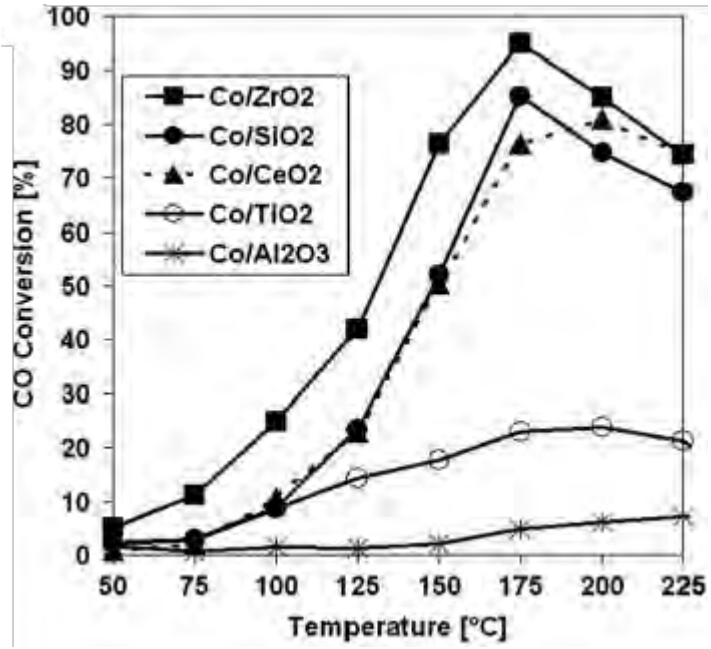

Figure 2.16: *CO conversion as a function of temperature over different supported Co_3O_4-based catalysts. [Adapted from Zhao et al. (2008)].*

Chapter 3: Scope of Thesis

The production of hydrogen for fuel cell applications has been gaining ever-increasing interest. The hydrogen is typically produced via reforming of liquid fuels or natural gas followed by a two-step water gas shift process. The produced hydrogen-rich gas still contains CO in trace amounts (approx. 0.5 - 1%) and this CO needs to be further converted as it presents a poison to the platinum catalyst on the anode side of the fuel cell (Mishra & Prasad, 2011; Park *et al*., 2009). The catalytic preferential oxidation of CO (CO-PROX) has been described as the most promising route for this conversion. In this reaction it is aimed to choose and design the heterogeneous catalyst such that minimal loss of hydrogen occurs via its oxidation with oxygen which gets co-fed. Catalysts used in this reaction are often platinum group-based (Pt, Pd, Ir, Ru, Rh) as well as gold-based. However, also much cheaper base metal oxides have shown significant potential as catalysts for this reaction like copper oxide, cerium oxide and cobalt oxide (Co_3O_4) (Mishra & Prasad, 2011; Park *et al*., 2009).

In this study, γ-Al_2O_3-supported Co_3O_4 nanoparticles were investigated as catalysts for CO-PROX. The specific objectives of the project were to:

- Investigate the effect of Co_3O_4 crystallite size and reaction temperature on the CO oxidation activity and phase integrity of Co_3O_4.
- Look into the effect of metal-support interactions and reaction temperature on the CO oxidation activity and phase integrity of Co_3O_4.

The reverse micelle technique was used to synthesise these Al_2O_3-supported Co_3O_4 catalysts of varying crystallite sizes (Fischer *et al*., 2011). This method was chosen as it has been shown that it gives rise to nanoparticles with a narrow size distribution. The synthesised catalysts were characterised using powder X-ray diffraction (PXRD), transmission electron microscopy

(TEM), energy-dispersive X-ray (EDX) spectroscopy and hydrogen temperature-programmed reduction (H_2-TPR). All these *ex situ* characterisation techniques gave valuable information on the crystallite size of the formed phase (*i.e.,* Co_3O_4), the size distributions, Co_3O_4 loading and its reducibility as a function of crystallite size and temperature. Catalytic tests were performed in a fixed bed reactor using a feed containing only CO, O_2, H_2 and N_2. CO_2 and H_2O were not added as the study focused only on the effect of H_2 on the CO oxidation activity of Co_3O_4 and its reducibility under reaction conditions. The addition of H_2O and CO_2 has been shown to have a negative effect on the performance of CO-PROX catalysts, and may also affect the reduction behaviour of Co_3O_4 as a result, interfering with obtaining the kind of information needed.

In situ characterisation involved the use of novel UCT-developed instruments *viz.,* a magnetometer and a PXRD cell (Claeys *et al.*, 2010; Claeys & Fischer, 2013; Fischer *et al.*, 2014). The magnetometer gave very useful kinetic data as well as information on the degree of reduction of Co_3O_4 to metallic cobalt since this instrument is more sensitive to magnetic material. The PXRD cell was used as a complementary technique for monitoring the bulk phase changes from Co_3O_4 to CoO and Co as a function of reaction temperature and crystallite size of Co_3O_4.

Chapter 4: Experimental Methodology

4.1. Preparation of supported Co_3O_4 catalysts

4.1.1. Variation of the crystallite size of Co_3O_4

As mentioned in Chapter 3, this study will involve an investigation into the crystallite size effects of Co_3O_4-based catalysts on the preferential oxidation of CO. To achieve this, Co_3O_4 nanoparticles with a narrow size distribution needed to be synthesised and the reverse micelle technique was chosen for this purpose (Fischer *et al*., 2011).

To prepare stable reverse micelle solutions, three different liquid phases were mixed *viz.,* n-hexane (AR grade, Kimix) as the oil or non-polar phase, pentaethylene glycol dodecylether or Berol 050 (Akzo Nobel) as the amphiphilic phase or surfactant and water as the polar phase. The amounts of each liquid phase added in each of the five prepared microemulsions are shown in Table 4.1. Firstly, the n-hexane was mixed with Berol 050 under stirring using an over-head stirrer (with a stainless steel impeller) for sixty minutes at 800 rpm in a 1000 or 2000 ml Schott bottle at room temperature and atmospheric pressure. Then an aqueous solution of $Co(NO_3)_2.6H_2O$ (Sigma Aldrich, reagent grade 98% purity) was prepared and thereafter added to the stirring n-hexane-Berol 050 mixture after sixty minutes. This new ternary mixture was stirred for a further two hours before being allowed to stabilise overnight.

After this, an optically clear and stable pink reverse micelle solution was obtained which indicated that the right proportions of the non-polar, amphiphilic and polar phases had been mixed at room temperature. To the stable solution, a 25 wt.-% NH_3 aqueous solution (Kimix) was then added dropwise under stirring and left to stir for a further thirty minutes allowing for

the precipitation of cobalt nitrate to form $Co(OH)_2$ nanoparticles. A Co^{2+}:NH_3 molar ratio of 1:4 was used to ensure the complete precipitation of cobalt nitrate to $Co(OH)_2$ nanoparticles. The formed $Co(OH)_2$ nanoparticles were still enclosed in the reverse micelle system and needed to be liberated through flocculation *i.e.,* the destabilisation of the microemulsion (Eriksson *et al.*, 2004). This was done by adding acetone (AR grade, Kimix) dropwise under stirring and each time, the amount of acetone added was always double the total volume of the prepared reverse micelle solution. After complete flocculation, the nanoparticles were allowed to settle to the bottom of the Schott bottle and the resulting supernatant was syphoned using a long piece of silicon tubing. The nanoparticles were washed a couple of times with copious amounts of acetone until a colourless supernatant was obtained. This extensive washing procedure also ensured that little or no surfactant phase remained around the nanoparticles. After the washing procedure, the nanoparticles were transferred into a dry 250 ml beaker and were allowed to settle to the bottom of the beaker before syphoning the excess acetone. The remaining acetone after syphoning was allowed to evaporate at room temperature and atmospheric pressure and thereafter, the particles were ground to obtain a fine powder of $Co(OH)_2$. This powder was further dried in a Memmert oven overnight at 120 °C and subsequently calcined in a Nabertherm furnace in air at 200 °C for sixty minutes and obtained a black powder. This unsupported black powder was characterised by PXRD and TEM to confirm its chemical composition and also to determine the average sizes of crystallites.

Table 4.1: *Composition of the reverse micelle solutions prepared at room temperature and atmospheric pressure for producing different crystallite sizes of Co_3O_4.*

Sample Name	Hexane (g)	Berol 050 (g)	Water (g)	o/s[a] (mol/mol)	w/s[b] (ω, mol/mol)	$Co(NO_3)_2.6H_2O$ (g)
TN_01	250.0	22.0	15.0	53.6	15.4	4.4
TN_02	250.0	25.0	15.0	47.2	13.7	3.3
TN_03	500.0	68.3	26.4	34.5	8.7	2.6
TN_04	500.0	68.4	18.2	34.5	6.0	1.6
TN_05	875.0	161.0	12.0	25.6	1.7	1.3

[a] oil-to-surfactant ratio

[b] water-to-surfactant ratio

The black powder was re-suspended in distilled water under ultrasonication for sixty minutes to break-up the nanoparticles before depositing them on to the support material. The support chosen for depositing the Co_3O_4 nanoparticles was γ-Al_2O_3 (Puralox (Batch 9574), SCCa 5-150, Sasol Germany: S_{BET} = 162 m^2/g, V_{pore} = 0.47 cm^3/g, $đ_{pore}$ = 11.5 nm, $đ_{particle}$ = 150-200 μm). An amount of γ-Al_2O_3 which would allow for obtaining a 10 wt.-% loading of Co_3O_4 was placed in a dry round bottom flask and to it, the Co_3O_4-water suspension was added. The round bottom flask was transferred to a rotary evaporator to remove the water. This was done under a vacuum pressure of 250 mbar and a temperature of 70 °C. The procedure detailed above is illustrated in Figure 4.1. The obtained powder of Co_3O_4/Al_2O_3 appeared dark grey and was further characterised with PXRD, TEM, EDX and H_2-TPR.

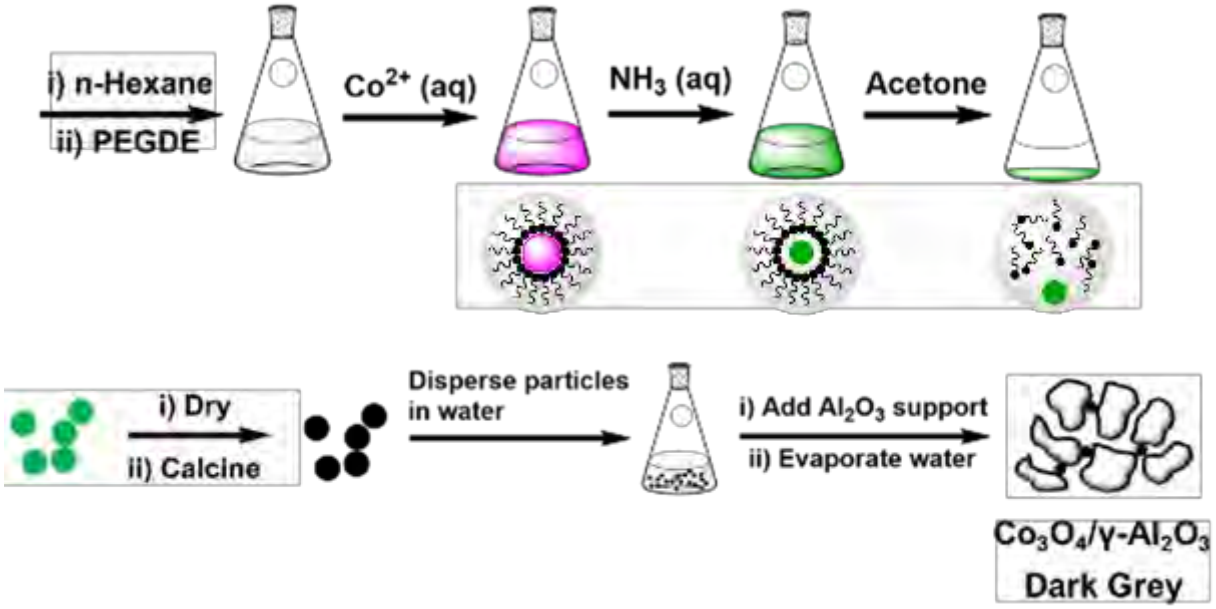

Figure 4.1: *Illustration of the steps followed in an attempt to obtain γ-Al_2O_3 supported Co_3O_4 crystallites of varying sizes.*

4.1.2. Alteration of the support-addition method

Altering the method by which the nanoparticles are deposited on the support or by which the metal precursor is contacted with the support material, can vary the strength of the interaction between the support and the nanoparticles (Fischer *et al.*, 2012). In this study, this was done to see the effect of the strength of the interaction on the catalytic performance and reducibility of Co_3O_4/Al_2O_3 catalysts. The crystallite size of Co_3O_4 was set to remain in the 3.0 – 5.0 nm range so to minimise the size effect in this part of the investigation.

Four catalysts were synthesised and named RM_1, RM_2, RM_3 and RM_4. The composition of each microemulsion prepared is summarised in Table 4.2. RM_1 was synthesised using the same method detailed in section 4.1.1 and was identical to TN_05. RM_2 was synthesised by preparing a reverse micelle solution with the cobalt precursor already dissolved as detailed in section 4.1.1. However, before adding the 25 wt.-% NH_3 aqueous solution for precipitation, an amount of γ-Al_2O_3 for obtaining a 10 wt.-% Co_3O_4 loading was added to the reverse micelle solution and then the solution was stirred for a further sixty minutes. The steps detailed in section 4.1.1 following from the addition of the precipitating agent were followed as is and are

illustrated in Figure 4.2 except, the calcination was performed at 400 °C for three hours instead of 200 °C for one hour.

Table 4.2: *Composition of the reverse micelle solutions used for preparing γ-Al_2O_3 supported Co_3O_4 crystallites with varying metal-support interactions.*

Sample Name	Hexane (g)	Berol 050 (g)	Water (g)	o/s[a] (mol/mol)	w/s[b] (ω, mol/mol)	$Co(NO_3)_2.6H_2O$ (g)
RM_1 (TN_05)	875.0	161.0	12.0	25.6	1.7	1.3
RM_2	500.0	68.3	26.4	34.5	8.7	2.6
RM_3	500.0	68.3	26.4	34.5	8.7	2.6
RM_4	500.0	68.4	18.2	34.5	6.0	1.6

[a] oil-to-surfactant ratio

[b] water-to-surfactant ratio

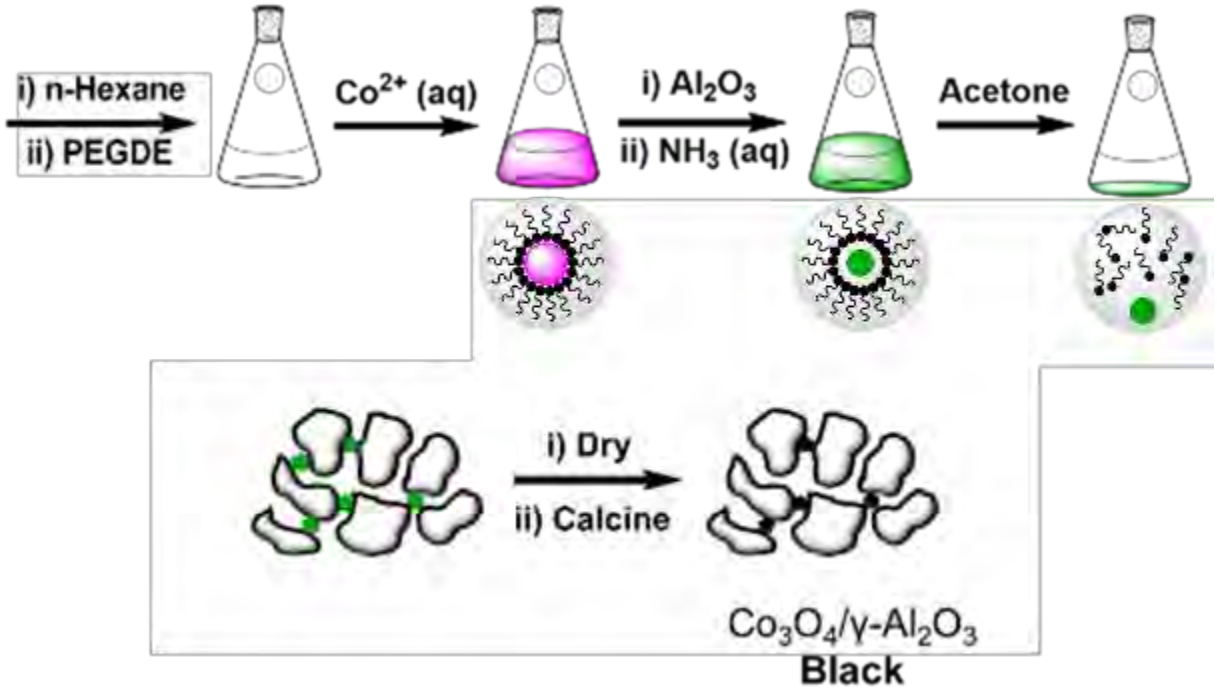

Figure 4.2: *Illustration of the steps followed in an attempt to obtain the γ-Al_2O_3 supported Co_3O_4 catalyst RM_2.*

For preparing RM_3, the γ-Al_2O_3 support was added thirty minutes after the addition of the precipitating agent to the reverse micelle solution containing the cobalt precursor and this resulting mixture containing the γ-Al_2O_3 support was stirred for a further sixty minutes. The other steps following after the addition of the support material were identical to those used for synthesising RM_2 and are illustrated in Figure 4.3. RM_4 was synthesised almost in a similar manner to RM_1. The difference was that the dried $Co(OH)_2$ were instead re-dispersed in acetone under ultrasonication for sixty minutes, thereafter this suspension was added to the γ-Al_2O_3 support in a round-bottom flask as in RM_1. The acetone was removed using a rotary evaporator to obtain a light green powder. The obtained powder was then dried at 120 °C overnight and calcined at 200 °C in an oven in air for sixty minutes. The general procedure for producing RM_4 is illustrated in Figure 4.4. All four samples were characterised using PXRD, TEM, EDX & H_2-TPR.

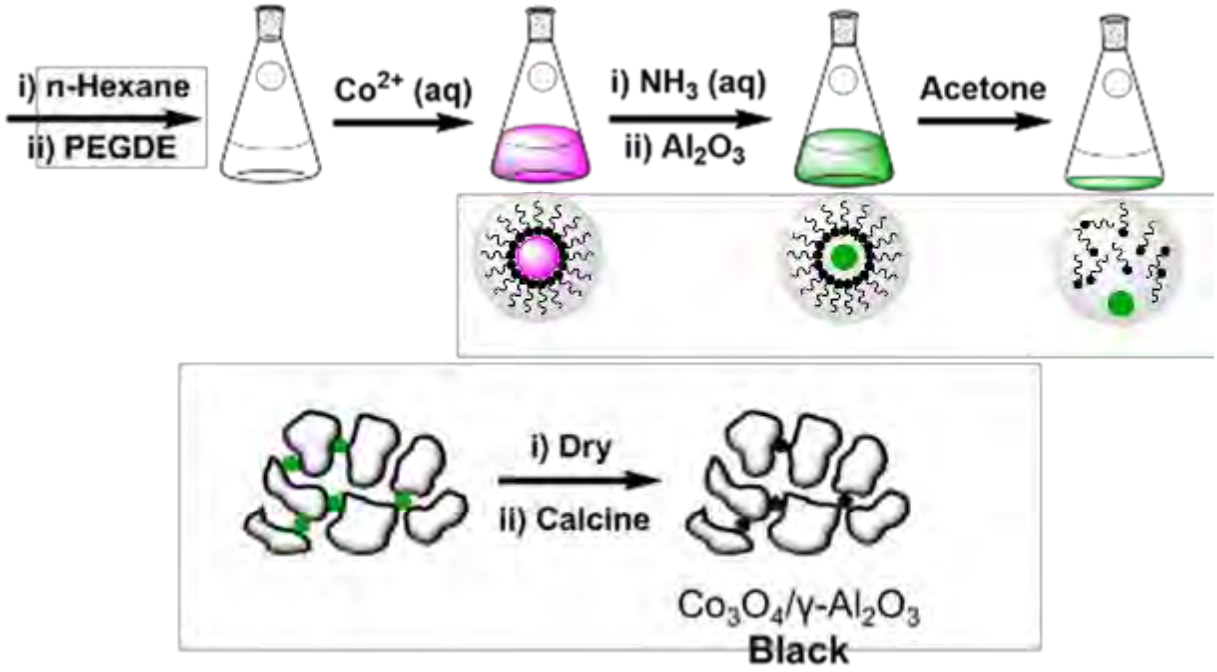

Figure 4.3: *Illustration of the steps followed in an attempt to obtain the γ-Al_2O_3 supported Co_3O_4 catalyst RM_3.*

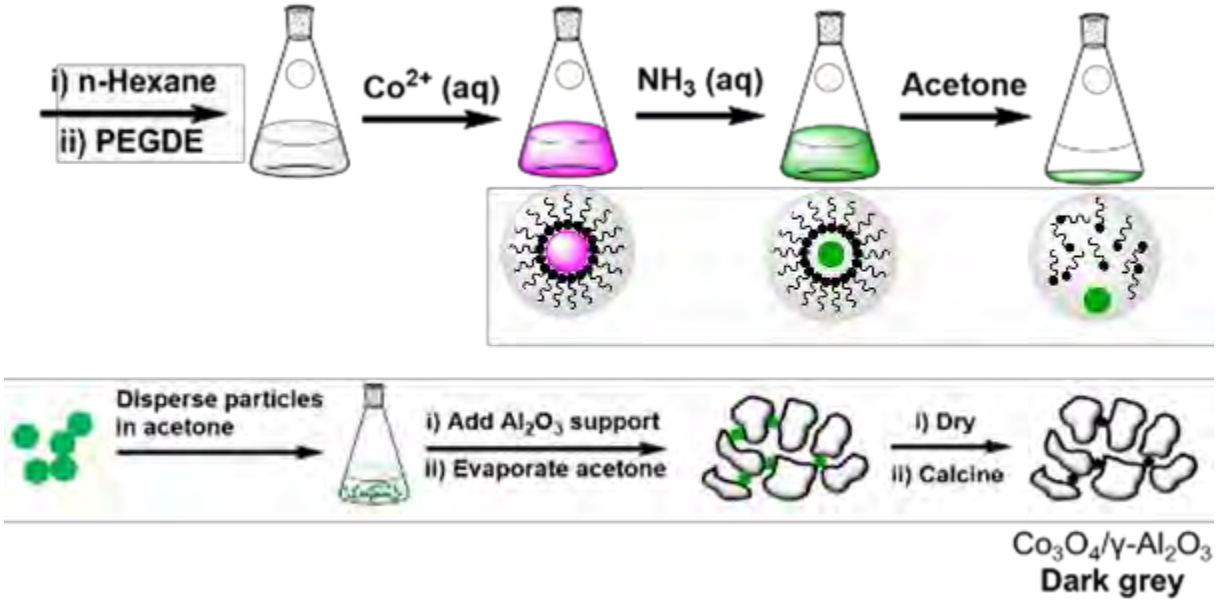

Figure 4.4: *Illustration of the steps followed in an attempt to obtain the γ-Al_2O_3 supported Co_3O_4 catalyst RM_4.*

4.2. *Ex situ* characterisation of the synthesised Co_3O_4/γ-Al_2O_3 catalysts

4.2.1. Powder X-ray diffraction (PXRD)

Powder X-ray diffraction measurements were conducted using a Bruker D8 Advance Laboratory X-ray diffractometer equipped with a cobalt source (λ = 1.78897 Å) and a position sensitive detector (Bruker Vantec). The scan range was 20 ° < 2θ < 130 ° (step size: 0.01233218 ° and time per scan: 0.3 seconds) and the total scan time was 47.75 minutes. The different phases present in the fresh and spent supported catalysts were identified by comparing with the peak positions and relative intensities recorded in the International Centre for Diffraction Data PDF-2 database.

Rietveld refinement, using the software program TOPAS 4.1, was applied to further identify the crystalline phases present and also to determine their average crystallite size. Since the alumina support used in this study is not pure γ-Al_2O_3 but contains small amounts of δ-Al_2O_3

(which has an unknown crystal structure), a method called PONKCS *i.e.,* partial or no known crystal structures (Scarlett & Madsen, 2006) was used to obtain weight percentages of each phase present. Where possible, the data obtained here was compared to the data obtained using EDX.

4.2.2. Transmission electron microscopy (TEM)

Analysis of the fresh and spent supported catalysts was conducted on different microscopes. For obtaining crystallite size distributions and morphology of the cobalt-bearing crystallites, a Tecnai F20 Transmission Electron Microscope operated at 200 kV was used. Each sample containing unsupported crystallites was dissolved in methanol in a small Eppendorf tube and sonicated for 10 minutes and thereafter a small amount of the suspension was transferred onto carbon-coated copper grids using an air displacement micropipette before analysis. The supported catalysts, *i.e.,* TN_01 – TN_05 and RM_4, were not sonicated prior to transfer onto the copper grids as the sonication initially caused the nanoparticles to segregate from the support. However, the samples RM_2 and RM_3 were sonicated for 10 minutes.

All micrographs were analysed using the freeware ImageJ. To obtain crystallite size distributions, 200 – 300 crystallites were counted for each sample in order to obtain a statistically representative size distribution. Also both number- and volume-based average crystallite sizes together with the number- and volume-based standard deviations could be calculated using Equations 4.1 to 4.4 (Bergeret & Gallezot, 1997; National Institute of Standards and Technology, 2013). This volume-based average crystallite size was compared with the average crystallite size obtained by Rietveld refinement, since this average crystallite size is also a volume-based one.

$$\boldsymbol{number-based\ average}\ (\bar{d}_{c,n}) = \frac{\sum_{i=1}^{N} n_i d_i}{N} \qquad \textbf{Equation 4.1}$$

$$\boldsymbol{volume-based\ average}\ (\bar{d}_{c,v}) = \frac{\sum_{i=1}^{N} n_i d_i^4}{\sum_{i=1}^{N} n_i d_i^3} \qquad \textbf{Equation 4.2}$$

$$\boldsymbol{number-based\ standard\ deviation}\ (sd_n) = \sqrt{\frac{\sum_{i=1}^{N} n_i (d_i - \bar{d}_{c,n})^2}{N-1}} \qquad \textbf{Equation 4.3}$$

$$\boldsymbol{volume-based\ standard\ deviation\ (sd_v)} = \sqrt{\frac{\sum_{i=1}^{N} \boldsymbol{n_i d_i^3 \left(d_i - \bar{d}_{c,v}\right)^2}}{\frac{\boldsymbol{N-1}}{\boldsymbol{N}} \sum_{i=1}^{N} \boldsymbol{n_i d_i^3}}} \qquad \textbf{Equation 4.4}$$

The variable $\boldsymbol{d_i}$ is the diameter of crystallite $\boldsymbol{i}$, $\boldsymbol{n_i}$ is the number of crystallites of size $\boldsymbol{d_i}$ and $\boldsymbol{N}$ is the total number of crystallites counted.

4.2.3. Energy-dispersive X-ray (EDX) spectroscopy

To obtain the Co_3O_4 loading in the fresh supported catalysts, elemental analysis was performed using energy-dispersive X-ray (EDX) spectroscopy. A very small amount of each sample was sprinkled on two-sided carbon tape stuck on aluminium stubs. The samples were then coated with carbon for thirty minutes to enhance their conductivity before being sent for analysis. The carbon coating does not interfere with the elemental analysis. After the coating procedure, the samples were taken for analysis in the LEO 1450 SEM/EDX instrument.

4.2.4. Hydrogen temperature-programmed reduction (H_2-TPR)

Temperature-programmed reduction using hydrogen (H_2-TPR) was conducted to monitor the reduction behaviour of the supported Co_3O_4 catalysts. A sample of 100 mg is placed between two pieces of quartz wool in a U-shape quartz reactor. The reduction is conducted on a Micromeritics AutoChem 2910 with a thermal conductivity detector (TCD) for measuring the hydrogen consumption. The sample was firstly dried by flowing argon (flow rate: 10 ml (NTP)/min) through the system with heating to 120 °C (heating rate: 10 °C/min) and holding for sixty minutes at 120 °C. The system was then cooled to 60 °C and after reaching this temperature, 5% hydrogen in argon (flow rate: 50 ml (NTP)/min) was allowed to flow through the sample and the system was heated to 920 °C (heating rate: 10 °C/min).

4.3. *In situ* characterisation of the synthesised $Co_3O_4/\gamma\text{-}Al_2O_3$ catalysts under CO-PROX conditions

4.3.1. Magnetic measurements on the magnetometer

4.3.1.1. Background

Magnetic measurements can be very useful in identifying and quantifying different species present in a sample. Depending on the chemical and physical properties of a particular species; the species can either be referred to as ferromagnetic, antiferromagnetic, paramagnetic or superparamagnetic.

Ferromagnetic materials are attracted by an applied magnetic field (symbol: H, units: T (Tesla) or kOe (kilo-Oersted)) via the parallel alignment of neighbouring electron spins forming microscopic regions called magnetic domains (Buschow, 2001; Kittel, 2004; Serway & Jewett Jr., 2014). Upon removal of this external field, the material or a fraction of it, remains magnetised and the observed magnetisation is called remnant magnetisation (M_{rem}). This behaviour is a result of the strong coupling between the neighbouring electron spins (Serway & Jewett Jr., 2014). Ferromagnetism is temperature-dependent and material-specific therefore, there exists a critical temperature above which ferromagnetic materials lose their ferromagnetic character and become paramagnetic. This critical temperature is called the Curie temperature (T_C). The loss in ferromagnetic behaviour above T_C is a result of an increase in the thermal energy which mitigates the strong interaction between neighbouring spins (Serway & Jewett Jr., 2014).

Antiferromagnetic materials are almost like ferromagnetic materials except that the neighbouring spins align themselves in opposite directions in the presence of an applied field (Buschow, 2001; Kittel, 2004; Serway & Jewett Jr., 2014). Antiferromagnetic behaviour is also temperature-dependent and the critical temperature below which antiferromagnetic behaviour can be observed is called the Néel temperature (T_N). Above this critical temperature, antiferromagnetic materials also become paramagnetic (Serway & Jewett Jr., 2014).

Superparamagnetic behaviour is a special case of ferromagnetism whereby small crystallites (normally in the nanometre range) lose their magnetisation upon removal of an external field. Superparamagnetism is crystallite size-dependent and material-specific therefore, there exists a critical crystallite size whereby a ferromagnetic sample will display superparamagnetic behaviour.

In this study, it is believed that Co_3O_4 would reduce to CoO and ultimately to Co at high temperatures due to the H_2-rich CO-PROX environment (Teng *et al.*, 1999). Co_3O_4 and CoO are antiferromagnetic oxides with a Neel Temperature of 32 K and 291 K, respectively (Kittel, 2005; Mousavand *et al.*, 2009). Metallic Co is ferromagnetic with a Curie temperature of 1403 K (Buschow, 2001). The novel UCT-developed *in situ* magnetometer set-up (Claeys *et al.*, 2010; Fischer *et al.*, 2014) shown in Figure 4.5 was designed for the detection of ferromagnetic and superparamagnetic materials with a detection limit of 0.025 emu (corresponding to 0.14 mg of Co) at 350 °C. The magnetic susceptibility of antiferromagnetic material is orders of magnitude weaker than that of ferromagnetic (and superparamagnetic) materials and therefore, cannot be adequately detected in this *in situ* magnetometer. In this study, the *in situ* magnetometer instrument was therefore, used to detect the presence of metallic Co only. The critical size below which metallic Co is believed to be superparamagnetic is still under debate. Bean and Livingston (1959) reported a theoretical size of 8 nm for hcp cobalt and 28 nm for fcc Co at room temperature. Barbier *et al.* (1998), based on their experimental work, reported that this critical size for cobalt was in the 16 – 20 nm range (without making a distinction between the two allotropes of cobalt *i.e.,* fcc and hcp cobalt).

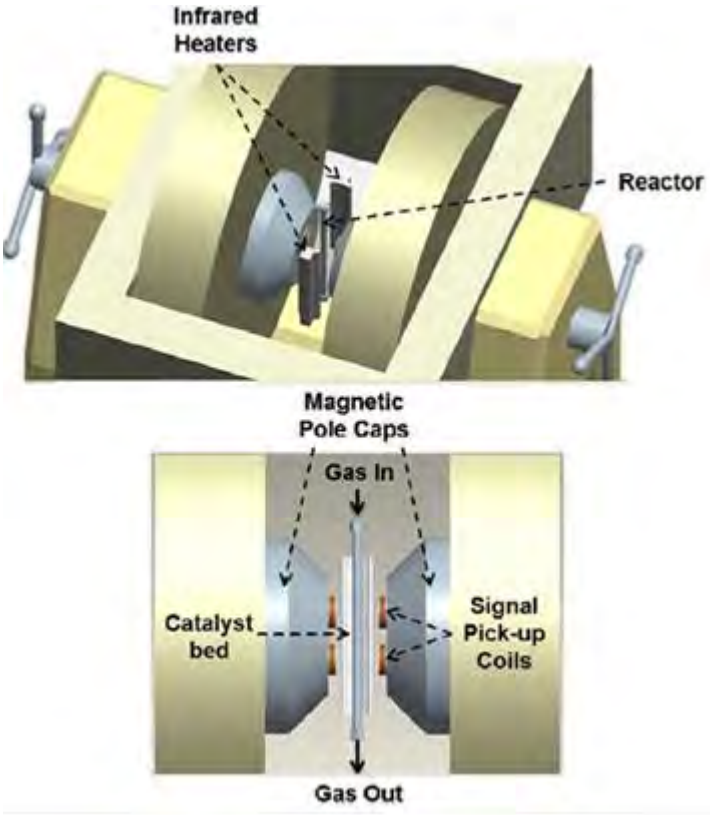

Figure 4.5: *(**top**) Novel UCT-developed in situ magnetometer instrument used for the detection of ferromagnetic and superparamagnetic materials. (**bottom**) Front view showing the stainless steel in situ magnetometer reactor placed between two electro-magnetic pole caps. Note that the front infrared heater is not shown in this view. [From Claeys et al. (2010); Fischer et al. (2014)].*

The strength of the external field required to align superparamagnetic crystallites is strongly dependent on crystallite size *i.e.,* a much stronger external field is required to magnetise very small crystallites than that required for the magnetisation of larger crystallites. Therefore, when varying the strength of the applied field, the magnetisation measured at low fields is a result of the relatively larger crystallites with the magnetisation at higher fields being a cumulative result of both small and large crystallites. This maximum magnetisation measured at high field strengths is called the saturation magnetisation (M_s). Upon removal of the external field (*i.e.,* at 0 T), the crystallites lose their magnetisation as shown in Figure 4.6 (Dalmon, 1994).

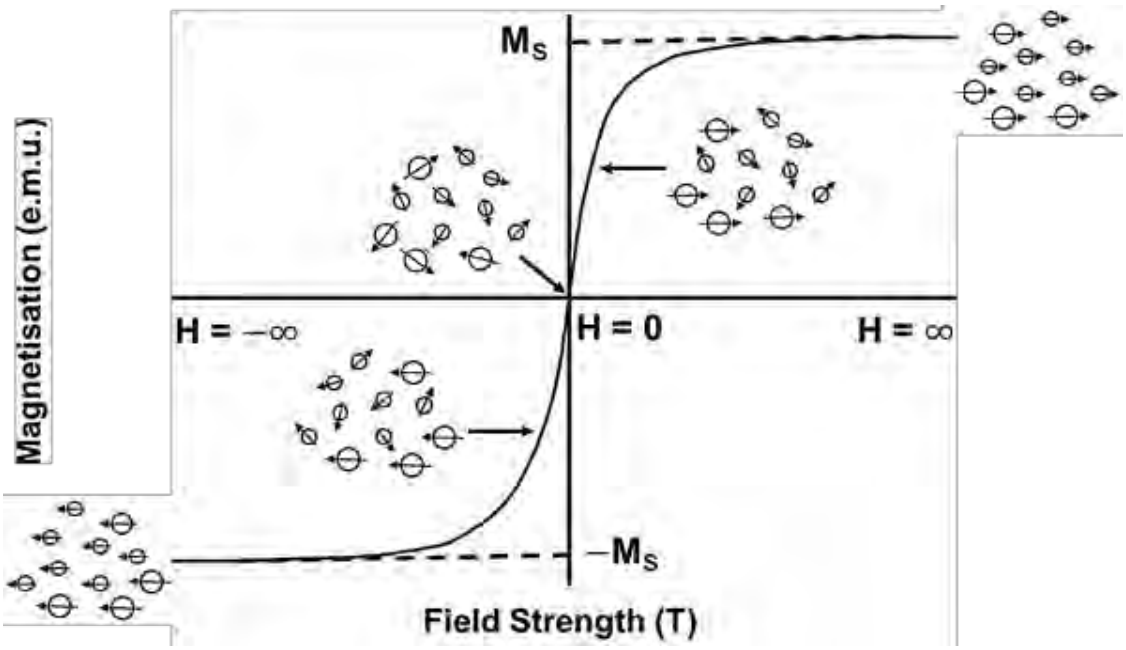

Figure 4.6: *Measured magnetisation of a purely superparamagnetic sample as a function of the applied magnetic field. [Adapted from Dalmon, 1994].*

For a sample which exhibits superparamagnetic behaviour, a crystallite size distribution and average crystallite size can be obtained from the plot shown in Figure above. The Langevin function/Equation shown as Equation 4.5 can be used to obtain a crystallite size distribution via superimposing a number of these Equations according to the contribution of the various crystallite sizes (Dalmon, 1994).

$$\frac{\boldsymbol{M}}{\boldsymbol{M_s}} = \coth\left(\frac{\boldsymbol{\rho \cdot \sigma_s \cdot \frac{\pi}{6} \cdot d^3 \cdot H}}{\boldsymbol{k_B \cdot T}}\right) - \left(\frac{\boldsymbol{k_B \cdot T}}{\boldsymbol{\rho \cdot \sigma_s \cdot \frac{\pi}{6} \cdot d^3 \cdot H}}\right) \qquad \textbf{Equation 4.5}$$

$\frac{\boldsymbol{M}}{\boldsymbol{M_s}}$ is the ratio of the measured sample magnetisation to the saturation magnetisation, $\boldsymbol{\rho}$ is the density of the magnetic material and $\boldsymbol{\sigma_s}$ is the specific saturation magnetisation of the magnetic material (for cobalt: 168 emu.g^{-1} at room temperature (Niu *et al.*, 2003)) which is independent of crystallite size (Selwood, 1975). The variable $\boldsymbol{d}$ is the crystallite diameter, $\boldsymbol{H}$ is the applied magnetic field, $\boldsymbol{k_B}$ is the Boltzmann constant and $\boldsymbol{T}$ is the temperature.

As mentioned above, ferromagnetic materials or crystallites have a remnant magnetisation (M_{rem}) upon removal of the applied external field (*i.e.,* at 0 T). So when varying the external field and measuring the magnetisation, a hysteresis plot is obtained as the one shown in Figure 4.7.

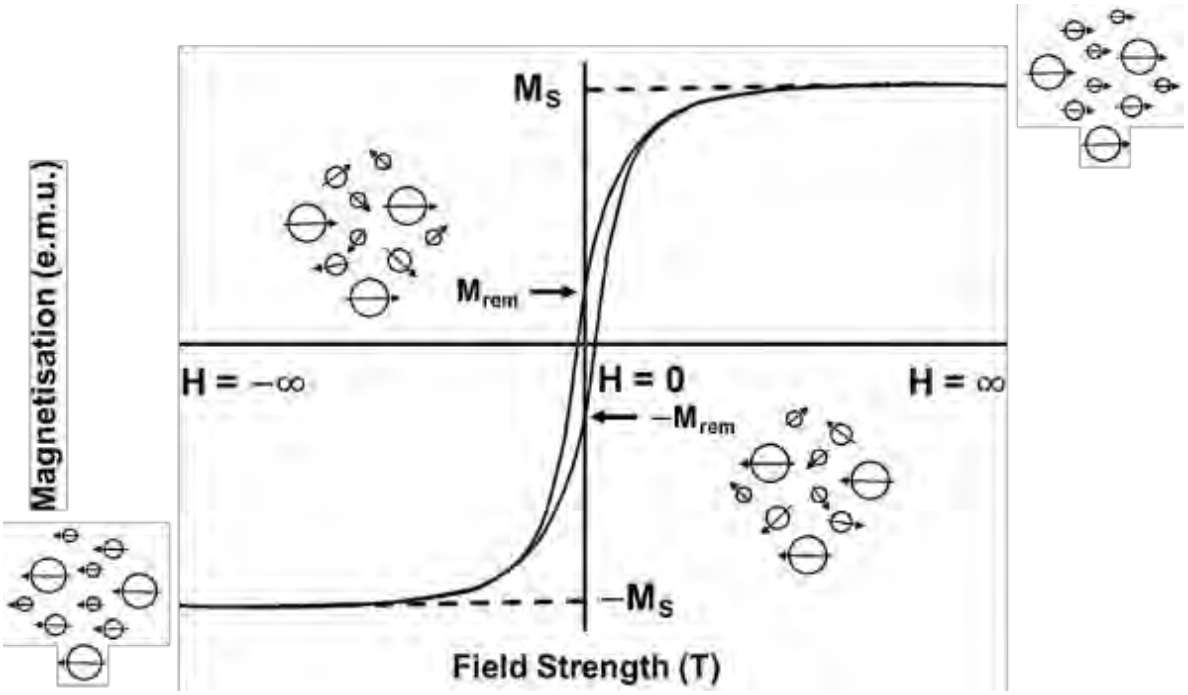

Figure 4.7: *Hysteresis plot obtained when the magnetisation of a ferromagnetic sample is measured as function of the applied magnetic field. [Adapted from Dalmon, 1994].*

From this hysteresis measurement, a crystallite size distribution cannot be obtained using the Langevin Equation but the relative amount of material displaying remnant magnetisation (γ) at 0 T in a catalyst sample can be obtained and is calculated using Equation 4.6 (Dalmon, 1994). Also, this quantity can give qualitative information about the crystallite size (Claeys *et al.*, 2015).

$$\gamma\ (wt.-\%) = \frac{2M_{rem}}{M_s} \times 100 \qquad \textbf{Equation 4.6}$$

Where $\boldsymbol{\gamma}$ is the amount of material displaying remnant magnetisation relative to the total amount of ferromagnetic material present in a sample. This material comprises of crystallites having a crystallite size which is greater than the critical size for superparamagnetism. $\boldsymbol{M_{rem}}$ is the sample's remnant magnetisation and $\boldsymbol{M_s}$ is the sample's saturation magnetisation.

4.3.1.2. Catalyst testing unit

Depicted in Figure 4.8 is the set-up of the catalyst testing unit used for the magnetic measurements under CO-PROX reaction conditions. Among other things, it shows the different gas streams and the reactor used for the magnetic measurements. CO, H_2 and N_2 were fed from one gas cylinder (AFROX (0.97% CO, 54.43% H_2, 44.60% N_2)) whereas, O_2 was fed from a different gas cylinder as synthetic air (Air products (21% O_2 in N_2, 99.999 % purity)). Therefore, only mass flow controllers MFC2 and MFC3 (Brooks Instruments) were used for feeding these gases to the system and the 3-way valves 3WV4 and 3WV5 were used for controlling the flow into the reactor. CO_2 and H_2O were not co-fed as this study aimed at looking at the effect of H_2 (among other things) on the catalytic performance and reducibility of supported Co_3O_4 catalysts. As discussed in sub-section 2.4.1, CO_2 and H_2O can also affect the performance of CO-PROX catalysts (Guo & Liu, 2007; Monyanon *et al.*; 2007; Park *et al.*, 2004) and so having these gases present may mask the sole effect of H_2 which is targeted in this study.

The experiments were all performed at atmospheric pressure, the total gas flow was 78 ml (NTP)/min or 100 ml (NTP)/min and the amount of catalyst loaded in the reactor was varied between 1.0 and 1.5 g in order to achieve the same Co_3O_4 loading in the reactor and to compensate for the differences in the Co_3O_4 loadings as determined by EDX. The gas volumetric ratio 1:1:52:46 of $CO/O_2/H_2/N_2$ was used. The reaction temperature was increased from 50 to 350 °C using a 1 °C/min heating ramp. The temperature was held for an hour at 50 °C and every 25 °C up to 350 °C. After the hour at 350 °C had lapsed, the reactor was cooled back down to 50 °C with the temperature held for an hour at every 25 °C. Magnetisation measurements were taken every 10 minutes during the whole experiment and magnetisation measurements were taken at -2, 0, 2 T and again at 0 T (*i.e.,* -20, 0, 20 kOe and again at 0 kOe). This allowed to determine the saturation magnetisation ($\boldsymbol{Ms}$) and the remnant magnetisation

(M_{rem}), with the former being used to determine the degree of reduction (see Appendix A). At 50 °C after the completion of the run, a single hysteresis measurement was taken by varying the magnetic field strength from -2 to 2 T and back to -2 T (*i.e.,* -20 to 20 kOe and back to -20 kOe) in 65 steps. This ultimately allowed to determine **γ**.

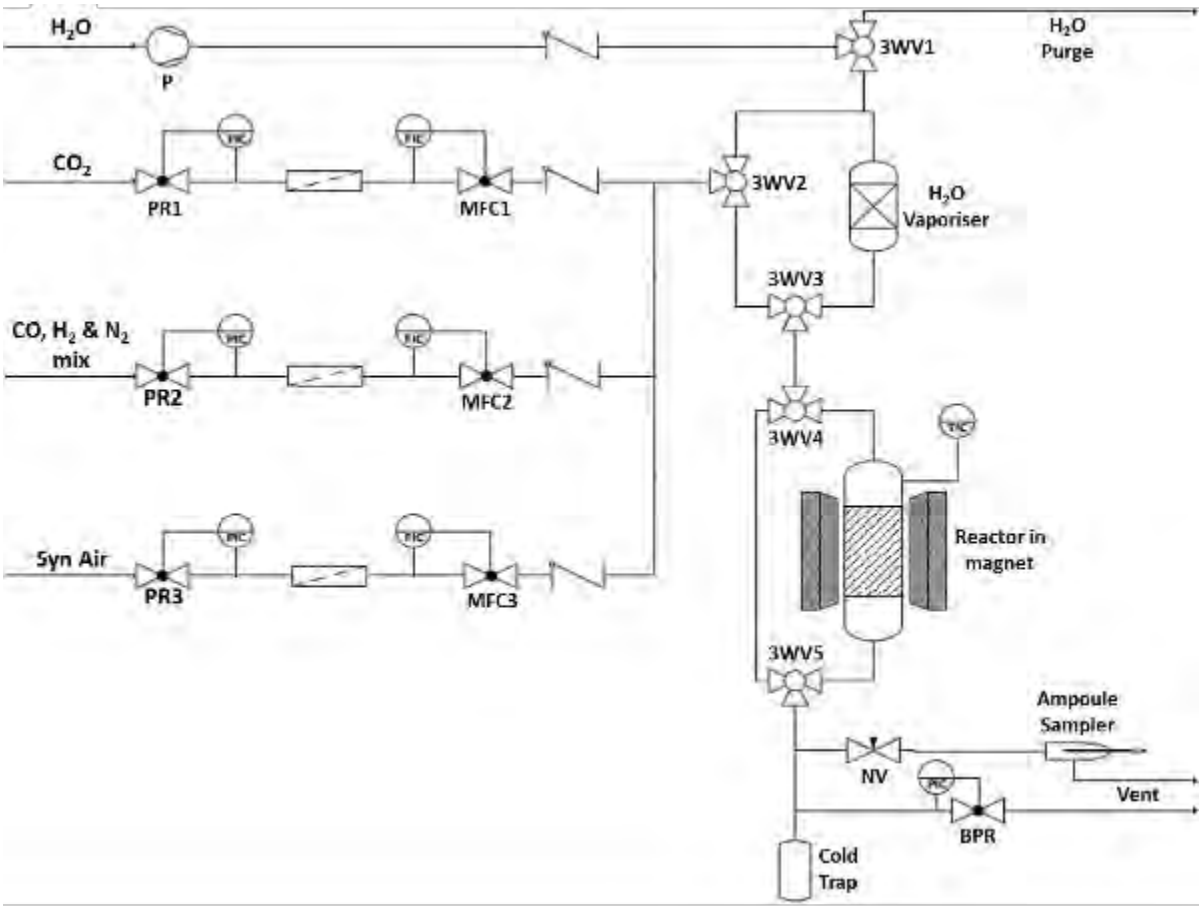

Figure 4.8: *Set-up of the catalyst testing unit used for the in situ CO-PROX experiments in the magnetometer.*

4.3.1.3. Reactor set-up

The set-up for the reactor used for the magnetic measurements is depicted in Figure 4.9. A stainless steel reactor (O.D.: 0.5", I.D.: 9.7 mm) was placed between two pole caps of the electro-magnet (Bruker Analytik GmbH; maximum field strength (at a 4.8 cm air gap): 2 T (*i.e.,* 20 kOe) and contained a brass frit which supported the catalyst bed and prevented the loss of

catalyst through the reactor. The reactor tube was spray-painted with high-temperature black paint to increase the reactor's heat absorption from the two infrared heaters. Above this brass frit was a layer of glass wool onto which the measured amount of catalyst was placed. Above the catalyst bed was another layer of glass wool. Then a non-magnetic thermocouple (Pt 100 element) was placed above the glass wool and to ensure the thermocouple's radially central positioning in the reactor, a star-like guide was used. Silicon carbide was used to fill up the reactor and to also help in pre-heating the gases.

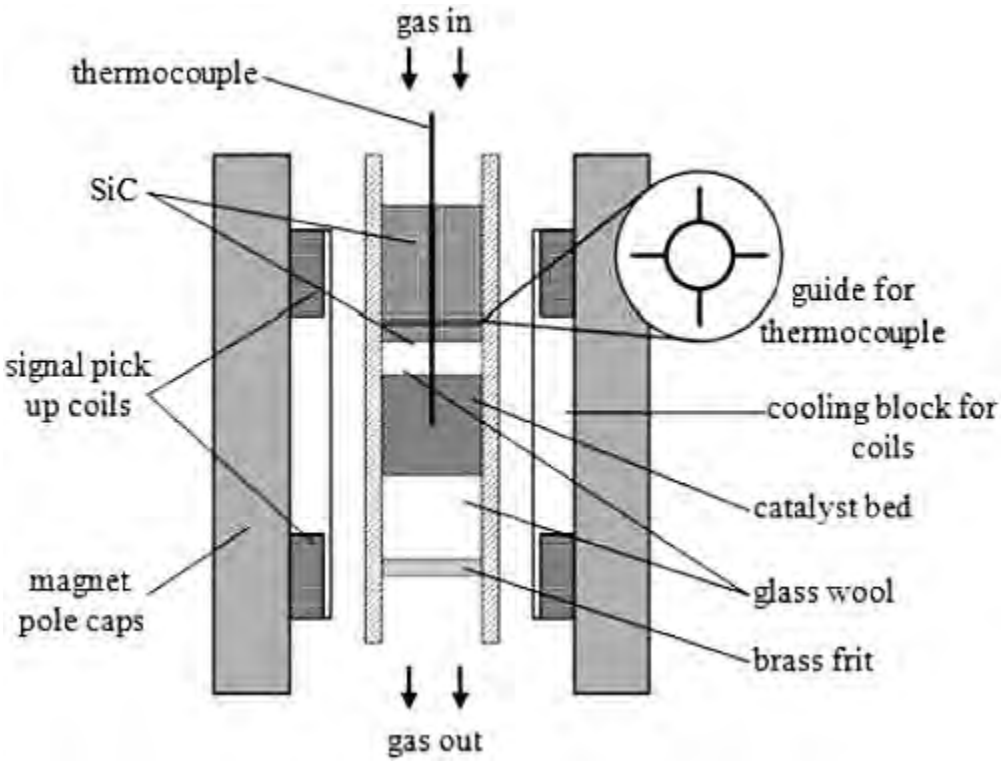

Figure 4.9: *Front view of a loaded in situ magnetometer reactor placed between two electro-magnetic pole caps. [From Claeys et al. (2010); Fischer (2011)].*

The loaded reactor was placed on the aluminium holding bracket equidistant from the two infrared heaters which were used to heat the reactor. The electro-magnet supplied a homogenous field which could be accurately controlled and measured via a field probe (not shown). The control of the field strength from -2 to 2 T and back to -2 T allowed for the recording of a hysteresis. For ideal signal strength, it was important that the catalyst bed be placed exactly in the centre of the detection coils on the pole caps of the electro-magnet as shown in Figure 4.10. This was done by adjusting the vertical position of the reactor using the

aluminium holding bracket. This brack*et al*so facilitated the movement of the reactor (via an electromotor; amplitude: 4 cm, frequency: 2 Hz) to induce a signal/voltage from the magnetised catalyst in the pick-up coils. To allow the movement of the reactor and also gas flow to and from the reactor, flexible 1/16-inch tubing was used. The magnetisation of the sample is proportional to the induced signal measured by the pick-up coils. The set-up was calibrated with a known amount of pure metallic cobalt powder (*i.e.,* 0.1 g) and the procedure involved varying the temperature at a constant external field of 2 T and measuring the sample magnetisation. As a result, a calibration curve was obtained and this later enabled the determination of the degree of reduction of Co_3O_4 to metallic cobalt (see Appendix A).

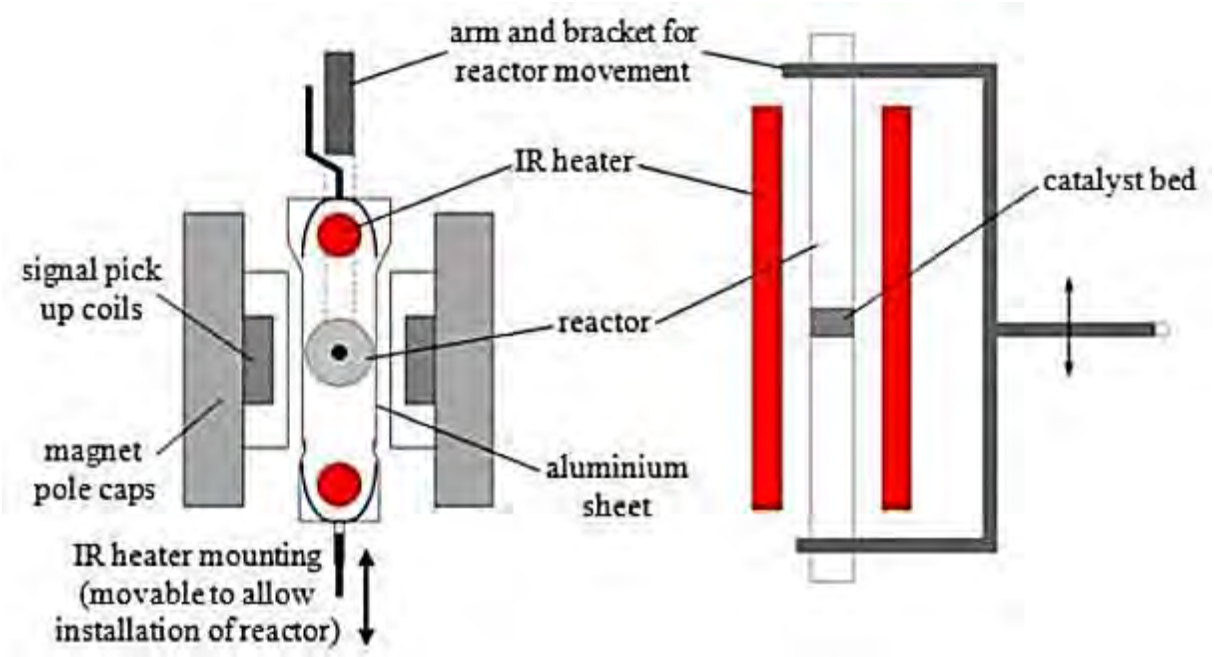

Figure 4.10: *In situ magnetometer reactor set-up. (**left**) Top view and (**right**) side view. [From Claeys et al. (2010); Fischer (2011)].*

4.3.2. Powder X-ray diffraction (PXRD)

Powder X-ray Diffraction measurements under CO-PROX reaction conditions were carried out using a novel UCT-developed *in situ* capillary cell reactor (Claeys & Fischer, 2013; Fischer *et al.*, 2014) which was mounted on to the Bruker D8 Advance X-ray diffractometer with a cobalt source (λ = 1.78897 Å). This *in situ* instrument was used as a complementary technique for monitoring the bulk phase changes of Co_3O_4 to CoO and to Co. (Note: metallic Co can be detected at much lower mass fractions in the magnetometer than those that can be detected in the PXRD capillary cell instrument). This technique can also give information on the average crystallite size and the changes thereof. The capillaries used were made up of borosilicate (Capillary Tube Supplies LTD, UK) and had a length of 75 mm, a wall thickness of 0.02 mm and a tube opening of 1.0 mm. The catalyst bed length in the capillary reactor was limited to 15 mm along the centre as this length serves as the isothermal region of the reactor (Clapham, 2012). The catalyst bed was therefore, supported by two pieces of glass wool which filled up the reactor on each side. An internal thermocouple (Temperature Controls, RSA), with a diameter of 0.5 mm and a maximum-rated operating temperature of 1000 °C, was placed inside the capillary reactor as shown Figure 4.11 below, with its tip in close contact with the catalyst bed but outside the path of the X-rays.

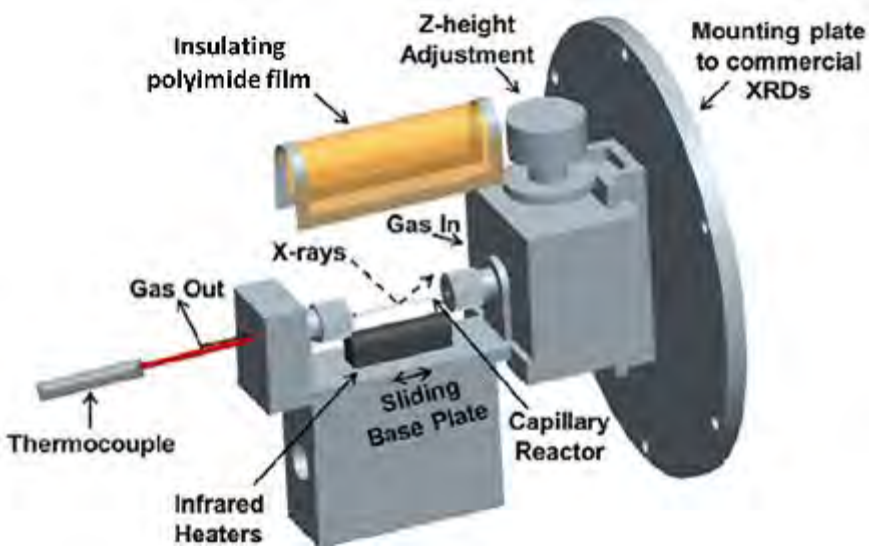

Figure 4.11: *The novel UCT-developed in situ PXRD capillary cell used for monitoring the bulk phase changes in the catalyst under CO-PROX conditions. [From Claeys & Fischer (2013); Fischer et al. (2014)].*

The capillary reactor was placed between the X-ray source and detector; was covered with a polyimide film (DuPont, Kapton, RS components) attached to aluminium heat shields using magnetic strips (Technical + General Distribution, RSA) as shown in Figure 4.12 on the next page. The polyimide film does not interfere with the X-rays and the aluminium heat shields, which could interfere with the X-rays, were attached to the polyimide film such that they are not in the path of the X-rays.

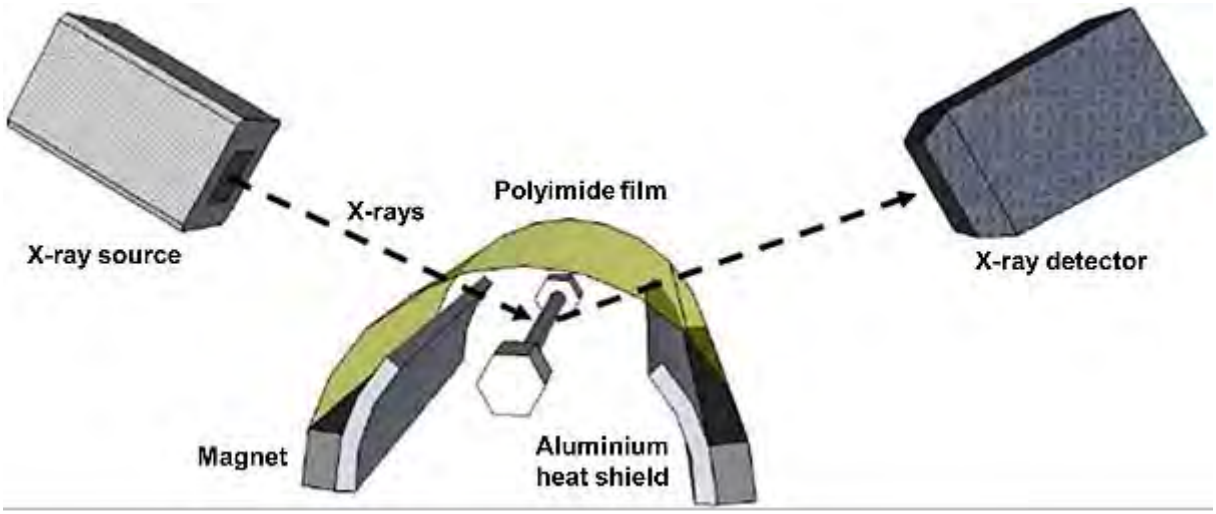

Figure 4.12: *Front-view of the covered in situ PXRD capillary cell reactor. Notice that the polyimide film does not interfere with the X-rays and also that the aluminium heat shields are positioned away from the path of the X-rays. [From Clapham (2012)].*

The maximum operating temperature and pressure of these capillaries is 500 °C and 25 bar, respectively, which made them suitable for use under CO-PROX reaction conditions. The scan range used was 35 ° < 2θ < 95 ° and the total time per scan was 7.28 minutes (with a 2.72 minute delay between scans, a step size of 0.03083045 ° and a time per step of 0.2 seconds). The scan time was kept this short so to minimise the effect of phase changes during a scan. Scans were recorded from 50 °C and then at every 25 °C up to 350 °C (heating rate 1 °C/min). The reactor was cooled down to 50 °C with the scans also being taken every 25 °C from 350 °C. Six scans were taken in total at each temperature with a holding time of sixty minutes. The CO-PROX gas feed used for these experiments was the same as in the magnetometer but the total gas flow was reduced to 1.3 – 1.6 ml (NTP)/min due to the fact that a maximum total mass

of approximately 15 mg could be loaded into the borosilicate capillary reactors. The space velocity was therefore, kept constant and was similar to that used for the magnetic studies.

4.3.3. Product analysis

Online gas chromatography was conducted using an Agilent Technologies 490 micro GC fitted with a thermal conductivity detector for detecting CO, O_2, H_2, CO_2, CH_4 and N_2. The micro GC had three modules which had different columns – the first and second column were 10 m and 20 m Molecular Sieve 5A PLOT columns, respectively. The first column had Ar as the carrier gas and was mainly used for the detection of H_2. The second column had H_2 as the carrier gas and was used for the detection of O_2, N_2, CH_4 and CO. The third column was a 10 m PoraPlot Q column which also had H_2 as the carrier gas and was mainly used for the detection of CO_2. The software programme Varian Galaxie Chromatography Data System 1.9.3.2 was used to control the gas chromatograph analysis and to calculate the peak areas of each gas exiting the reactor. The error in the measurements on the said microGC instrument is known to be between 2 – 3%.

The GC was calibrated using two calibration gas cylinders; one having a mixture of 20.1% CO, 9.8% CO_2, 15.2% CH_4, 10.1% Ar, 5.2% N_2 in H_2 (AFROX); the other gas cylinder had synthetic air (Air products (21% O_2 in N_2, 99.999 % purity)). From the chromatograms, response factors for each gas (except for N_2 and Ar) were calculated (see Equation 4.7) using N_2 as the reference since it was present in both cylinders and was the only gas that would not get consumed under reaction conditions. To calculate the molar flow rate for each gas, Equation 4.8 was used.

$$\boldsymbol{F_i = \frac{A_{N_2} n_{i,in}}{A_i n_{N_2,in}}} \qquad \textbf{Equation 4.7}$$

$$\boldsymbol{n_{i,out} = F_i \frac{A_i n_{N_2,in}}{A_{N_2}}} \qquad \textbf{Equation 4.8}$$

$\boldsymbol{F_i}$ is the response factor of gas component $\boldsymbol{i}$ with reference to nitrogen. $\boldsymbol{A_{N_2}}$ is the calculated peak area of nitrogen and $\boldsymbol{A_i}$ is the calculated peak area of gas component $\boldsymbol{i}$. The variable $\boldsymbol{n_{N_2,in}}$

is the molar gas flow rate of nitrogen and $\boldsymbol{n_{i,in}}$ is the molar gas flow rate of gas component $\boldsymbol{i}$ entering the system during the calibrations. Finally, $\boldsymbol{n_{i,out}}$ is the molar gas flow rate of gas component $\boldsymbol{i}$ exiting the reactor under reaction CO-PROX conditions. The results of the calibration can be found in Appendix B.

The total CO conversion ($\boldsymbol{X_{CO}}$), CO_2 yield ($\boldsymbol{Y_{CO_2}}$) and selectivity from O_2 ($\boldsymbol{S_{CO_2}^{O_2}}$), the CH_4 yield ($\boldsymbol{Y_{CH_4}}$) were calculated using Equations 4.9 to 4.12:

$$X_{CO}\ (\%) = \frac{n_{CO,in} - n_{CO,out}}{n_{CO,in}} \times 100 \qquad \textbf{Equation 4.9}$$

$$Y_{CO_2}\ (\%) = \frac{n_{CO_2,out}}{n_{CO,in}} \times 100 = \frac{n_{CO,in} - n_{CO,out} - n_{CH_4,out}}{n_{CO,in}} \times 100 \qquad \textbf{Equation 4.10}$$

$$S_{CO_2}^{O_2}\ (\%) = \frac{n_{CO_2,out}}{2 \cdot \left(n_{O_2,in} - n_{O_2,out}\right)} \times 100 = \frac{n_{CO,in} - n_{CO,out} - n_{CH_4,out}}{2 \cdot \left(n_{O_2,in} - n_{O_2,out}\right)} \times 100 \qquad \textbf{Equation 4.11}$$

$$Y_{CH_4}\ (\%) = \frac{n_{CH_4,out}}{n_{CO,in}} \times 100 = \frac{n_{CO,in} - n_{CO,out} - n_{CO_2,out}}{n_{CO,in}} \times 100 \qquad \textbf{Equation 4.12}$$

Where $\boldsymbol{n_{CO,in}}$and $\boldsymbol{n_{O_2,in}}$ are the molar gas flow rates of CO and O_2, respectively, entering the reactor under reaction conditions. The variables $\boldsymbol{n_{CO,out}}$, $\boldsymbol{n_{O_2,out}}$, $\boldsymbol{n_{CO_2,out}}$ and $\boldsymbol{n_{CH_4,out}}$ are the molar gas flow rates of CO, O_2, CO_2 and CH_4, respectively, exiting the reactor under reaction conditions.

Oxygen can also potentially oxidise H_2 to H_2O, but for the experiments performed in this study, H_2 conversions to H_2O were not calculated since H_2 was present in very high amounts relative to oxygen (*i.e.,* 52:1 H_2:O_2) and therefore, the changes in its concentration as a result of oxidation were too little to be measured accurately. It should be noted that to fully convert oxygen to water, based on Equation 2.5, a volume of hydrogen twice that of oxygen will be required. In these experiments, this volume corresponds to a maximum of approximately 3.8% of the total volume of H_2 fed. Since there is a competing reaction, *i.e.,* CO oxidation, the conversion of H_2 can be expected to be much lower than 3.8% especially at low temperatures (*i.e.,* below 175 – 200 °C). Nonetheless, it is worth noting that the H_2O selectivity from O_2 ($\boldsymbol{S_{H_2O}^{O_2}}$) can be expected to be $\boldsymbol{100 - S_{CO_2}^{O_2}}$.

Chapter 5: *Ex situ* Characterisation Results

5.1. Powder X-ray diffraction (PXRD)

5.1.1. Variation of the crystallite size of Co_3O_4

The reverse micelle technique was used to synthesise Co_3O_4 nanoparticles of different sizes. Parameters including the oil-to-surfactant ratio, water-to-surfactant ratio and mass/concentration of the cobalt precursor were important in achieving the different sizes. Five different sizes were targeted and these were allowed to vary in the 3 – 15 nm range. Powder X-ray diffraction (PXRD) measurements were helpful in confirming the cobalt phase present in the unsupported and supported catalysts as well as confirming the crystallite sizes in each case. From the PXRD patterns shown in Figure 5.1, it is clear that Co_3O_4 is the only cobalt phase present in the unsupported catalysts. Figure 5.2 shows that Co_3O_4 is still the only cobalt phase present together with the γ-Al_2O_3 support in the supported catalysts. All the Co_3O_4 peak positions in each obtained diffraction pattern of the unsupported and supported catalysts corresponds very well with those of the literature diffraction pattern of Co_3O_4. The peak intensity and width can together give a qualitative indication of the crystallite. As seen in Figures 5.1 and 5.2, when the intensity of the Co_3O_4 peak increases, the peak gets narrower. This behaviour implies an increase in the crystallite size of the Co_3O_4 nanoparticles between the different samples.

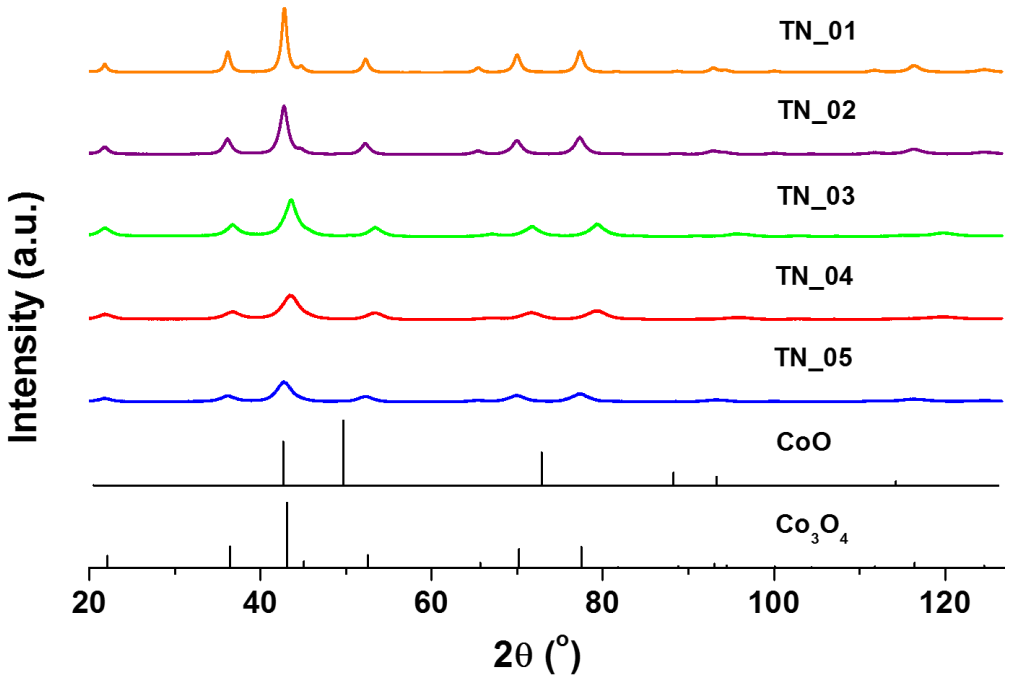

Figure 5.1: *PXRD patterns of the five catalysts (in the unsupported state) with varied Co_3O_4 average crystallite sizes including the reference diffraction patterns of Co_3O_4 and CoO.*

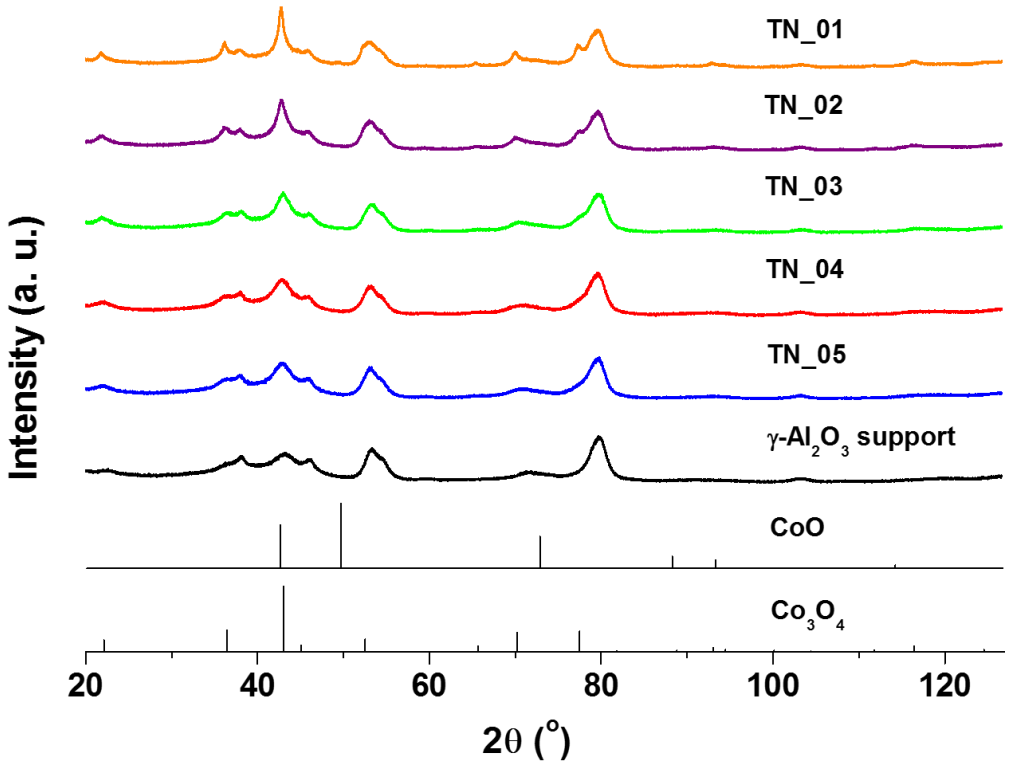

Figure 5.2: *PXRD patterns of the five catalysts (in the supported state) with varied Co_3O_4 average crystallite sizes including the reference diffraction patterns of Co_3O_4 and CoO, together with the recorded spectrum of the γ-Al_2O_3 support.*

The TOPAS 4.1 software program was then used to determine the actual crystallite size of Co_3O_4 and its loading on the support. TOPAS 4.1 uses Rietveld refinement to acquire this information and the method PONCKS (Scarlett & Madsen, 2006) further enables the determination of the Co_3O_4 loading. It is important to note that the average crystallite size obtained here is volume-based (the same applies to the size obtained using the Scherrer Equation). Table 5.1 shows the calculated average sizes of the Co_3O_4 crystallites in the unsupported and supported samples of TN_01 – TN_05. The sizes of the Co_3O_4 crystallites in the unsupported samples were not expected to change upon supporting due to the mild conditions used during the supporting of the crystallites (see sub-section 4.1.1). As it can be seen from the data in Table 5.1, the average crystallite sizes remained significantly unchanged indeed after supporting. The data in this table reflects on the effect of varying the different properties of the reverse micelle solutions prepared *i.e.,* o/s and w/s ratios as well as the amount of the cobalt precursor (see Table 4.1), on the final crystallite size. The final average sizes obtained were within the targeted size range and the Co_3O_4 loadings were very close to the targeted 10 wt.-%.

Table 5.1: *PXRD average Co_3O_4 crystallite size for TN_01 – TN_05 both in the unsupported and supported state and the calculated Co_3O_4 loading in the supported catalysts.*

Sample Name	Targeted size (nm)	Actual size[a]: unsupported (nm)	Actual size[b]: supported (nm)	Co_3O_4 loading (wt.-%)
TN_01	13.0 – 15.0	15.1	15.3	9.1
TN_02	10.0 – 12.0	9.9	10.2	9.9
TN_03	7.0 – 9.0	7.2	7.5	8.9
TN_04	4.0 – 6.0	5.3	5.1	8.9
TN_05	3.0 – 5.0	4.3	4.5	8.7

[a] obtained by Rietveld refinement in Topas 4.1

[b] obtained by applying the PONKCS method and Rietveld refinement in Topas 4.1

5.1.2. Alteration of the support-addition method

When altering the support-addition method, it was believed that the metal-support interactions could also be altered. Fischer *et al.* (2012) reported that early contact of the γ-Al_2O_3 support with the cobalt precursor still dissolved in the polar phase of the microemulsion, gave rise to cobalt-based nanoparticles with very strong interactions with the support. It also gave rise to very small crystallites of Co_3O_4 between 3.0 and 5.0 nm. With these strong metal-support interactions, Fischer *et al.* further reported a higher concentration of Co^{2+} species on the surface based on XPS (X-ray Photoelectron Spectroscopy) results and attributed this to the presence of cobalt aluminate- ($CoAl_2O_4$-) like species on the surface. Synthesising the $Co(OH)_2$ or the Co_3O_4 nanoparticles, respectively, and then contacting them with the γ-Al_2O_3 support, did not give rise to strong metal-support interactions (Fischer *et al.* 2012). In this study, the support-addition method was also altered so to change the metal-support interactions and to then investigate the effect this has on the catalytic performance and reducibility of Co_3O_4. The goal was to also achieve similar crystallite sizes of Co_3O_4 in each catalyst so to minimise the effect of the varying sizes.

The PXRD patterns in Figure 5.3 are for the four catalysts synthesised in this series. By looking at the relative intensities of the peaks and peak positions, there are strong indications for the presence of Co_3O_4 in RM_1. The peaks are broad and have relatively low intensities which is a good indication for the presence of small Co_3O_4 crystallites. The PXRD patterns of RM_2, RM_3 and RM_4 displayed no obvious indication for the presence of Co_3O_4 as the γ-Al_2O_3 peaks dominated throughout each of the three patterns. However, as seen in

Table 5.2, the calculated crystallite sizes of Co_3O_4 in RM_1 - RM_4 were all in the 3 – 5 nm size range as targeted. However, the calculated loading of Co_3O_4 (determined using TOPAS 4.1) in the samples RM_2 – RM_4 were significantly lower than the targeted 10 wt.-%.

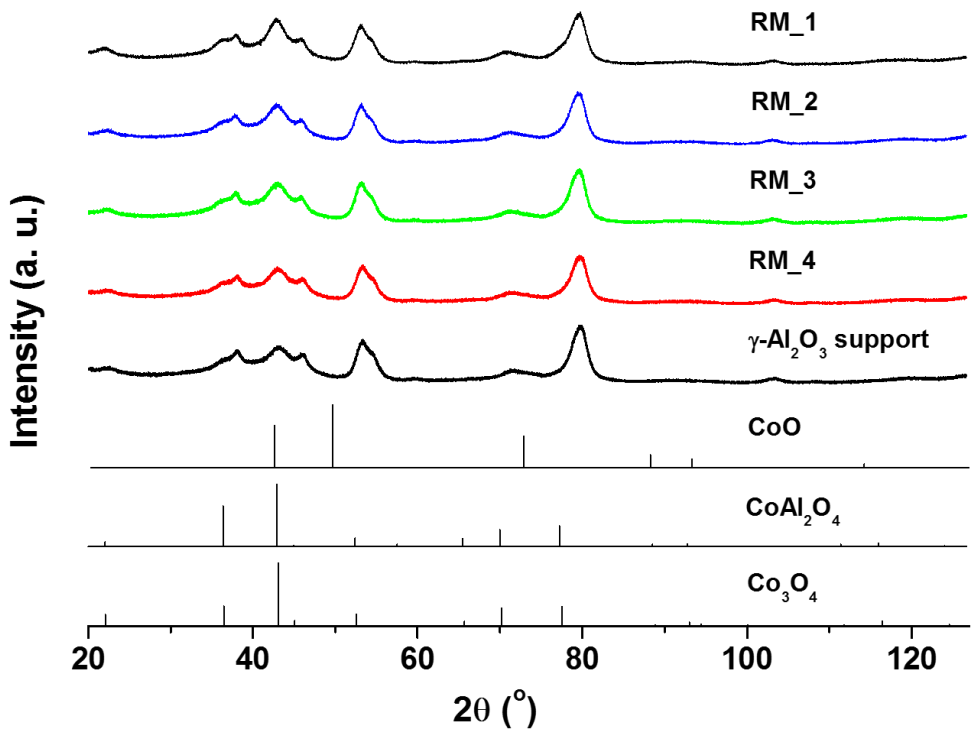

Figure 5.3: *PXRD patterns of the four catalysts with different metal-support interactions including the reference patterns for CoO, $CoAl_2O_4$ and Co_3O_4; as well as the recorded patterns of the γ-Al_2O_3 support.*

Table 5.2: *Obtained average Co_3O_4 crystallite sizes and Co_3O_4 loading from Topas 4.1 for RM_1 – RM_4.*

Sample Name	Targeted size (nm)	Actual size[a] (nm)	Co_3O_4 loading[b] (wt.-%)
RM_1 (TN_05)	3.0 – 5.0	4.5	8.7
RM_2	3.0 – 5.0	3.5	6.2
RM_3	3.0 – 5.0	3.8	5.8
RM_4	3.0 – 5.0	4.2	4.3

[a] obtained by Rietveld refinement in Topas 4.1

[b] obtained by applying the PONKCS method and Rietveld refinement in Topas 4.1

The lower loadings may be explained by the differences in the respective synthesis procedures followed. To obtain RM_2 and RM_3, one needs to rely on the assumption that all the precursor material in the microemulsion gets impregnated into the support. Also, one needs to assume that no material is lost during the extensive washing procedure. For producing RM_4, the assumption made here is that all precursor material gets fully converted to $Co(OH)_2$ and that no particles are lost during the extensive washing procedure before being deposited onto the support. The small crystallite sizes and low loadings could explain the appearance of these three patterns.

The $CoAl_2O_4$ phase is also included as a reference pattern in Figure 5.3. This was done so to visually identify the presence of this species particularly in RM_2 and RM_3 (Fischer *et al.*, 2012). Possibly due to its low mass fraction, small crystallite size or absence, it was not possible to identify it even when using Rietveld refinement software Topas 4.1. As already mentioned, Fischer *et al.* (2012) from their XPS experimental results found evidence for the presence of surface $CoAl_2O_4$-like species. It may be possible that these species were also present on the support surface of RM_2 and RM_3; but could not be detected by PXRD as it is a bulk technique.

5.2. Transmission Electron Microscopy (TEM)

5.2.1. Variation of the crystallite size of Co_3O_4

Transmission electron microscopy (TEM) was used to confirm the average crystallite size of the unsupported and supported Co_3O_4 nanoparticles and to obtain size distributions in each case. TEM was also helpful in giving indications on the morphology of the crystallites and also showing how the nanoparticles were dispersed on the support. The freeware ImageJ was used to view and measure 200 - 300 crystallites in each sample from the micrographs obtained. Figure 5.4 shows the selected micrographs of TN_01, TN_03 and TN_05 in the unsupported state. (See Appendix C for the corresponding micrographs of TN_02 and TN_04). The crystallites mainly appear spherical in appearance (with some crystallites displaying slight

deviations from this morphology) and this was ultimately assumed when the volume-based average crystallite sizes were calculated. The crystallites had a tendency to agglomerate even after the 10-minute sonication performed prior to the analysis. However, it was still reasonably possible to isolate single crystallites and measure them. Figure 5.5 shows the number-based TEM size distribution emanating from the micrographs of the unsupported material and it can be seen that the distribution is reasonably narrow for all catalysts with some widening as the targeted average crystallite size increases.

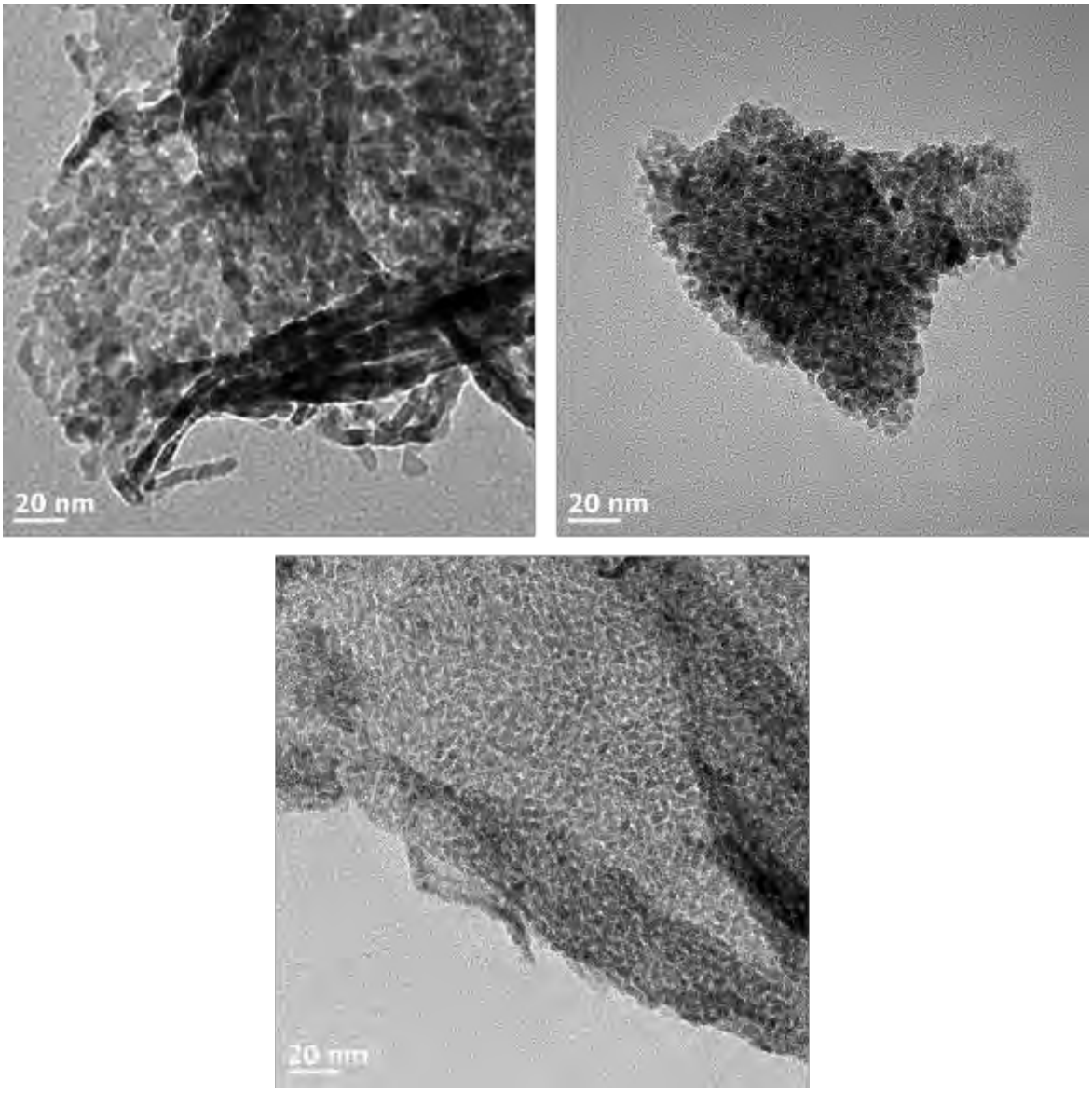

Figure 5.4: *TEM micrographs of the fresh samples of (top-left) TN_01, (top-right) TN_03 and (bottom) TN_05 in the unsupported state.*

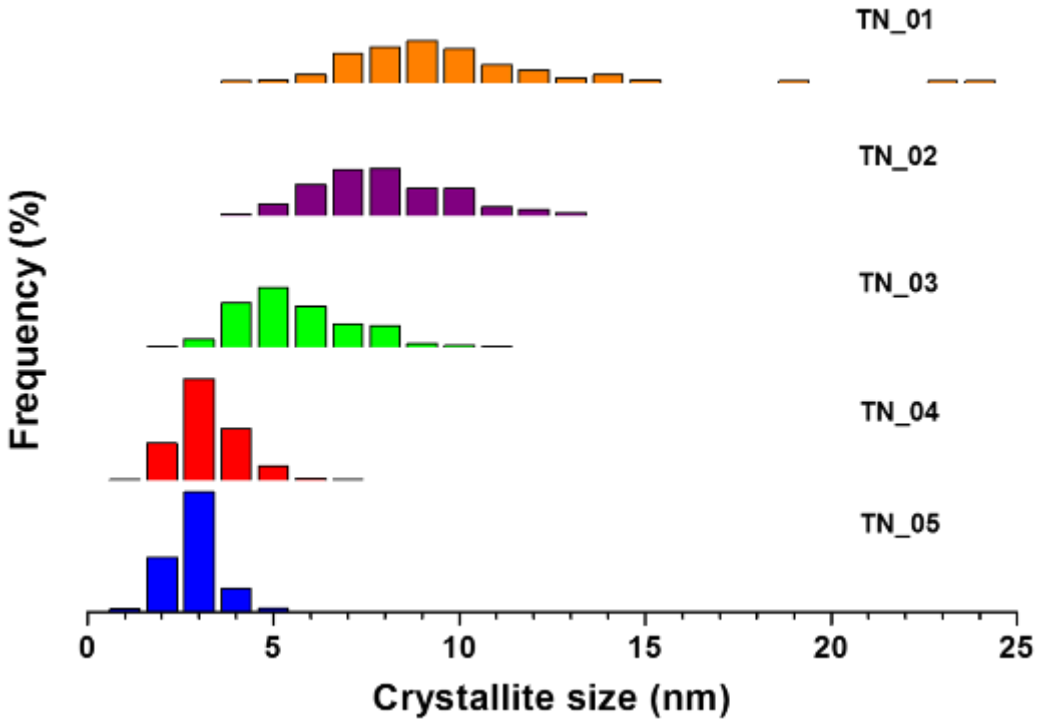

Figure 5.5: *Number-based size distributions of the fresh samples of TN_01 – TN_05 in the unsupported state obtained by means of TEM analysis.*

Eastoe *et al.* (2006) reported that at low water-to-surfactant ratios, there is less intermicellar exchange resulting in a decreased growth rate. As the ratio increases, the film surrounding the micelles becomes more fluid, allowing for greater intermicellar exchange and an increased growth rate, which may contribute to the wider size distributions obtained for the samples with larger crystallites.

Table 5.3 shows the number- and volume-based average crystallite sizes of Co_3O_4 for each unsupported sample. The results in this table reflect on the effect of varying the different properties of the reverse micelle solutions prepared *i.e.,* o/s and w/s ratios as well as the amount of the cobalt precursor (see Table 4.1), on the final crystallite size. The data further shows that the final average sizes were within the desired size range.

Table 5.3: *Number- and volume-based average Co_3O_4 crystallite sizes for TN_01 – TN_05 obtained by TEM analysis in the unsupported state.*

Sample Name	Targeted size (nm)	Actual size[a] (nm)	Actual size[b] (nm)
TN_01	13.0 – 15.0	10.1 ± 2.8	13.8 ± 3.2
TN_02	10.0 – 12.0	8.5 ± 1.7	9.5 ± 1.9
TN_03	7.0 – 9.0	6.1 ± 1.5	7.2 ± 1.6
TN_04	4.0 – 6.0	3.8 ± 0.8	4.5 ± 1.0
TN_05	3.0 – 5.0	3.3 ± 0.6	3.7 ± 0.7

[a] TEM number-based average crystallite sizes obtained using Equations 4.1 and 4.3

[b] TEM volume-based average crystallite sizes obtained using Equations 4.2 and 4.4

The supported catalysts were relatively harder to analyse by TEM as the contrast between the Co_3O_4 crystallites and those of the γ-Al_2O_3 was rather poor as it can be seen in Figure 5.6. Note that Figure 5.6 only shows the selected micrographs of TN_01, TN_03 and TN_05 in the supported state. (The corresponding micrographs of TN_02 and TN_04 can be found in Appendix C). According to Fischer (2011), the darker crystallites or areas are more likely to contain Co_3O_4 crystallites and therefore, this is how the Co_3O_4 crystallites could potentially be distinguished from those of the γ-Al_2O_3 support. It can be seen that some areas of the γ-Al_2O_3 support contain single crystallites of Co_3O_4 but with some areas containing a cluster of Co_3O_4 crystallites even after the crystallites had been sonicated before depositing them onto the support. Due to the said poor contrast between the Co_3O_4 crystallites and those of the γ-Al_2O_3 support, valuable size information could not be obtained from these as counting a statistically significant number of crystallites (ca. 200 – 300) proved to be rather difficult. However, it should be noted that the average crystallite size of the unsupported crystallites in each sample was not expected to change due to the mild conditions used for supporting the crystallites (see sub-section 4.1.1) as it was also seen from the PXRD data.

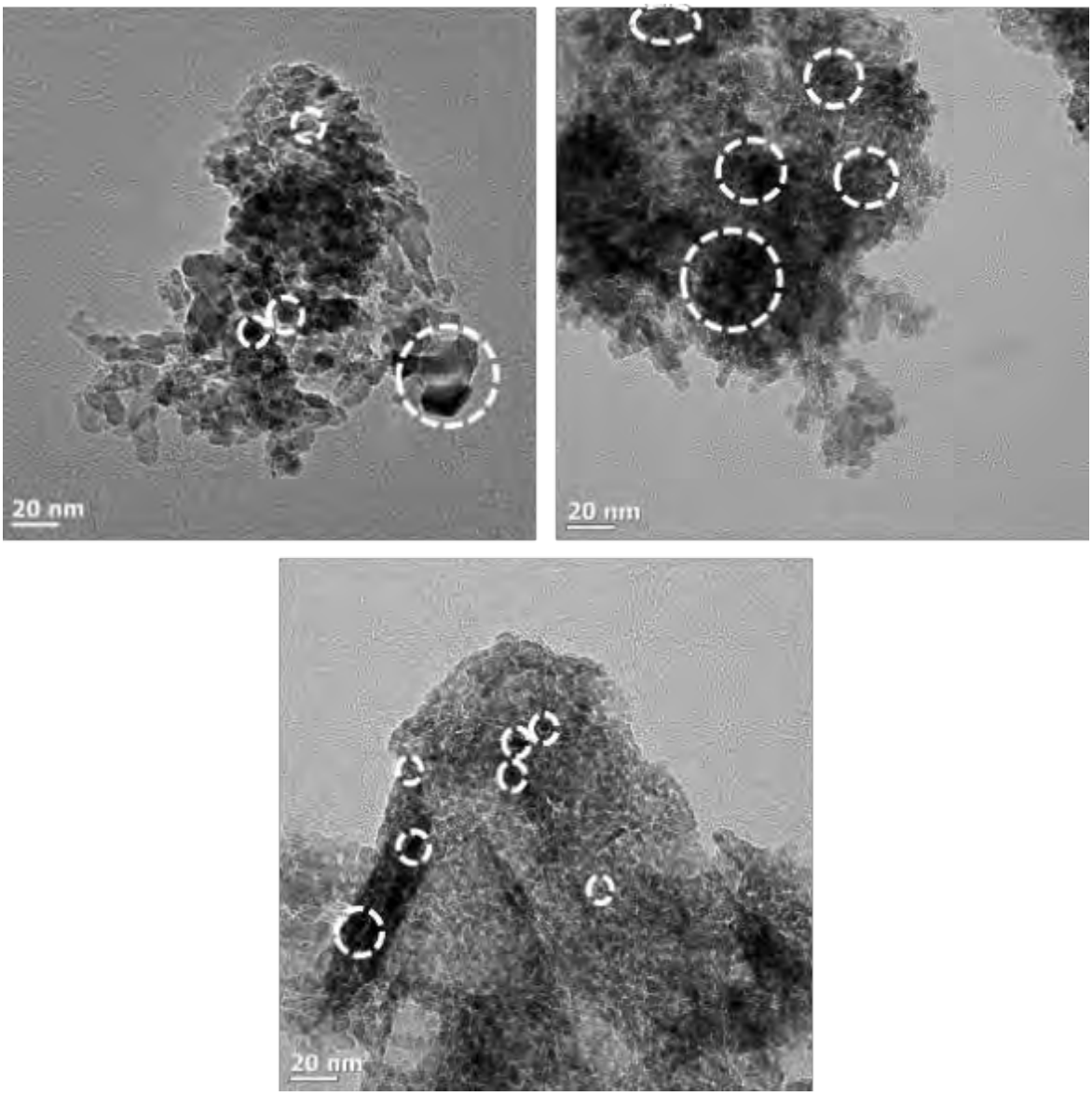

Figure 5.6: *TEM micrographs of the fresh samples of (**top-left**) TN_01, (**top-right**) TN_03 and (**bottom**) TN_05 in the supported state. Circled with white dashed lines are some of the single crystallites or a group of crystallites of* Co_3O_4 *identified.*

5.2.2. Alteration of the support-addition method

TEM analysis was also used to obtain average crystallite sizes and size distributions for the second series of catalysts *i.e.,* RM_1 – RM_4. Figure 5.7 shows the selected micrographs of the supported samples of RM_2 – RM_4. (Note: RM_1 is shown in Figure 5.6 as TN_05). From these single crystallites and some clusters of Co_3O_4 crystallites were identified as described above. The crystallites also appeared mostly spherical and when calculating the volume-based average crystallite size, this was taken into account. From the crystallites identified, a number-based size distribution for each sample was plotted and shown in Figure 5.8. It can be seen that the size distributions are narrow and also point towards similar average sizes between these four catalysts. Table 5.4 shows the number- and volume-based average crystallite size calculated for each catalyst and it can be seen that indeed all four catalysts had crystallites of similar sizes which were in the desired 3.0 – 5.0 nm range.

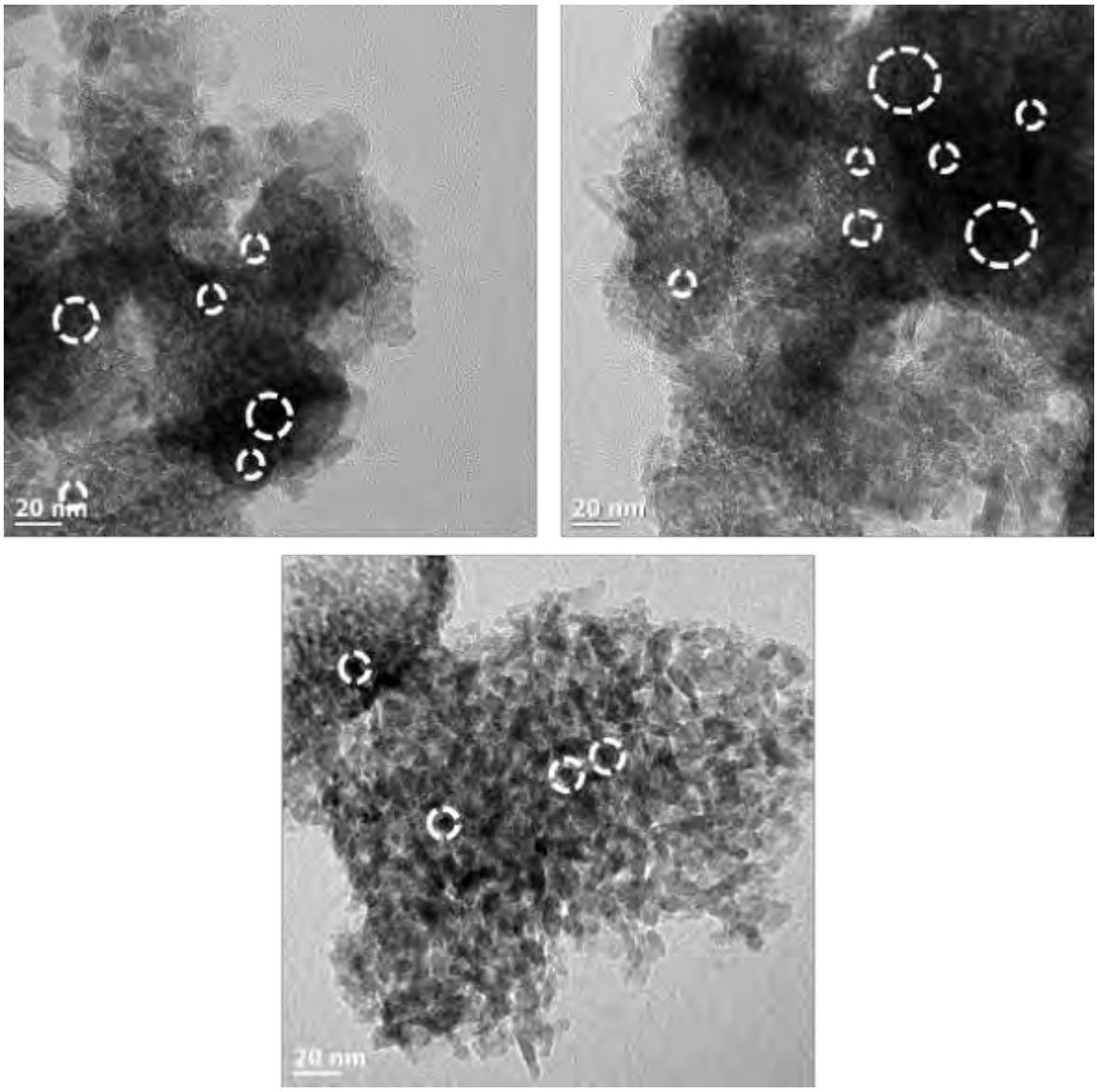

Figure 5.7: *TEM micrographs of the fresh samples of (**top-left**) RM_2, (**top-right**) RM_3 and (**bottom**) RM_4. Circled with white dashed lines are some of the single crystallites or a group of crystallites of* Co_3O_4 *identified.*

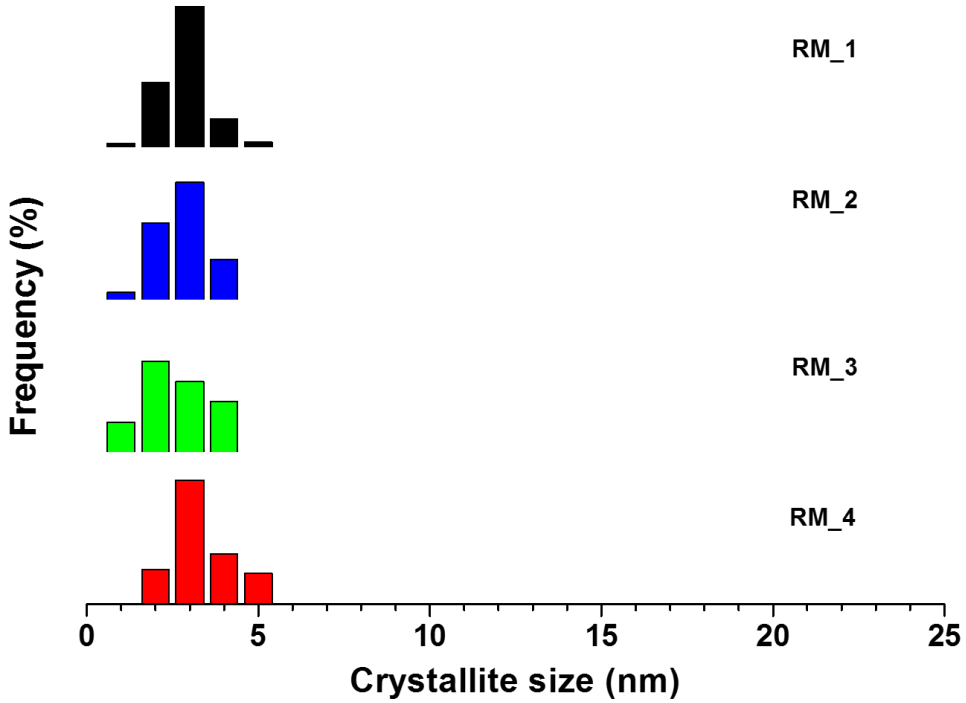

Figure 5.8: *Number-based size distributions of the fresh samples of RM_1 – RM_4 obtained by means of TEM analysis.*

Table 5.4: *Number- and volume-based crystallite sizes of the fresh samples of RM_1 – RM_4 obtained by TEM analysis.*

Sample Name	Targeted size (nm)	Actual size[a] (nm)	Actual size[b] (nm)
RM_1 (TN_05)	3.0 – 5.0	3.3 ± 0.6	3.7 ± 0.7
RM_2	3.0 – 5.0	3.3 ± 0.7	3.7 ± 0.8
RM_3	3.0 – 5.0	3.2 ± 0.8	3.9 ± 0.9
RM_4	3.0 – 5.0	3.8 ± 0.9	4.4 ± 1.0

[a] TEM number-based average crystallite sizes obtained using Equations 4.1 and 4.3

[b] TEM volume-based average crystallite sizes obtained using Equations 4.2 and 4.4

Table 5.5 shows compares the volume-based average crystallite sizes obtained from PXRD and TEM analysis for all catalysts *i.e.,* unsupported and supported samples of TN_01 – TN_05 and the supported samples of RM_2 – RM_4 (where possible). It can be seen that there is a very good agreement between the sizes obtained from these two techniques and more generally, that

the reverse micelle method was successful in controlling the final crystallite of the crystallites as desired.

Table 5.5: *Volume-based average crystallite sizes for TN_01 – TN_05 in the unsupported (PXRD and TEM) and supported state (PXRD), as well as for RM_2 – RM_4 in the supported state (PXRD and TEM).*

Sample Name	Targeted size (nm)	PXRD size: unsupported (nm)	PXRD size: supported (nm)	TEM size (nm)
TN_01	13.0 – 15.0	15.1	15.3	13.8
TN_02	10.0 – 12.0	9.9	10.2	9.5
TN_03	7.0 – 9.0	7.2	7.5	7.2
TN_04	4.0 – 6.0	5.3	5.1	4.5
TN_05/RM_1	3.0 – 5.0	4.3	4.5	3.7
RM_2	3.0 – 5.0	-	3.5	3.7
RM_3	3.0 – 5.0	-	3.8	3.9
RM_4	3.0 – 5.0	-	4.2	4.4

5.3. Energy-dispersive X-ray (EDX) spectroscopy

Elemental analysis by EDX spectroscopy allowed for the quantification of Co, Al and O. From this, one could then use the atomic ratios to calculate the amount of Co_3O_4 actually present in each sample. Table 5.6 shows the calculated Co_3O_4 loading of all eight synthesised catalysts. The Co_3O_4 loadings obtained using the TOPAS 4.1 software are also included for comparison. The results shown confirm that the targeted Co_3O_4 loading was obtained for the five samples of varying crystallite sizes *i.e.,* TN_01 – TN_05. For RM_2 – RM_4, the Co_3O_4 loading was lower than targeted loading in each case. Overall, it is worth mentioning that the EDX loading and the TOPAS-derived loading were in very good agreement.

RM_2 and RM_3 were synthesised by adding the support in the microemulsion to allow for the uptake of cobalt nitrate and cobalt hydroxide, respectively. When this was done, not all of the precursor material was taken up by the support. Upon addition of the NH_3 precipitating agent, a green precipitate (*i.e.,* $Co(OH)_2$) was formed and also recovered after the washing procedure together with the reddish-pink impregnated support. Attempting to deposit these unsupported $Co(OH)_2$ nanoparticles onto the already impregnated support would have resulted in the formation of cobalt oxide particles with different metal-support interactions in a single sample - which was not desired. Therefore, the unsupported $Co(OH)_2$ nanoparticles were separated from the impregnated support using a separating funnel as the impregnated support was denser than the $Co(OH)_2$ particles.

The synthesis of RM_4 relies on the assumption that all the cobalt nitrate gets converted to the green cobalt hydroxide precipitate upon addition of aqueous NH_3. Also, it is assumed that no particles are lost during the washing procedure and during their deposition onto the support prior to the drying and calcination steps. It may be possible that these assumptions did not hold true and the low cobalt oxide loading is in fact a result of the losses incurred during the synthesis.

Table 5.6: *Co_3O_4 loading in the synthesised catalysts obtained using EDX spectroscopy. In the brackets, next to each sample name, is the PXRD average crystallite size of Co_3O_4.*

Sample Name	Targeted loading (wt.-%)	EDX loading (wt.-%)	TOPAS loading (wt.-%)
TN_01 (15.3 nm)	10.0	10.9	9.1
TN_02 (10.2 nm)	10.0	8.8	9.9
TN_03 (7.5 nm)	10.0	9.2	8.9
TN_04 (5.1 nm)	10.0	8.5	8.9
TN_05/RM_1 (4.5 nm)	10.0	9.4	8.7
RM_2 (3.5 nm)	10.0	5.8	6.2
RM_3 (3.8 nm)	10.0	5.9	5.8
RM_4 (4.2 nm)	10.0	5.2	4.3

5.4. Hydrogen temperature-programmed reduction (H_2-TPR)

5.4.1. Variation of the crystallite size of Co_3O_4

Temperature-programmed reduction using hydrogen (H_2-TPR) was conducted to determine the reducibility of Co_3O_4 nanoparticles. This was done over a temperature range starting from 60 °C going up to 920 °C. The hydrogen consumption was measured using a thermal conductivity detector attached to the H_2-TPR instrument used. The reduction of Co_3O_4 to Co is generally believed to occur over two steps as shown by Equations 5.1 and 5.2. This implies that the TPR profile of Co_3O_4 would mainly display two reduction peaks (Sewell *et al*., 1996; Tang *et al.*, 2008). However in other literature, the TPR profiles of Co_3O_4 have been shown to possess only one reduction peak which involves the reduction of Co_3O_4 to Co as shown by Equation 5.3 (Arnoldy & Moulijn, 1985; Sirijaruphan *et al.*, 2003). In the presence of strong metal-support

interactions, three or four reduction peaks have been observed in some TPR profiles of supported Co_3O_4 catalysts.

$$\boldsymbol{Co_3O_4(s) + H_2(g) \rightarrow 3CoO(s) + H_2O(g)} \qquad \textbf{Equation 5.1}$$

$$\boldsymbol{CoO(s) + H_2(g) \rightarrow Co(s) + H_2O(g)} \qquad \textbf{Equation 5.2}$$

$$\boldsymbol{Co_3O_4(s) + 4H_2(g) \rightarrow 3Co(s) + 4H_2O(g)} \qquad \textbf{Equation 5.3}$$

In this part of the study, the desired outcome was to synthesise supported Co_3O_4 crystallites of different sizes which will have minimal interaction with the support (Fischer *et al*., 2011). Therefore, a maximum of two reduction peaks was expected for these supported catalysts. Also, the reducibility of the Co_3O_4 phase was predicted to be inversely proportional to the crystallite size *i.e.,* smaller crystallites being easily reduced compared to larger crystallites (Fischer *et al.*, 2014; Liu *et al.*, 2013; Wang *et al.*, 2005). Figure 5.9 shows the TPR profiles of the five catalysts synthesised. It can be seen that TN_01 and TN_02 mainly display one reduction peak, with TN_01 having a small shoulder on the left of the main reduction peak. The reduction of the crystallites in TN_01 and TN_02 occurs over a relatively narrower temperature range of 200 – 350 °C. The other three catalysts displayed two (TN_03) and three (TN_04 and TN_05) reduction peaks. The reduction process for these three catalysts took place over a wider temperature range of 180 – 480 °C. This implied that the small-sized crystallites of Co_3O_4 in these three catalysts were harder to reduce compared to the larger crystallites in TN_01 and TN_02. This result was not expected as previous studies have revealed an opposite trend (Fischer *et al.*, 2014; Liu *et al.*, 2013; Wang *et al.*, 2005).

The γ-Al_2O_3 support for supporting the Co_3O_4 nanoparticles has an average pore diameter of 11.5 nm. Therefore, it is possible that some of the small crystallites in TN_03, TN_04 and TN_05 enter the pores of the support and interact relatively stronger with the support making them harder to reduce. This strong interaction may also explain the appearance of three peaks instead of two in TN_04 and TN_05 (Fischer, 2011).

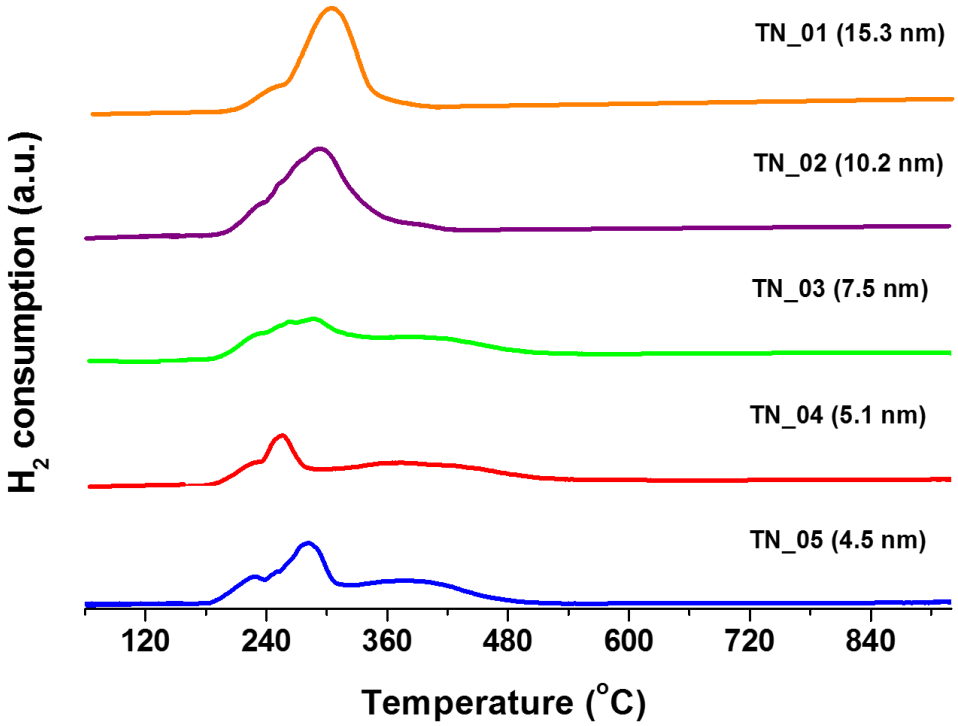

Figure 5.9: *H_2-TPR profiles for the five catalysts with varying crystallite size of Co_3O_4. In the brackets, next to each sample name, is the PXRD average crystallite size of Co_3O_4.*

5.4.2. Alteration of the support-addition method

H_2-TPR experiments were also conducted on the catalysts RM_1, RM_2, RM_3 and RM_4. When synthesising these catalysts, the aim was to alter the strength of the metal-support interactions, therefore, the success of this procedure can be assessed with H_2-TPR (Arnoldy & Moulijn, 1985; Fischer *et al.*, 2012). Strong metal-support interactions decrease the reducibility of the metal oxide species *i.e.,* the metal oxide is instead reduced at relatively higher temperatures. This behaviour may also affect the catalytic performance of supported metal oxides especially in oxidation reactions (Wang *et al.*, 2006; Zhao *et al*., 2008). Figure 5.10 shows the H_2-TPR profiles of the four above-mentioned catalysts. The Co_3O_4 crystallites in RM_1 and RM_4 completely reduce at relatively lower temperatures and display three reduction peaks. However, the crystallites in RM_2 and RM_3 display two reduction peaks in the 180 - 330 °C temperature range and a separate peak above 800 °C. The catalyst RM_4 reduces over a narrower temperature range than that observed for RM_1 which may imply that the metal-support interactions in RM_4 are weaker than those in RM_1.

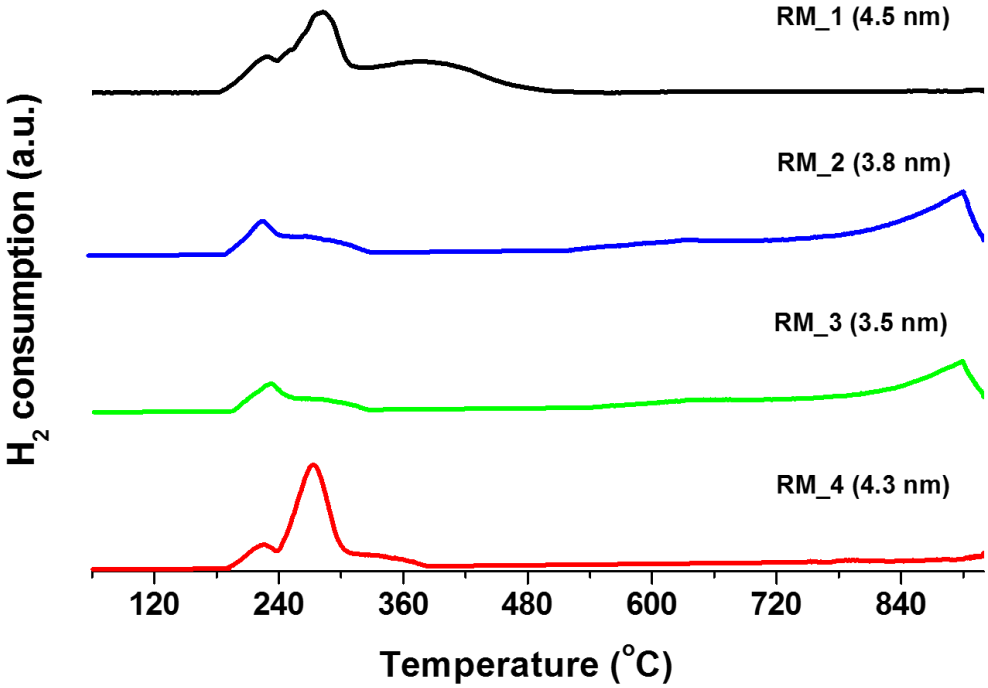

Figure 5.10: *H_2-TPR profiles for the four catalysts with different metal-support interactions. In the brackets, next to each sample name, is the PXRD average crystallite size of Co_3O_4.*

Fischer *et al.* (2012) also observed a similar behaviour when comparing these two catalysts. According to Fischer *et al.*, it may be possible that there was still some residual surfactant around the green $Co(OH)_2$ nanoparticles used for synthesising RM_4 which may have hindered them from entering the pores of the support prior to the drying and calcination steps. The Co_3O_4 nanoparticles used for synthesising RM_1 were obtained after drying and subsequent calcination leaving the surface of these nanoparticles with a negligible amount of surfactant. This allowed for their easy entry into the pores of the support, hence inducing slightly stronger metal-support interactions in RM_1. Figure 5.11 simply illustrates this point.

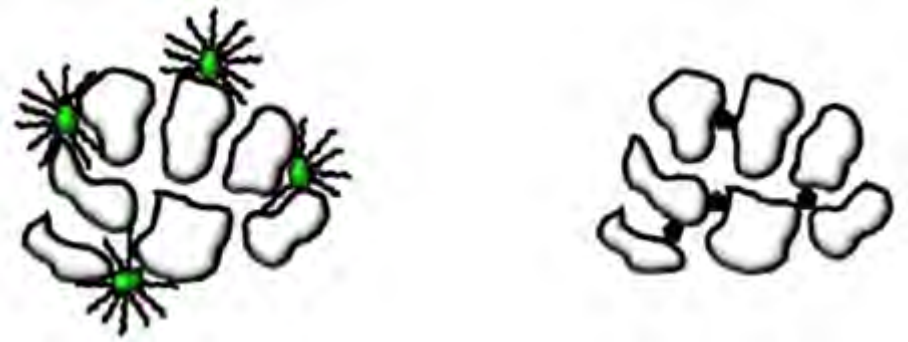

Figure 5.11: *(**left**) Residual surfactant hindering the entry of $Co(OH)_2$ particles into the pore system of γ-Al_2O_3 when synthesising RM_4. (**right**) Co_3O_4 particles residing in the pores of the γ-Al_2O_3 and thus interacting strongly with the support. [From Fischer (2011)].*

Catalysts RM_2 and RM_3 displayed a different reduction behaviour to RM_1 and RM_4. Between 180 and 330 °C, two reduction peaks were observed and later another reduction peak emerged above 800 °C. In the literature, this reduction behaviour has been reported for some Al_2O_3-supported Co_3O_4 catalysts (Arnoldy & Moulijn, 1985; Fischer *et al.*, 2012; Sirijaruphan *et al.*, 2003; Wang *et al.*, 2006). The two low-temperature peaks were assigned to the normal reduction of Co_3O_4 to Co. The high-temperature reduction peak above 800 °C was assigned to the possible reduction of cobalt aluminate-like ($CoAl_2O_4$) species. RM_2 and RM_3 were synthesised by contacting the support with the dissolved metal precursor and later performing a high-temperature (*i.e.,* 400 °C) calcination. This procedure could have caused for some Co^{2+} ions of the precursor to migrate into the support matrix to form these irreducible cobalt aluminates (Arnoldy & Moulijn, 1985; Fischer *et al.*, 2012; Sirijaruphan *et al.*, 2003; Wang *et al.*, 2006). Sirijaruphan *et al.* (2003) further postulated that these species may also be just formed during the TPR experiment. As the temperatures are increased, the Co^{3+} ions of Co_3O_4 are reduced to Co^{2+} ions and some of these Co^{2+} ions could migrate into the support matrix resulting in the formation of the said cobalt aluminates. Some or all of the aforementioned ideas could explain the formation of these very strong metal-support interactions in the form of cobalt aluminates.

5.5. Summary: Catalyst preparation and *ex situ* characterisation

The reverse micelle technique was successfully employed to obtain the first series of catalysts (*i.e.,* TN_01 – TN_05) with varying crystallite sizes of Co_3O_4 within the 3.0 – 15.0 nm range. This was achieved by altering the oil-to-surfactant ratio, water-to-surfactant ratio (ω) and the starting amount/mass of the $Co(NO_3)_2.6H_2O$ precursor. The deposition of Co_3O_4 in the calcined state onto the γ-Al_2O_3 support was performed in order to minimise the contact/interaction between the support and the nanoparticles (Fischer *et al.*, 2012). Therefore, this procedure conveniently allowed for the investigation of the effect of crystallite size without having to be concerned about the effect of (significant) metal-support interactions. The second series of catalysts (*i.e.,* RM_1 – RM-4) were also synthesised using the reverse micelle technique. However, the support was contacted with the cobalt-containing species at different stages of the synthesis in each case. This was done in order to inflict different metal-support interactions in the prepared catalysts. The Co_3O_4 crystallite size in these four catalyst samples was kept within the 3.0 – 5.0 nm size range so to minimise the effect of having different crystallite sizes during the catalytic performance tests.

PXRD and TEM analyses were both successful in confirming the targeted crystallites sizes of Co_3O_4 in the unsupported and supported catalysts. TEM analysis was particularly useful in obtaining crystallite size distributions which in turn gave an indication on the success of the reverse micelle method in controlling the Co_3O_4 crystallite size. Also, a number- and volume-based average size was obtained as well for each catalyst. The TEM volume-based sizes were in good agreement with the volume-based sizes obtained by Rietveld refinement. With EDX analysis, it was possible to confirm the elemental composition of each sample and from the analysis, the Co_3O_4 loading was calculated. The Co_3O_4 loading obtained using EDX was found to be in good agreement with the loading determined using Rietveld refinement and PONCKS on Topas 4.1.

Finally, H_2-TPR experiments offered valuable insight into the reducibility of the supported catalysts synthesised. It was observed that catalysts with larger crystallites (TN_01 and TN_02) where easier to reduce than the catalysts with smaller crystallites. This behaviour was attributed to the possible existence of slightly stronger metal-support interactions in the catalysts with smaller crystallites (Fischer, 2011). For the samples RM_1 – RM_4, H_2-TPR experiments clearly confirmed the existence of metal-support interactions of varying strengths between the

samples. RM_1 and RM_4 were much easier to reduce due to the presence of relatively weaker interactions (Fischer *et al.*, 2012). Whereas RM_2 and RM_3 exhibited very strong metal-support interactions which was indicated by a reduction peak above 800 °C which was attributed to the presence of cobalt aluminates (Arnoldy & Moulijn, 1985; Fischer *et al.*, 2012; Sirijaruphan *et al.*, 2003; Wang *et al.*, 2006).

Chapter 6: Catalyst Testing & *In situ* Characterisation Results

6.1. Catalyst testing

Catalytic tests were performed in fixed bed reactors and the tests were directly coupled with *in situ* characterisation in the magnetometer and PXRD capillary cell instruments, respectively. The amount of catalyst loaded in the *in situ* magnetometer reactor was varied between 1.0 and 1.2 g to account for the differences in the Co_3O_4 loading and a total gas flow rate of 100 ml (NTP)/min was used for the experiments done with catalysts TN_01 – TN_05. For the experiments with RM_2 – RM_4, the amount of catalyst loaded was varied between 1.3 and 1.5 g and a total gas flow rate of 78 ml (NTP)/min was used. The feed comprised of a 1:1:52:46 $CO/O_2/H_2/N_2$ gas mixture where the gases CO, H_2 and N_2 were introduced from one cylinder (AFROX (0.97% CO, 44.60% N_2 in H_2)) and O_2 was co-fed as synthetic air from a different gas cylinder (Air products (21% O_2 in N_2, 99.999 % purity)).

In the *in situ* PXRD capillary reactor, the mass of catalyst loaded was 15 mg and to maintain the same space velocity between the two instruments, the total flow rate was varied between 1.3 and 1.6 ml (NTP)/min of the same gas mixture used for the *in situ* magnetic studies. The temperature was varied between 50 and 350 °C at atmospheric pressure, which involved heating and cooling profiles. Temperature changes were of 25 °C steps with a 1 °C/min ramp and the temperature being held for an hour at every 25 °C in both instruments. The reactor outlet gases were analysed using a GC-TCD instrument which enabled the determination of the total CO conversion, CO_2 yield and selectivity from O_2 and CH_4 yield.

6.1.1. Effect of Co_3O_4 crystallite size

After confirming that five catalysts with Co_3O_4 crystallites of varying sizes and most importantly, with reasonably narrow size distributions, this allowed the possibility to investigate the effect of crystallite size on the CO-PROX catalytic performance of these five catalysts. Figure 6.1 shows the normalised reactor outlet flow rates of CO, CO_2 and CH_4 calculated from the data obtained during the *in situ* magnetic studies. These normalised flow rates are for three of the five prepared catalysts *i.e.,* TN_01 (15.3 nm), TN_03 (7.5 nm) and TN_05 (4.5 nm). Kinetic data for TN_02 and TN_04 appears in Appendix D. The absolute outlet flow rates calculated were an average of two data points at every temperature *i.e.,* one at t = 30 minutes and one at t = 55 minutes. It is worth mentioning that the conversions at each held temperature were very similar and therefore, an average of two data points was a good representation of the overall conversion at that temperature. The normalised outlet flow rate of each gas at every 25 °C are shown along the heating profile (*i.e.,* 50 - 350 °C) and cooling profile (*i.e.,* 350 - 50 °C), respectively. According to Equations 2.1 and 2.4, one mole of CO is required to form one mole of CO_2. Similarly, one mole of CO is required to form one mole of methane. Therefore, normalising the outlet flows of these gases makes it possible to obtain the total CO conversion as well as the CO_2 and CH_4 yield, respectively. Furthermore, the CO_2 selectivity from the conversion of CO can also be directly obtained from the plots in Figure 6.1.

Over all three catalysts, the temperature range in which CO is only converted to CO_2 is 75 - 225 °C with no methane being formed. However, the mass-specific CO oxidation activity appeared to be dependent on the starting crystallite size of Co_3O_4. TN_05 (4.5 nm) generally showed higher CO conversions at every temperature between 75 and 225 °C and TN_01 (15.3 nm) showed relatively lower conversions among the three catalysts. Also, the temperature at which 50% of the CO was converted to CO_2 (*i.e.,* T_{50}) decreased with decreasing the starting crystallite size, which indicates a greater mass-specific activity over smaller crystallites. TN_01 had a T_{50} in the 175 – 200 °C temperature range, TN_03 had a T_{50} slightly above 150 °C and TN_05 had T_{50} in the 125 – 150 °C temperature range. The temperature at which the maximum amount of CO_2 was formed (*i.e.,* $T_{CO_2\ max}$) over each catalyst also decreased with the starting crystallite size of Co_3O_4. TN_01 had a $T_{CO_2,max}$ of 225 °C (with the CO_2 max. = 83%), TN_03 had a $T_{CO_2\ max}$ of 200 °C (CO_2 max. = 96%) and finally, TN_05 had a $T_{CO_2\ max}$ of 175 °C (CO_2 max. = 98%). The 98% CO conversion to CO_2 of TN_05 implies that there is still 20000 ppm

of CO present in the H_2-rich gas exiting the reactor at 175 °C, which is well above the 10 ppm limit stipulated for fuel cell applications.

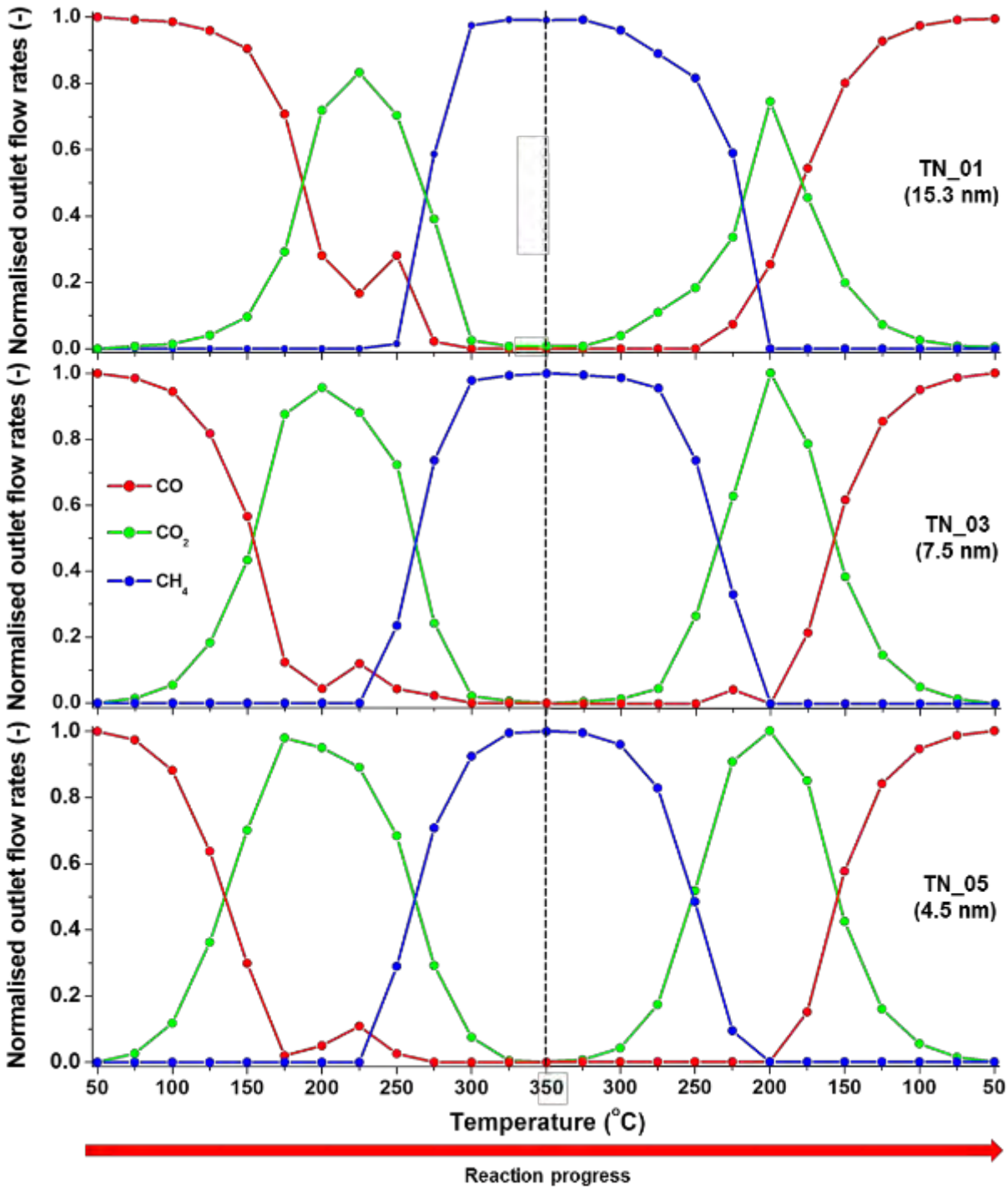

Figure 6.1: *Normalised outlet flow rates of CO, CO_2 & CH_4 as a function of temperature for (**top**) TN_01, (**middle**) TN_03 and (**bottom**) TN_05. In the brackets, next to each sample name, is the starting PXRD average crystallite size of Co_3O_4.*

Nonetheless, above these $T_{CO_2\ max}$ temperatures, the CO_2 formation decreased and the CO levels consequently began to increase. This was due to the H_2 oxidation reaction starting to dominate over CO oxidation as being the most favoured reaction at these high temperatures (Woods *et al.*, 2010; Yung *et al.*, 2008). The CO levels reached a maximum over the 225 – 250 °C temperature range before methane formation was observed. The methane light-off temperature was 250 °C over each catalyst, however very little CH_4 was formed over TN_01 at this temperature. Methane formation is known to take place over reduced metallic cobalt catalysts and so the formation of methane in this regard was attributed to the reduction of the cobalt oxide phase (Herranz *et al.*, 2009; Tuxen *et al.*, 2013; Teng *et al.*, 1999). As high reaction temperatures were reached, methanation completely dominated over the CO oxidation reaction and 100% conversion of the CO was achieved above 300 °C over all three catalysts.

Upon decreasing the reaction temperature to below 325 °C, the catalysts slowly re-gained CO oxidation activity. CO_2 formation was still higher at every temperature along the cooling profile over TN_05 compared to the other catalysts. It was clear that the catalysts had lost some of their initial activity as the CO_2 yields over each catalyst had decreased at every corresponding temperature along the cooling profile. This observation strongly indicated that the all three catalysts had undergone some structural (*i.e.,* crystallite size) and/or chemical transformations (*i.e.,* phase changes) during the experimental run.

As already mentioned, the formation of methane points towards partial or complete reduction of Co_3O_4 to Co. However, the formation of CO_2 upon decreasing the reaction temperature suggested that the metallic cobalt species formed could have been partially re-oxidised. The re-oxidation of Co to CoO under similar conditions, *i.e.,* temperature and O_2 partial pressure, has been previously observed resulting in core-shell structured crystallites (Sadasivan *et al*., 2013). The formation of a CoO shell (and a metallic cobalt core) could be the reason for the restored CO oxidation activity over each catalyst. CoO, just like Co_3O_4, has been shown to exhibit good CO oxidation activity in the absence and presence of H_2 (Ko *et al.*, 2006; Mankidy *et al.*, 2014; Teng *et al.*, 1999). Below 200 °C, methane formation was no longer observed and this could be a result of a complete re-oxidation of the surface metallic cobalt species.

To oxidise the CO, O_2 was co-fed using a 1:1 CO/O_2 gas volumetric ratio. The oxygen being co-fed potentially had a second reaction pathway which it could take *i.e.,* the oxidation of H_2, which in turn has a major effect on the CO_2 selectivity (Brown Jr. *et al.*, 1960; Mishra & Prasad; 2011). Shown in Figure 6.2 is the CO_2 selectivity based on the conversion of O_2 ($\boldsymbol{S_{CO_2}^{O_2}}$) as a

function of temperature for TN_01, TN_03 and TN_05 (see Appendix D for the $S_{CO_2}^{O_2}$ of TN_02 and TN_04). As already mentioned in sub-section 4.3.3, the H_2O selectivity from O_2 ($S_{H_2O}^{O_2}$) can be expected to be $\mathbf{100} - S_{CO_2}^{O_2}$. As expected, when the temperature was increased, the CO_2 selectivity decreased. Below 175 °C, TN_05 exhibited high CO_2 selectivities compared to the other two catalysts which is consistent with the data presented in Figure 6.1. At and above 175 °C, TN_05 drastically lost its CO_2 selectivity with the other two catalysts undergoing a less severe decrease in this regard. Above 225 °C, there was no clear dependency of the CO_2 selectivity on the starting crystallite size of Co_3O_4 observed. Also at these high temperatures, the decrease in the CO_2 selectivity was greater as a result of methanation which further decreases the conversion of CO to CO_2.

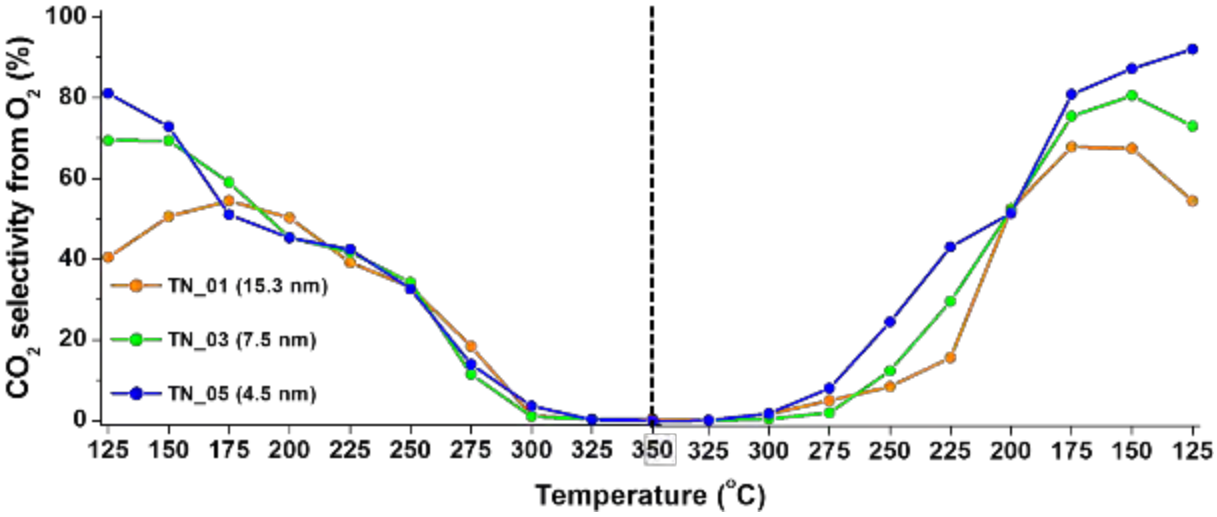

Figure 6.2: *CO_2 selectivity based on the conversion of O_2 as a function of temperature for the catalysts TN_01, TN_03 and TN_05.*

Upon decreasing the reaction temperature, the CO_2 selectivity increased below 325 °C. Again, this confirmed the establishment of CO oxidation active sites possibly through the re-oxidation of metallic cobalt. The increase in the CO_2 selectivity along the cooling profile shows a dependency on the starting crystallite size of Co_3O_4 *i.e.,* TN_05 maintained higher selectivities compared to the other two catalysts.

As observed in Figure 6.1, TN_05 displayed superior overall mass-specific CO oxidation activity and particularly, this catalyst had the lowest $T_{max,CO2}$ of 175 °C. The stability of this

catalyst was therefore, tested at this temperature through performing a time-on-stream experiment over a 36-hour period using the same gas mixture and gas flow as in the temperature sweep experiments (*i.e.,* 50 to 350 °C and back to 50 °C). Shown in Figure 6.3 is the total CO conversion and CO_2 selectivity from O_2 calculated over the 36-hour period. The catalyst was able to reach full CO conversion to CO_2 after two hours and was also able to maintain a stable total CO conversion of 100% and CO_2 selectivity from O_2 of 53% (and a 47% H_2O selectivity from O_2) throughout the whole experiment. There were no traces of methane during the course of the experiment and this observation alone confirmed that no reduction to metallic cobalt took place. An *ex situ* PXRD analysis of the spent sample obtained at the end of the experiment further confirmed that the catalyst remained as Co_3O_4 without reducing to CoO or Co. The spectrum obtained from the said analysis can be found in Appendix H.

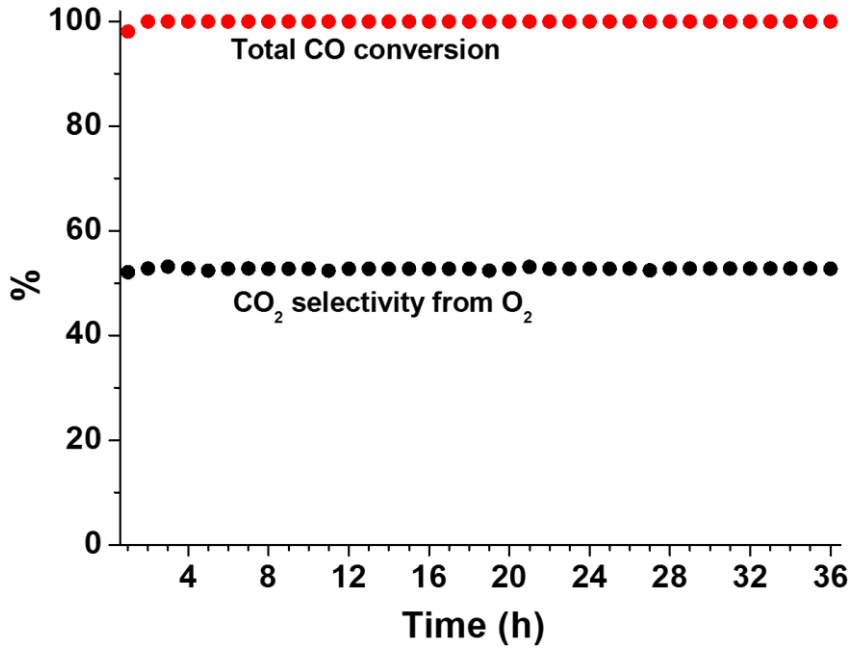

Figure 6.3: *CO conversion and CO_2 selectivity as a function of time for TN_05 at 175 °C.*

6.1.2. Effect of metal-support interactions

The four catalysts, RM_1 (4.5 nm), RM_2 (3.5 nm), RM_3 (3.8 nm) and RM_4 (4.2 nm), were also tested for CO-PROX activity. H_2-TPR experiments conducted on these catalysts confirmed that different metal-support interactions were induced when the support-addition method for producing these catalysts was altered. RM_2 and RM_3 displayed a very similar reduction behaviour and furthermore, the crystallites in these catalysts were much harder to reduce compared to those in RM_1 and RM_4. This was attributed to the presence of very strong metal-support interactions (Arnoldy & Moulijn, 1985; Fischer *et al.*, 2012; Sirijaruphan *et al.*, 2003; Wang *et al.*, 2006). Therefore, in testing these four catalysts, the goals were to investigate the effect of metal-support interactions on their catalytic performance and reducibility under the H_2-rich environment of CO-PROX.

Figure 6.4 shows the normalised outlet flow rates of CO, CO_2 and CH_4 along the heating and cooling profiles, respectively for all four catalysts. These normalised flow rates were also calculated from the data obtained during the *in situ* magnetic studies. From the plots in this figure, it is clear that the CO oxidation light-off temperatures over RM_1 and RM_4 were lower than those for RM_2 and RM_3. The former two catalysts began to oxidise CO at 75 °C whilst the latter two began at temperatures in the 100 – 125 °C range. RM_1 and RM_4 also had low T_{50} values which were between 125 and 150 °C, whereas RM_2 had a T_{50} just above above 200 °C and RM_3 had a T_{50} value just below 200 °C. The $T_{CO_2\ max}$ for RM_1 was 175 °C with a CO_2 max. of 98% whereas RM_4 obtained 100% CO conversion at 175 and 200 °C. Both RM_2 and RM_3 obtained a $T_{CO_2\ max}$ of 225 °C but the CO_2 max. for RM_2 was 76% and for RM_3 was 86%. It is clear that RM_4 was able to reduce the CO levels in the H_2-rich gas feed to below 10 ppm.

However, between 200 and 225 °C RM_4 began to form methane and RM_1 shortly followed in the 225 – 250 °C temperature range. Methane formation over RM_2 and RM_3 was not observed until temperatures between 275 and 300 °C in the case of RM_2; 250 – 275 °C in the case of RM_3. This implied that RM_3 was slightly easier to reduce compared to RM_2 and that both RM_1 and RM_4 were much easier to reduce compared to RM_2 and RM_3. This overall trend could also explain the differences in the CO oxidation and methanation activity between the four catalysts. The catalysts which were easier to reduce showed higher CO oxidation and methanation activity than those that were harder to reduce.

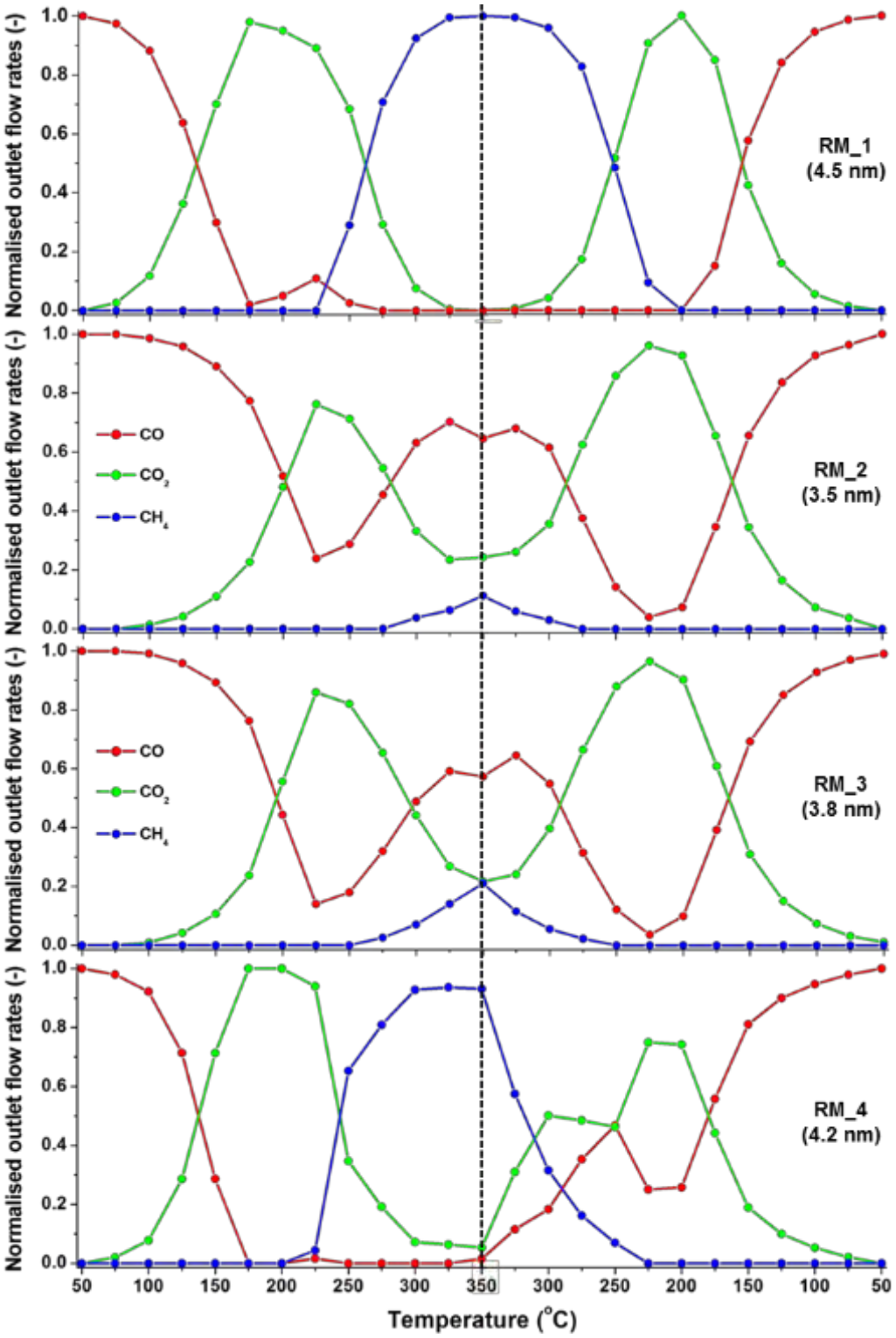

Figure 6.4: *Normalised outlet flow rates of CO, CO_2 & CH_4 as a function of temperature for RM_1 - RM_4.*

Upon cooling the reactor, the CO_2 yields over each catalyst increased as observed in the case of the first series of catalysts discussed earlier. RM_1 and RM_4 had clearly lost some of their previous activity with RM_4 appearing to have suffered a greater loss than RM_1. This could be a result of sintering and/or phase changes in the catalyst. However, RM_2 and RM_3 display an unexpected behaviour in that, they began to show enhanced CO oxidation activity compared to the activity displayed along the heating profile. It should still be noted that RM_1 maintained relatively higher CO_2 yields below 250 °C.

The CO_2 selectivities of these four catalysts were also determined and are shown in Figure 6.5. As expected, increasing the reaction temperature decreased the CO_2 selectivity as a result of H_2 oxidation beginning to dominate over the CO oxidation reaction. Below 175 °C, RM_1 and RM_4 show higher CO_2 selectivities than RM_2 and RM_3 but above 175 °C, this trend was reversed. This observation was in good agreement with the CO oxidation activity trends observed in Figure 6.5 along the heating profile. RM_2 and RM_3 continued to maintain their higher selectivities up to 350 °C. Upon cooling the reactor, the CO_2 selectivities for each catalyst increased which implied that CO oxidation activity over each catalyst was re-gained. Below 300 °C, RM_1 and RM_4 generally showed relatively lower selectivities than RM_2 and RM_3.

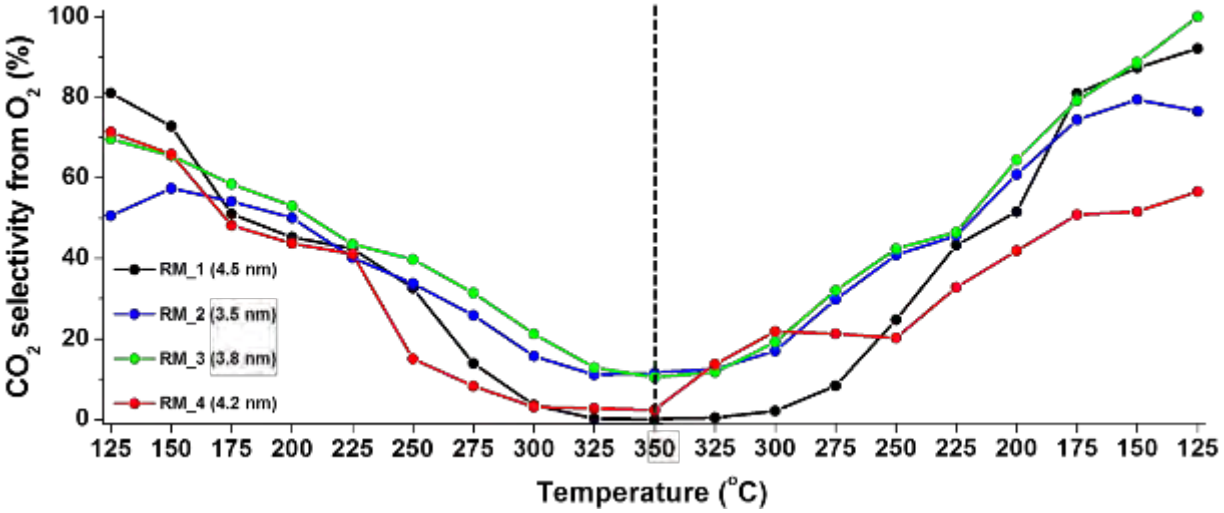

Figure 6.5: *CO_2 selectivity based on the conversion of O_2 as a function of temperature for all four catalysts.*

6.2. *In situ* magnetic studies in the magnetometer

As previously mentioned in section 4.3 above, magnetic studies on the synthesised catalysts were performed under CO-PROX reaction conditions. Since Co_3O_4-based catalysts were investigated in this study and also that the CO-PROX feed normally has high H_2 concentrations, the reduction of Co_3O_4 to CoO and Co can be expected at high temperatures (Teng *et al.*, 1999; Woods *et al.*, 2010). In the novel UCT-developed magnetometer instrument, only metallic cobalt can be detected since it is the only innately ferromagnetic cobalt phase among the three already mentioned above (Claeys *et al.*, 2010; Fischer *et al.*, 2014). For the studies in the magnetometer, sample magnetisation measurements were taken every 10 minutes from 50 to 350 °C and back to 50 °C each time at -2, 0, 2 T and again at 0 T. From a previously performed calibration of the instrument with a pure metallic cobalt sample of known mass, the sample magnetisations measured in this study and also from the EDX catalyst loading results, it was possible to calculate the degree of reduction of Co_3O_4. The degree of reduction is defined as the ratio of metallic cobalt formed/detected to the amount of cobalt loaded in the catalyst as Co_3O_4. At 50 °C after a test was completed, a single hysteresis measurement was taken by varying the magnetic field from -2 to 2 T and back to -2 T. This single measurement was performed in order to determine the amount of magnetic material displaying remnant magnetisation at 0 T (γ) in each sample and if possible, to also obtain a crystallite size distribution.

6.2.1. Effect of Co_3O_4 crystallite size

The aim in this part of the study was to investigate the effect of crystallite size on the reducibility of Co_3O_4. The results from the catalytic tests have already shown that over these catalysts, methane formation takes place at temperatures above 200 °C. The formation of methane is known to occur over metallic cobalt catalysts and so the observation made during the catalytic tests suggest that the Co_3O_4 phase has reduced to Co. Figure 6.6 shows the measured sample magnetisation at 2 T as a function of temperature for all five catalysts. The figure also shows the calculated degree of reduction from the measured magnetisations. The onset of reduction to Co in TN_02 seems to have occurred earlier (*i.e.,* at 225 °C) than in the other four catalysts (where it occurred at 250 °C). As the temperatures were increased above 250 °C, the

magnetisation and degree of reduction of each catalyst sample increased. However, TN_01 and TN_02 (having large crystallites) suddenly showed relatively higher degrees of reduction above 300 °C. This suggested that the larger crystallites were much easier to reduce than the smaller ones.

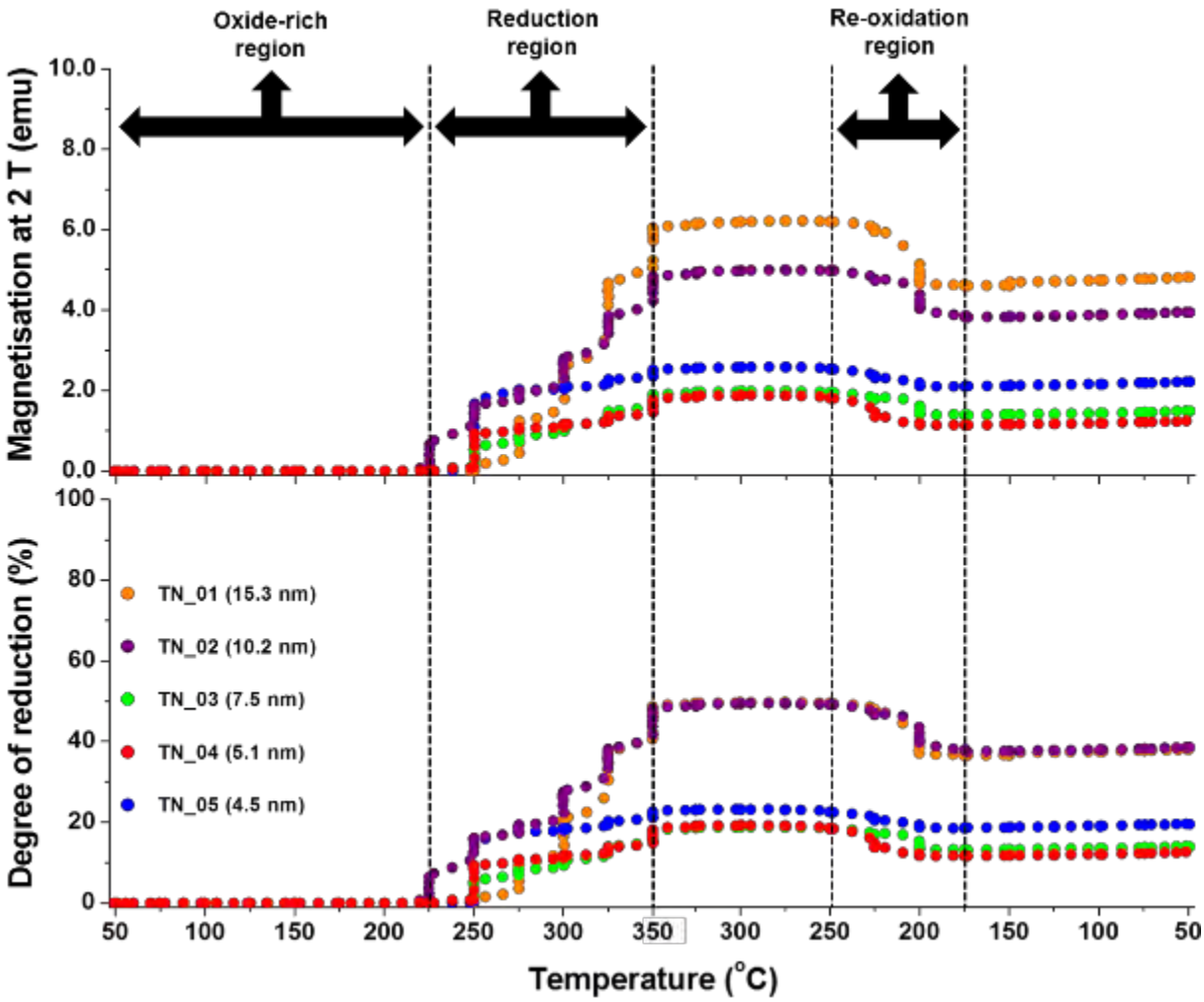

Figure 6.6: *(**top**) Sample magnetisation and (**bottom**) degree of reduction as a function of temperature for TN_01 - TN_05.*

This also appeared to be in close agreement with the H_2-TPR results obtained for these five catalysts (see Figure 5.9) which showed that the complete reduction of Co_3O_4 to Co was achieved over a relatively narrow temperature range in TN_01 and TN_02 as compared with the other three catalysts. This reduction behaviour of TN_01 and TN_02 during the magnetic studies can again be attributed to the slightly weak metal-support interactions that exist in these

catalysts. It should be noted that even with the high degrees of reduction observed for TN_01 and TN_02, the complete reduction of Co_3O_4 to Co was not observed.

Upon cooling the reactor, the degree of reduction and consequently, the magnetisation of each catalyst began to decrease below 250 °C. This decrease was attributed to the re-oxidation of the metallic cobalt to an oxide phase, possibly CoO (Sadasivan *et al*., 2013). However, this re-oxidation was terminated at 200 °C except in TN_02 where the re-oxidation ended at 175 °C. Similarly, the re-oxidation did not result in the complete loss of the metallic cobalt phase previously formed and therefore, this suggested that the crystallites after completion of the tests, may possess a double-shell structure. This proposed double-shell structure shown in Figure 6.7 has an oxide core (possibly CoO), a metallic cobalt inner-shell and a CoO outer-shell.

Figure 6.7: *A nanoparticle having a double shell-like structure after each test run. The nanoparticle is thought to have a (**grey**) CoO core, (**black**) a metallic cobalt inner-shell and (**grey**) a CoO outer-shell.*

As already shown in Figure 6.6, the catalyst TN_02 showed a reduction onset temperature of 225 °C with the other catalysts reducing at 250 °C. The onset of reduction to Co could be directly correlated with the formation of methane as shown in Figure 6.8. TN_02 was the first to form methane between 200 and 225 °C along the heating profile and was the only catalyst which showed some methanation activity even between 175 and 200 °C along the cooling profile. The formation and subsequent loss of the metallic cobalt phase was also, to some extent, correlated with the loss and restoration of the CO oxidation activity, respectively. Below 200 °C along the heating profile, this was seen as the oxide-rich region where Co_3O_4 and CoO were present. Also in the oxide-rich region, the conversion of CO is only towards the formation of CO_2. Above 200 °C was the reduction region where metallic cobalt was formed and consequently, methane as well.

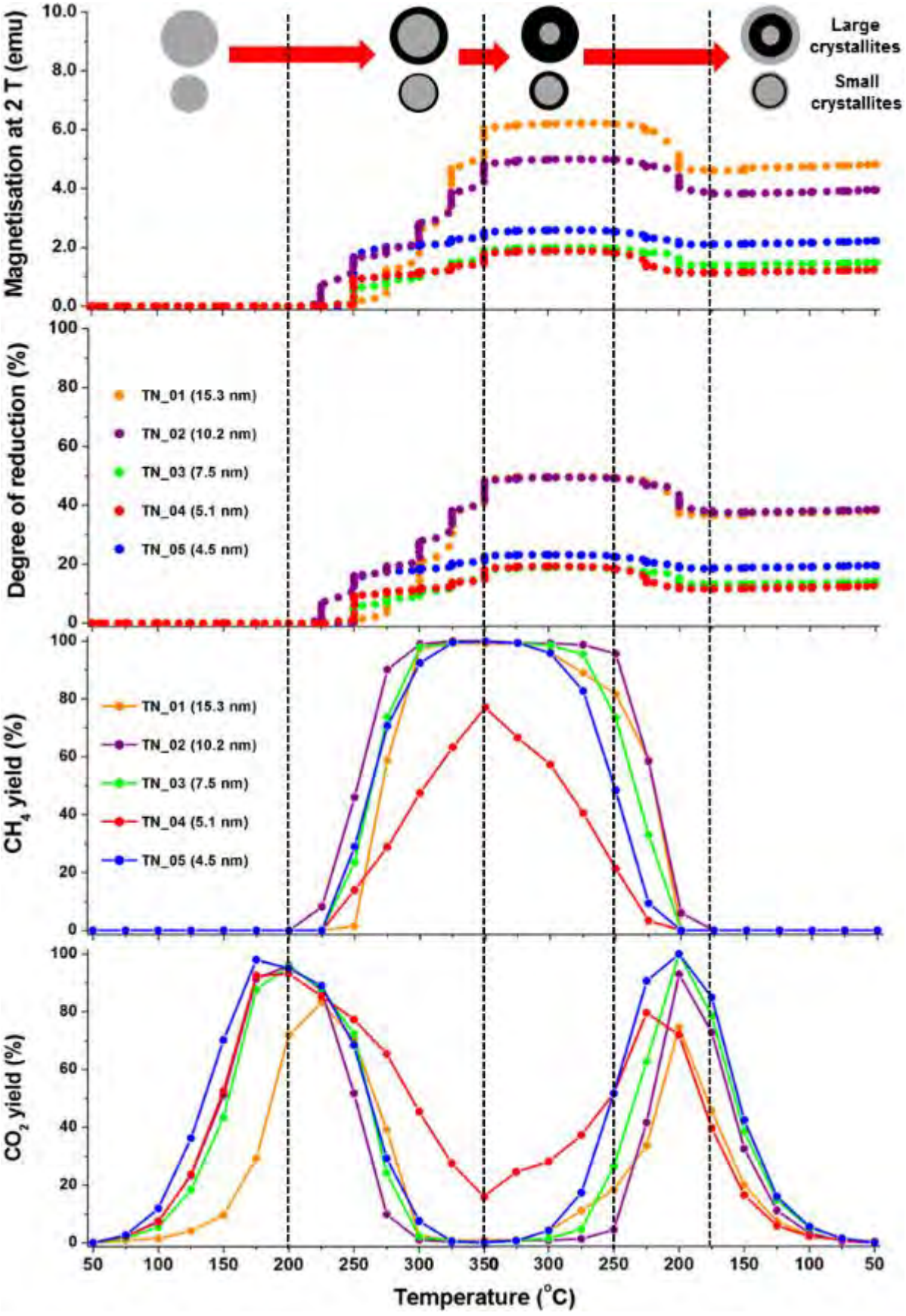

Figure 6.8: *Sample magnetisation, degree of reduction, CH_4 yield and CO_2 yield as a function of temperature for TN_01 - TN_05.*

The partial reduction of the oxide-rich particles is believed to occur from the outside as shown in Figure 6.8 creating a metallic shell (Sadasivan *et al*., 2013). Increasing the temperature increased the thickness of the metallic shell (*i.e.,* the degree of reduction) greatly for the larger crystallites compared to the smaller ones.

Decreasing the reaction temperature to below 250 °C caused a partial loss of the metallic phase via re-oxidation forming an oxide outer-shell. It is possible that the re-oxidation may have started above 250 °C but it could be the loss of metallic cobalt was not significant (*i.e.,* the oxide outer-shell was not thick enough) to be detected in the magnetometer. The gradual increase in the CO_2 yield below 350 °C over each catalyst seems to support the aforementioned point (see Figure 6.8). Below 175 °C, no significant changes in the sample magnetisations and degree of reduction were observed. Methane formation was also not observed below 175 °C due to the absence of surface metallic cobalt species. However, CO_2 was still formed at these temperatures with the yields decreasing with temperature as expected.

At 50 °C after the test run was completed, an M-H measurement (*i.e.,* magnetisation as a function of the field strength) was taken. The external magnetic field was varied from -2 to 2 T and brought back to -2 T with the sample magnetisation was measured at each field strength. Figure 6.9 shows the plotted data obtained from this measurement for TN_01, TN_03 and TN_05. (See Appendix E for the plots of TN_02 and TN_04). It is clear from the plots that all three catalysts had material displaying remnant magnetisation at 0 T in them which is indicated by the hysteresis behaviour observed in each plot. However, the relative width of the hysteresis qualitatively indicates the relative amount of material displaying remnant magnetisation at 0 T (γ) *i.e.,* the amount of cobalt crystallites with a size above cobalt's critical size for superparamagnetism (Dalmon, 1994).

Table 6.1 shows the calculated γ value for each catalyst using Equation 4.6 and what can be observed is that the relative amount of material displaying remnant magnetisation at 0 T increased with an increase in the starting crystallite size of Co_3O_4. Since the exact threshold (*i.e.,* critical crystallite size) for the transition from superparamagnetism to ferromagnetism is not known for sure yet for cobalt (both fcc and hcp) and how this threshold can be further influenced by temperature, it remains difficult to qualitatively determine whether the crystallites have sintered or not. Also the possible presence of crystallites having a double-shell structure may also make it more difficult to interpret the M-H data obtained since the crystallites would also have some oxide material together with metallic Co. For post-run crystallite size

analysis, PXRD and/or TEM may be more helpful. Nonetheless, the γ values show a reasonable trend.

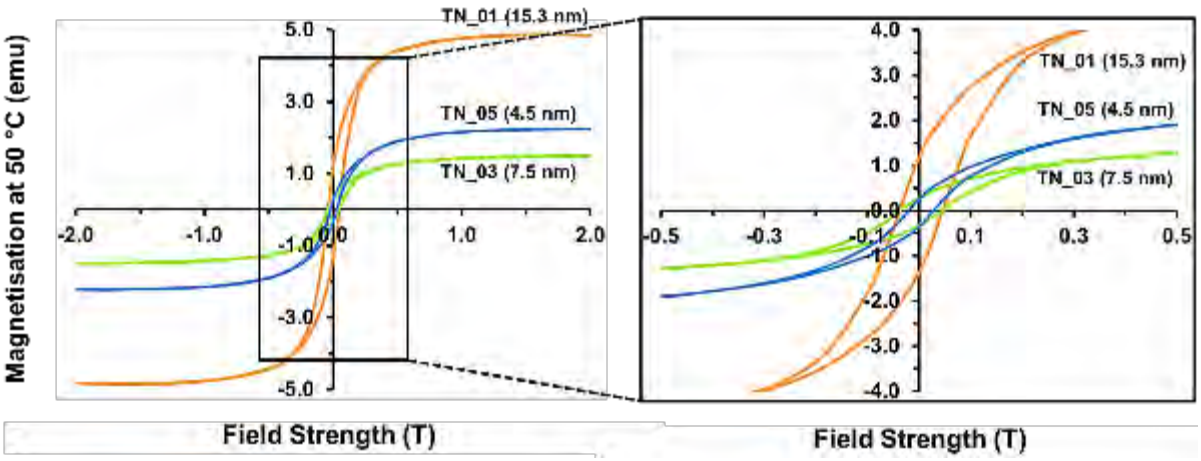

Figure 6.9: *(**left**) Sample magnetisation as a function of the external field at 50 °C for TN_01, TN_03 and TN_05. (**right**) Zoomed-in view showing the width of the hysteresis in each plot.*

Table 6.1: *Calculated relative amount of material displaying remnant magnetisation at 0 T (γ) in each catalyst sample at 50 °C.*

Sample Name	γ (wt.-%) at 50 °C
TN_01 (15.3 nm)	49.6
TN_02 (10.2 nm)	45.1
TN_03 (7.5 nm)	39.4
TN_04 (5.1 nm)	34.1
TN_05 (4.5 nm)	26.2

6.2.2. Effect of metal-support interactions

The H_2-TPR experiments confirmed that four catalysts with different metal-support interactions were synthesised (see Figure 5.10). The catalysts synthesised by contacting the support with the metal precursor still dissolved in the microemulsion (*i.e.,* RM_2 and RM_3) were much harder to reduce. From the catalytic test results, RM_2 and RM_3 where consequently less active compared to the catalysts RM_1 and RM_4 between 50 and 350 °C along the heating profile. Magnetic studies were also conducted on these four catalysts to investigate their reducibility under CO-PROX conditions. Figure 6.10 shows the sample magnetisation and degree of reduction as a function of temperature for each of the four catalysts. Also shown with these two plots are the methane and CO_2 yields, respectively.

It is clear that RM_1 and RM_4 reduced to form metallic cobalt under CO-PROX conditions. RM_4 reduced at 225 °C while RM_1 reduced at 250 °C. These onset reduction temperatures were in good agreement with the onset temperature for methane formation as shown in Figure 6.10. RM_4 reduced to Co over a narrower temperature range during H_2-TPR experiments compared to RM_1 and again, this was attributed to the weaker metal-support interactions in RM_4 (as also observed by Fischer *et al.* (2012)). The magnetic studies showed that RM_4 reduced to a much greater extent than RM_1 at temperatures above 250 °C. In RM_1 and RM_4, the metallic cobalt formed was also partially re-oxidised possibly to CoO between 200 and 250 °C along the cooling profile. As observed with the first series of catalysts discussed earlier, the restoration of the CO oxidation activity over RM_1 and RM_4 can be attributed to the establishment of new CO oxidation active sites through the re-oxidation of metallic cobalt. Crystallites with a double-shell structure are believed to be present in both RM_1 and RM_4 after completion of the catalytic test.

RM_2 and RM_3 showed slight indications for the formation of metallic Co above 300 °C as shown by Figure 6.11. This explained the relatively low CH_4 yields observed for these two catalysts. As mentioned in sub-section 4.3.1.1, the detection limit of the magnetometer is 0.025 emu which corresponds to a mass of 0.14 mg of cobalt at 350 °C. From Figure 6.11, RM_2 and RM_3 showed maximum magnetisations just below 0.04 emu which correspond to a mass of metallic Co below 0.23 mg.

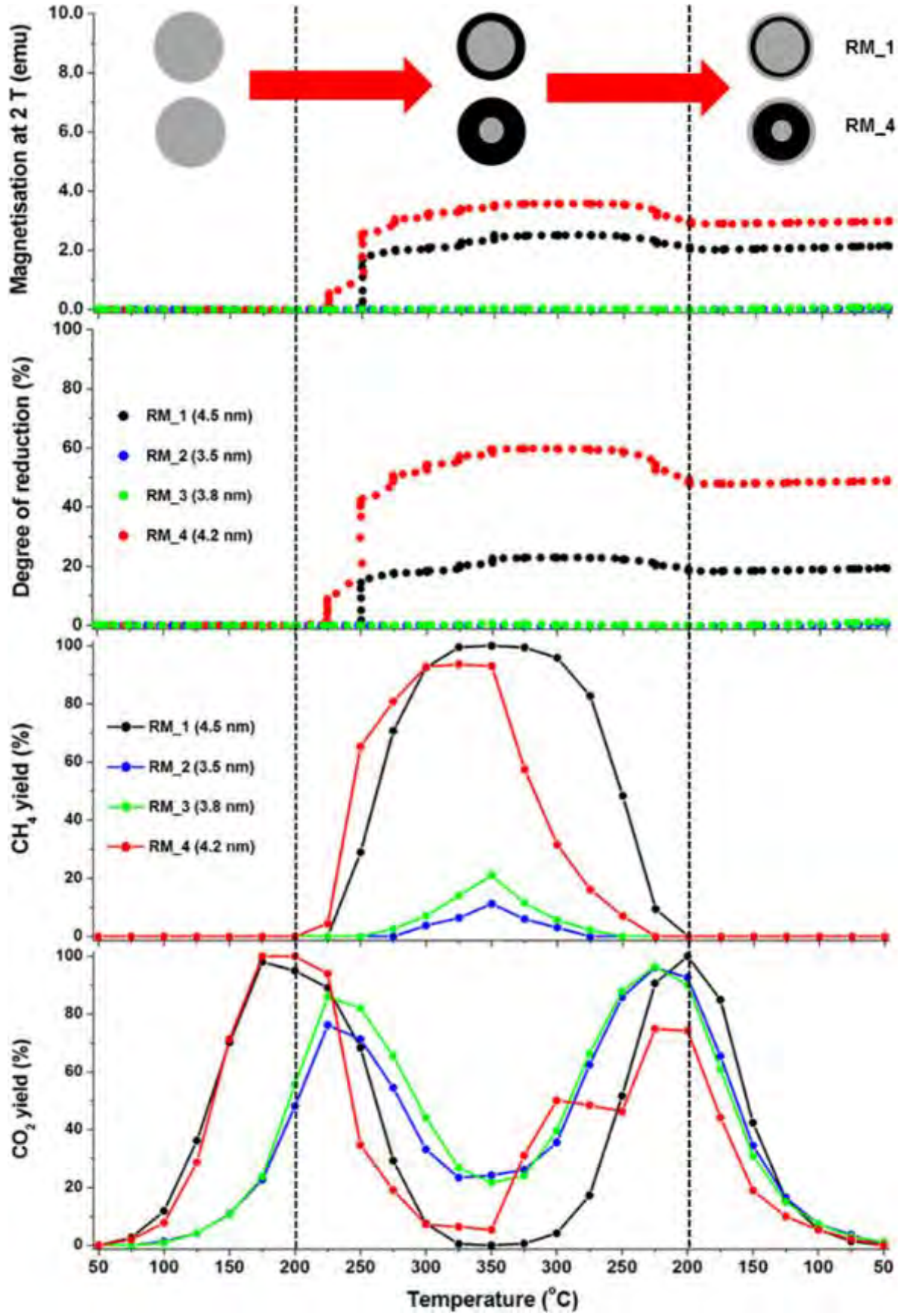

Figure 6.10: *Sample magnetisation, degree of reduction, CH_4 yield and CO_2 yield as a function of temperature for RM_1 - RM_4.*

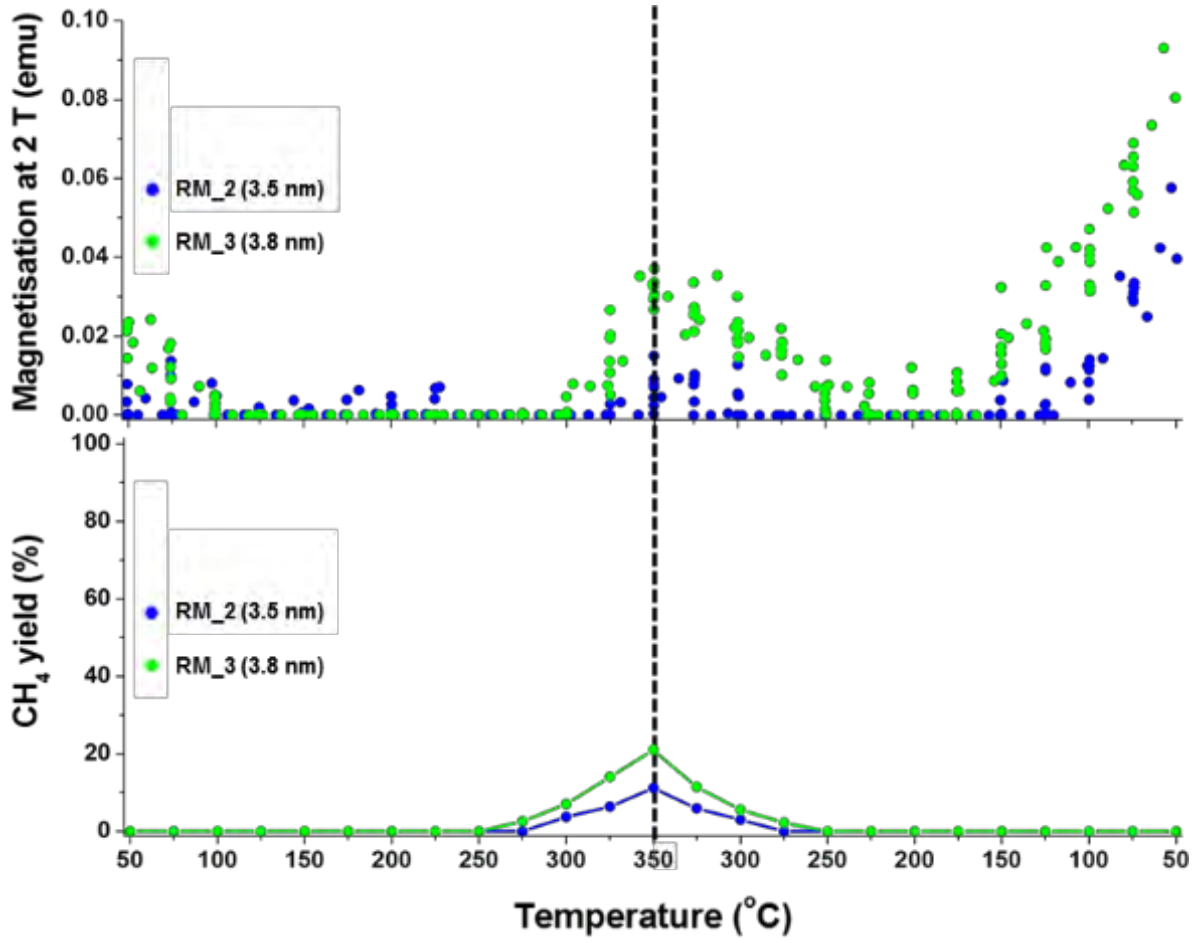

Figure 6.11: *Sample magnetisation and CH_4 yield as a function of temperature for RM_2 and RM_3.*

Even though there may be error in the measurement and in the calculation of the amount of metallic Co thought to be present, part of the observed increase in magnetisation at high temperatures does indicate that some magnetic material was formed. The decrease in magnetisation below 350 °C may also point towards re-oxidation of Co to CoO which ultimately terminated CH_4 formation at 225 °C and restored CO oxidation activity as shown in Figure 6.10.

The magnetisation observed in the 50 – 100 °C range upon heating may be due to the presence of paramagnetic species (*i.e.,* Co_3O_4 and γ-Al_2O_3). As expected, the magnetisation decreases with increasing temperature. The rapid increase in magnetisation below 175 °C upon cooling may be a cumulative result of the presence of paramagnetic species (*i.e.,* CoO and γ-Al_2O_3) and possibly very little amounts of metallic Co which may have not been re-oxidised.

In an attempt to explain the higher CO oxidation activity displayed by RM_2 and RM_3 upon cooling the reactor, it could be that the re-oxidised particles were no longer strongly interacting with the support. The segregation of nanoparticles from the support has been observed by Zeng *et al.* (2014) with their CuO-supported CeO_2 inverse catalyst under CO-PROX conditions. They compared a fresh 50 wt.-% CeO_2/CuO catalyst with its spent counterpart under HRTEM and observed two things. The CuO support had reduced to metallic copper (Cu) and also had separated from the CeO_2 nanoparticles. It is well accepted in the literature that in CuO/CeO_2 and CeO_2/CuO catalysts, the support supplies the oxygen species for oxidising the adsorbed CO (Jia *et al.*, 2010; Zeng *et al.*, 2013). However upon reduction of the CuO support, the formed metal possesses no oxygen species which it can supply for oxidising adsorbed CO which then decreases the activity of the CeO_2/CuO catalyst (Zeng *et al.*, 2014). Contrary to what Zeng *et al.* (2014) observed, it could be that in this study, the partial reduction of Co_3O_4 and the subsequent re-oxidation of the small amounts of metallic Co resulted in the separation of the nanoparticles from the support thus increasing their activity.

At 50 °C, an M-H measurement was also performed to obtain the relative amount of material displaying remnant magnetisation (γ) at 0 T. Figure 6.12 shows the M-H plots obtained for RM_1 and RM_4. (See Appendix E for M-H plots of RM_2 and RM_3). It is also clear from these plots that there was material displaying remnant magnetisation at 0 T in both RM_1 and RM_4 with RM_4 having a higher amount of this material based on the width of the hysteresis. Table 6.2 shows the calculated relative amount of material displaying remnant magnetisation (γ) at 0 T in each catalyst and confirms what is qualitatively shown in the M-H plots in Figure 6.11. Information on the whether sintering had taken place or not during the tests, is still elusive because of the reasons already pointed out in sub-section 6.2.1.

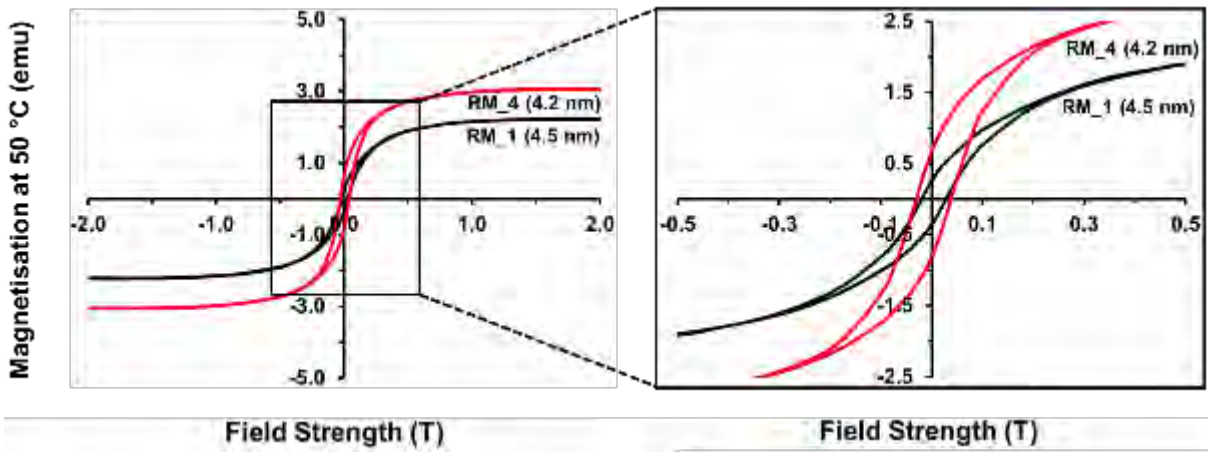

Figure 6.12: *(**left**) Sample magnetisation as a function of the external field at 50 °C for RM_1 and RM_4. (**right**) Zoomed-in view showing the width of the hysteresis in each plot*

Table 6.2: *Calculated relative amount of material displaying remnant magnetisation at 0 T (γ) in in RM_1 and RM_4 at 50 °C.*

Sample Name	γ (wt.-%) at 50 °C
RM_1 (4.5 nm)	26.2
RM_4 (4.2 nm)	46.7

6.3. *In situ* powder X-ray diffraction

In situ PXRD experiments were only performed on the samples TN_01 – TN_05 as these displayed a significant reduction behaviour during the magnetic studies. The other reason is that their initial cobalt oxide loadings and crystallite sizes were relatively high than in the case of RM_2 – RM_4. The *in situ* PXRD experiments were conducted almost in a similar manner to those conducted in the magnetometer in terms of the temperatures, the gas feed and space velocity used. The PXRD instrument allowed for the on-line monitoring of the bulk phase changes and the changes in the crystallite size occurring in the catalyst as a function of temperature. Figure 6.13 shows the on-top view of the PXRD patterns recorded as a function of temperature for the selected catalysts; TN_01, TN_03 and TN_05. (See Appendix F for the

corresponding patterns of TN_02 and TN_04). Each scan was recorded over a 7-minute period so to minimise the effect of phase changes on the PXRD scans being recorded. Consequently, this had a negative effect on the resolution in the scans as they were taken very quickly.

From the scans obtained, it can be observed that all three catalysts began to reduce to CoO at 225 °C. At 250 °C, the formation of metallic fcc cobalt was observed. It is worth noting that no hcp cobalt was observed in any of the recorded PXRD scans of all the catalysts. The presence of hcp cobalt would normally be indicated by a very intense peak at a 2θ angle of 55.7 °. TN_01 showed a very intense fcc Co peak at 51.8° above 250 °C with very faint CoO peaks at 49.7° and 72.9°. TN_03 and TN_05 displayed relatively clear and broad CoO peaks at 49.7 and 72.9° even after the appearance of the fcc cobalt peak at 51.8°. This observation was in very close agreement with the reduction behaviour observed in the magnetometer where TN_03 and TN_05 showed low degrees of reduction compared to TN_01 (see Figure 6.6). Furthermore, evidence for the presence of crystallites with a CoO core and a metallic Co shell was revealed in these experiments.

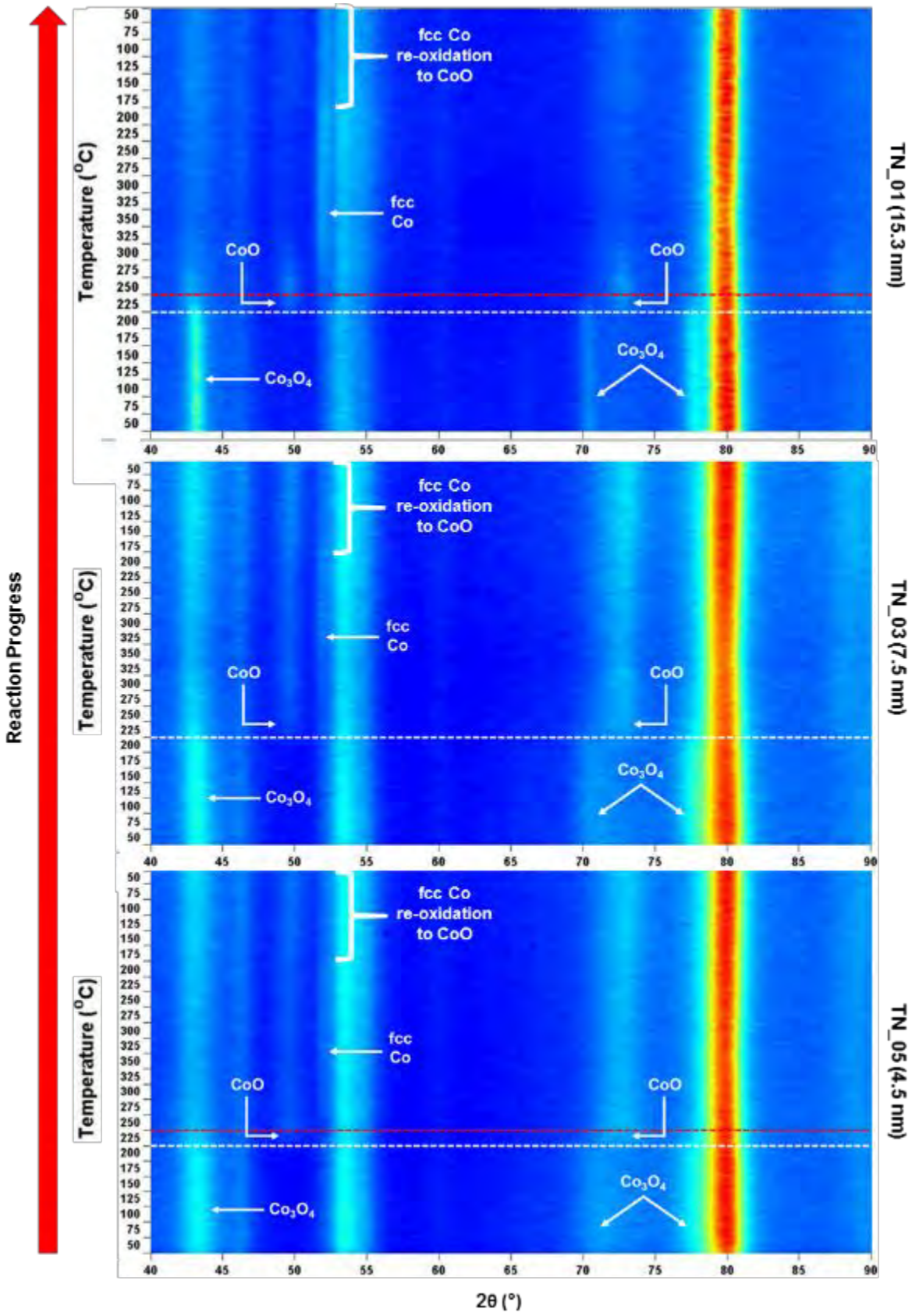

Figure 6.13: *On-top view of the in situ PXRD patterns recorded for (**top**) TN_01, (**middle**) TN_03 and (**bottom**) TN_05 as a function of temperature. The white and red dotted lines indicate the temperature at which the CoO and fcc Co phases were first observed, respectively.*

Upon cooling the reactor, changes in the phase composition in each catalyst were only observed at 175 °C where the metallic Co peak at 51.8° began to lose intensity (but not completely) with the CoO peaks at 49.7 and 72.8° simultaneously showing a slight increase in intensity for all three catalysts. This observation confirmed the re-oxidation of metallic cobalt as it was also observed in the magnetometer by a decrease in the sample magnetisation between 175 and 250 °C (see Figure 6.6). Although the PXRD detected this re-oxidation behaviour slightly later than the magnetometer, it should be noted that the magnetometer is highly sensitive to magnetic (*i.e.,* metallic) materials compared to PXRD. Therefore, the magnetometer is expected to capture any changes to the metallic cobalt phase much more readily than the *in situ* PXRD instrument (Fischer *et al.*, 2014).

This observed partial re-oxidation further supports the idea of double-shell structured crystallites being present at the end of each test run. The re-appearance of Co_3O_4 was not observed as CoO remained as the only visible cobalt oxide phase. The presence of CoO and continued oxidation of CO along the cooling profile suggested that the Co^{3+} ion (or bulk Co_3O_4) is not required for the oxidation of CO (Ko *et al.*, 2006; Mankidy *et al.*, 2014; Teng *et al.*, 1999). In a study done by Teng *et al.* (1999) where they compared CoO and Co_3O_4 (with MnOOH and CuO) catalysts under CO-PROX conditions. They found that CoO was more active than Co_3O_4 showing higher and more stable CO conversions over a wider temperature range.

Crystallite size analysis and the quantification of the different phases observed proved to be challenging using Rietveld refinement in the Topas 4.1 software as inaccurate and/or unreliable information was obtained. The possible presence of single- or double-shell structured crystallites at the different temperatures, could have resulted in the inaccurate determination of crystallite sizes and the mass fractions of each phase. *In situ* PXRD analysis on the Bruker D8 Advance Laboratory X-ray diffractometer (with a cobalt source: λ = 1.78897 Å) used in this study allows for the detection of crystallites with a size above 2 – 3 nm. Also, the mass-fractions of each chemical phase must at least be above 2 – 3 wt.-% for reliable quantification (Fischer, 2011). Therefore, with these different core-shell structures, the thickness of the shell(s) and the diameter of the core may have not been large enough to enable for their accurate quantification and accurate size determination by Rietveld refinement.

6.4. Catalytic evaluation and *in situ* characterisation: A further discussion

The catalytic evaluation studies have shown that the mass-specific CO conversions to CO_2 increased with a decrease in the starting crystallite size of Co_3O_4 along the heating and cooling temperature profiles. These experiments also showed that there was a decline in the CO_2 yields above 200 °C which was shortly followed by methane formation. Methanation occurred due to the partial reduction of the CoO phase to Co which was adequately confirmed during the *in situ* magnetic and PXRD studies. The reduction of larger crystallites was more pronounced than for the smaller crystallites due to the existence of relatively weak metal-support interactions in the catalysts with large crystallites. Decreasing the reaction temperature decreased the formation of methane and gradually restored the CO oxidation activity over each catalyst. Between 175 and 250 °C, both *in situ* instruments revealed that metallic fcc cobalt was partially re-oxidised to CoO. This also explained the gradual establishment of new CO oxidation active sites upon decreasing the reaction temperature. Further re-oxidation to Co_3O_4 was not observed during the *in situ* PXRD experiments which suggested that the Co^{3+} ion species was not required for the oxidation of CO (Ko *et al.*, 2006; Mankidy *et al.*, 2014; Teng *et al.*, 1999).

When looking at the effect of crystallite size on the conversion of CO, the appropriate descriptor to report is the surface area-specific rate or turnover frequency (TOF). This is done by normalising the activity (or conversions) by the exposed active surface area (Cuenya & Behafarid, 2015). In principle, this can be done for the kinetic data obtained in this study as well. The first assumption made was that changes in the crystallite size due to sintering were negligible under the set reaction conditions. However, changes in the crystallite size due to the reduction of Co_3O_4 should be accounted for. Table 6.3 shows the obtained Co_3O_4 number-based TEM average sizes for the first series of catalysts (*i.e.,* TN_01 – TN_05). More importantly, the table also shows the theoretical average diameters of pure CoO and Co crystallites, respectively, upon reduction of the Co_3O_4 phase in these catalysts.

These theoretical sizes were calculated by considering Equations 6.1 and 6.2 which show the two-step reduction of Co_3O_4 to metallic Co. The mass lost during the reduction of Co_3O_4 to CoO is approximately 7% and the mass lost when reducing CoO to Co is approximately 21%. Knowing this and the density of CoO (6.44 g/cm^3) and Co (8.9 g/cm^3), the volume and diameter of the pure CoO and Co crystallites could be calculated also assuming perfect spherical

crystallites in each case. Notice that the decrease in crystallite size from Co_3O_4 to CoO is approximately 4% and the decrease in crystallite size upon reducing CoO to Co is approximately 17%.

Table 6.3: *TEM sizes of Co_3O_4 crystallites and the calculated sizes of pure CoO and Co crystallites.*

Sample Names	TEM number-based Co_3O_4 average crystallite size (nm)	Theoretical average size of pure CoO crystallites (nm)	Theoretical average size of pure metallic Co crystallites (nm)
TN_01	10.1	9.7	8.0
TN_02	8.5	8.2	6.8
TN_03	6.1	5.9	4.9
TN_04	3.8	3.6	3.0
TN_05	3.3	3.2	2.6

$$\boldsymbol{Co_3O_4(s) + H_2(g) \rightarrow 3CoO(s) + H_2O(g)} \qquad \textbf{Equation 6.1}$$

$$\boldsymbol{3CoO(s) + 3H_2(g) \rightarrow 3Co(s) + 3H_2O(g)} \qquad \textbf{Equation 6.2}$$

Results from the *in situ* characterisation experiments indicated a complete reduction of Co_3O_4 to CoO, however, a complete reduction of CoO to metallic Co was not achieved. Therefore, when calculating the average diameters of the crystallites at every temperature, the degree of reduction was incorporated as well. Surface area-specific CO_2 and CH_4 formation rates, respectively were calculated and reported at only three temperature regions which are shown in Figure 6.14. Temperature region 1 (*i.e.,* 50 – 200 °C) is the oxide-rich region where the crystallites are predominantly in the Co_3O_4 phase with their diameters assumed to be the number-based TEM sizes. In this region, CO is only converted to CO_2. The other two regions (*i.e.,* regions 2 and 3) were chosen because the degree of reduction and/or re-oxidation of the crystallites in each catalyst does not significantly change with temperature. This implied that the average diameter of the crystallites remained constant in these respective regions. In region

2, it is believed that the crystallites have a single metallic shell with a CoO core. The presence of such structured crystallites explains the high yields of CH_4 obtained in this region. In region 3, the crystallites are believed to have a double-shell structure with a CoO outer-shell, Co inner-shell and CoO core. Over such crystallites, CO was again exclusively converted to CO_2.

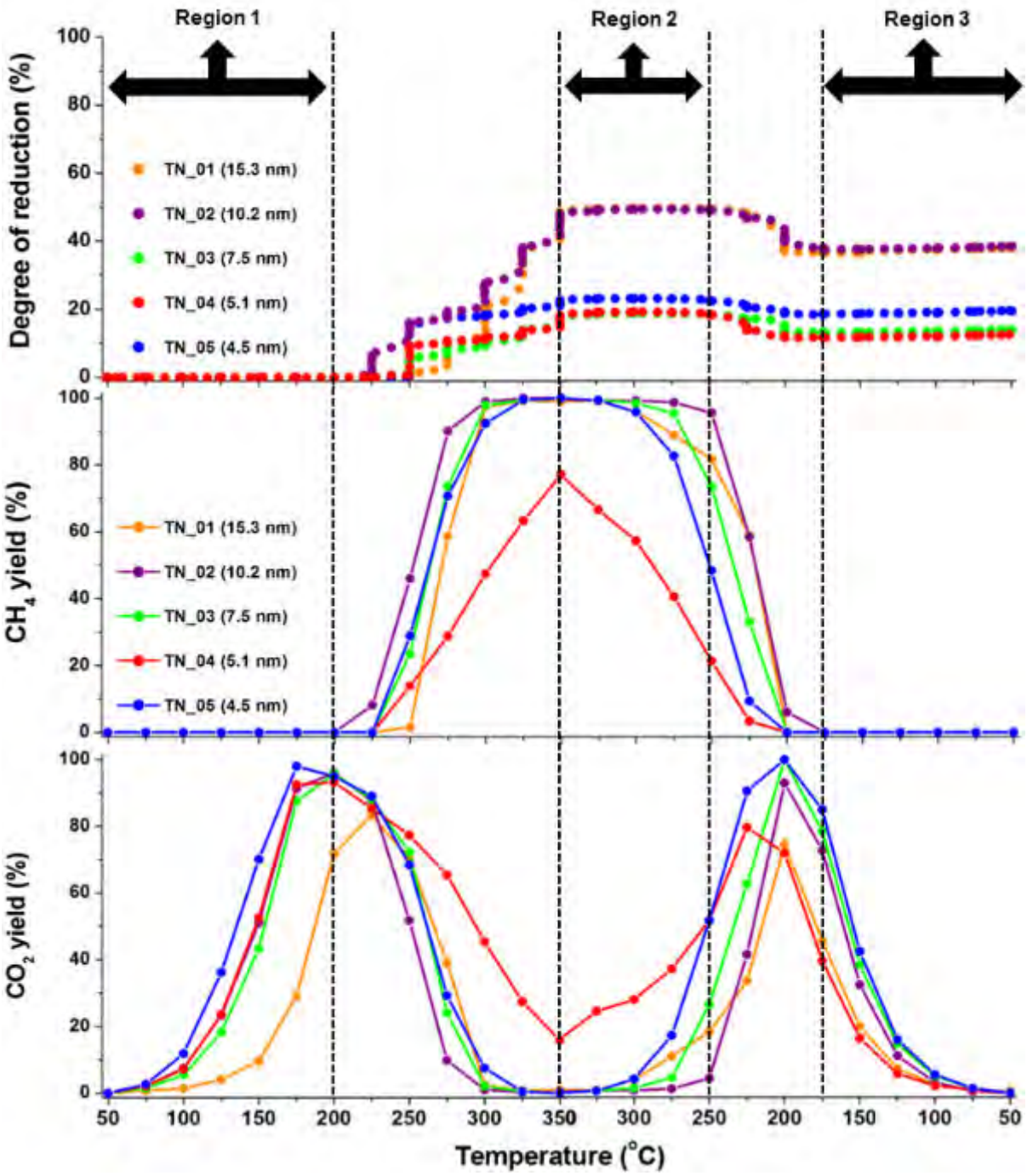

Figure 6.14: *(**top**) Degree of reduction, (**middle**) CH_4 yield and (**bottom**) CO_2 yield as a function of temperature for TN_01 - TN_05. The figure also shows the three regions where the formation rates of CO_2 (region 1 & 3) and CH_4 (region 2) were calculated.*

Table 6.4 shows the theoretical diameters of the crystallites in each catalyst in the respective temperature regions. (See Appendix G for the equations used to obtain the theoretical diameters in each case). It is well understood that these calculated average diameters obtained based on the model proposed (*i.e.,* the formation of single and double shell-structured crystallites, respectively) and the assumptions made (*i.e.,* negligible sintering) may be subject to error. In reality, the crystallites in each sample may not have sizes equal to the calculated average size and so assuming that the crystallites have the same size, could negatively affect other results obtained from calculations based on these average sizes. However, since no reliable crystallite size information could be obtained from any of the two *in situ* techniques used, the model proposed and the assumptions made here remain adequately plausible.

It can be seen from Table 6.4 that the average size of the crystallites (based on the model proposed) decreases from region 1 to region 2 as a result of metallic Co formation and that the sizes slightly increase in region 3 as a result of re-oxidation to CoO.

Table 6.4: *Average sizes of the crystallites in Regions 1, 2 and 3.*

Sample Names	Co_3O_4 TEM average crystallite size (nm): REGION 1	Theoretical diameters of crystallites (nm): REGION 2	Theoretical diameters of crystallites (nm): REGION 3
TN_01	10.1	9.0	9.2
TN_02	8.5	7.5	7.7
TN_03	6.1	5.7	5.7
TN_04	3.8	3.5	3.6
TN_05	3.3	3.1	3.1

Figure 6.15 shows the CO_2 surface formation rates in regions 1 and 3, and the surface formation rates of CH_4 in region 2 as a function of crystallite size and temperature. (See Appendix G for the equations used to obtain the formation rates). It can be seen that the surface area-specific formation rate of CO_2 increased with increasing temperature in region 1 and also that both the CH_4 and CO_2 formation rates decreased when the reaction temperature was decreased in regions

2 and 3, respectively. In region 1 above 100 °C, the CO_2 formation rates increased with increasing the starting Co_3O_4 crystallite size up to 8.5 nm above which, the CO_2 formation rate decreased. Iablokov (2011) accounted that the Co-O bonds in Co_3O_4 become stronger as the crystallites become smaller, making it difficult to release the active oxygen species for the oxidation of CO. This explains the low surface area-specific rates over the small crystallites. The larger crystallites (> 8.5 nm) display low surface rates due to the decreased number of exposed active sites (*i.e.,* Co^{2+} and/or Co^{3+}) on the surface of the crystallites.

The methane formation rates in region 2 also increased when the size of the single shell-structured crystallites increased from 3.1 to 7.5 nm but slightly decreased over the crystallites with a size of 9.0 nm. Generally, it can be seen that the larger cobalt-bearing crystallites were more active for the methanation reaction than smaller crystallites. *In situ* XAS (X-ray absorption spectroscopy) studies performed by Herranz *et al.* (2009) and Tuxen *et al.* (2013) support the above observation that larger cobalt-bearing crystallites are more active for the methanation reaction than smaller crystallites. They independently showed that the adsorptive dissociation of CO and H_2, respectively, occurs faster over larger crystallites due to the presence of larger atomic cobalt ensembles on the surface of the crystallites. Tuxen *et al.* (2013) further reported that in the presence of hydrogen, the adsorptive dissociation of CO was greatly enhanced through a hydrogen-assisted mechanism.

In region 3, the CO_2 formation rates were also higher over the assumed larger double shell-structured crystallites compared to over the smaller crystallites. This could also be attributed to the increased strength of the Co-O bond in the smaller CoO-bearing crystallites.

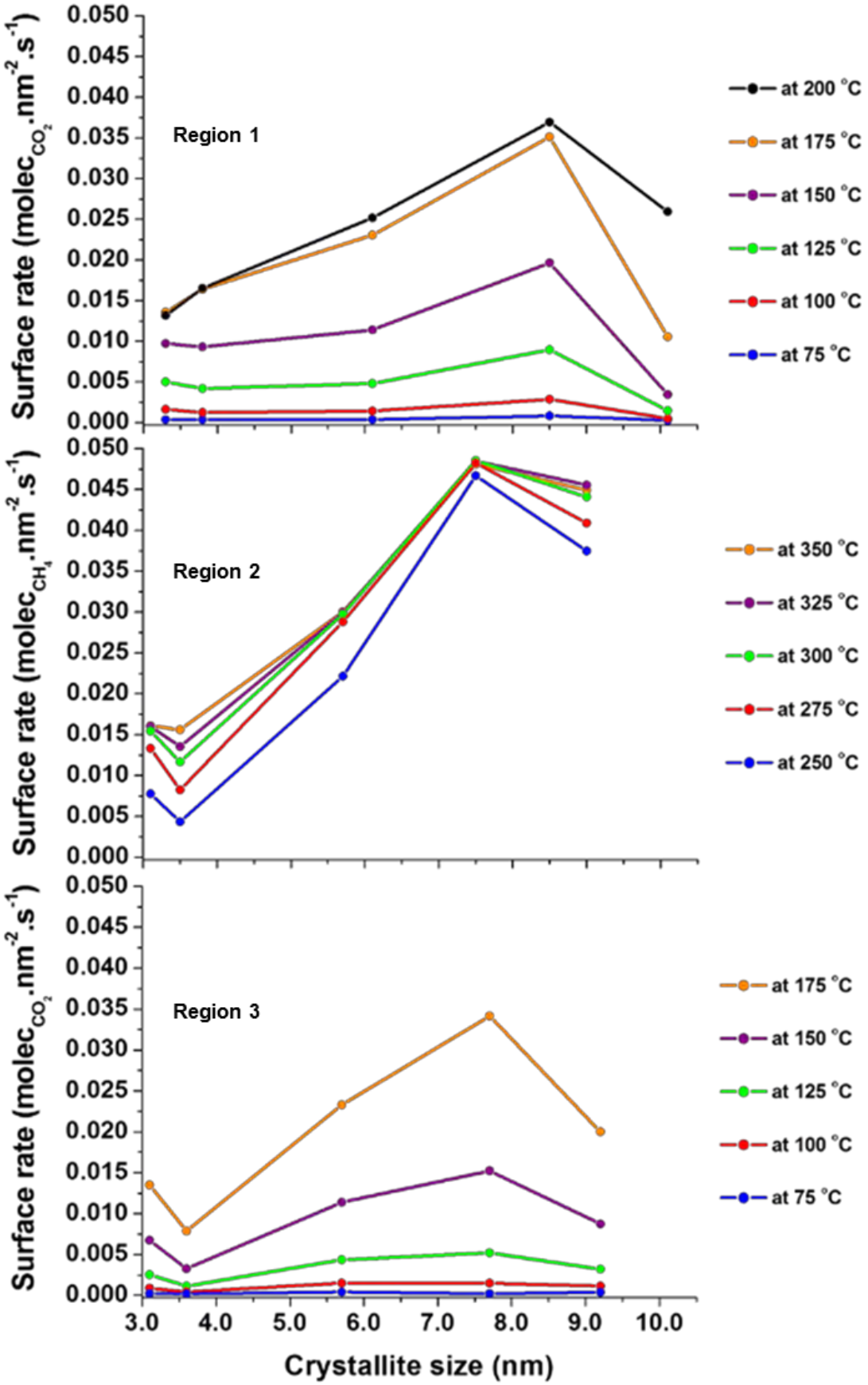

Figure 6.15: *Surface area-specific formation rates of CO_2 (Regions 1 and 3) and CH_4 (Region 2) as a function of crystallite size and temperature.*

Chapter 7: Post-run *Ex situ* Characterisation Results

7.1. Powder X-ray diffraction (PXRD)

All spent catalysts obtained after the studies in the magnetometer were characterised by PXRD to verify the chemical phases present and to monitor any crystallite size changes. Figures 7.1 and 7.2 show the PXRD patterns of the spent samples of TN_01 - TN_05 and RM_1 - RM_4, respectively. The patterns of the spent samples of TN_01 and TN_02 show the presence of fcc Co with peaks at 51.9°, 91.1° and 113.6°. CoO was present in all five spent samples showing a broad and small peak at 49.7° in each spectrum. This observation was not surprising as the catalysts TN_03 – TN_05 did show relatively low degrees of reduction in the magnetometer, which indicated that the amount of metallic cobalt formed was very little. Samples RM_2 - RM_4 showed no evidence for the presence of any cobalt phase as shown in Figure 7.2, possibly due to the presence of very small crystallites and/or small mass fractions of each cobalt phase. However, RM_1 showed the presence of CoO by a small broad peak at a 2θ angle of 49.7°. It should be noted that mass fractions below 2 – 3 wt.-% and crystallite sizes below 2 – 3 nm may not be detected in the PXRD instrument used in this study (Fischer, 2011).

Table 7.1 shows the estimated mass fraction of metallic cobalt based on the degree of reduction results obtained during the magnetic studies. TN_01 and TN_02 have mass fractions of metallic cobalt slightly above 2 wt.-% and also based on their initial Co_3O_4 crystallite sizes, the visibility of both the CoO and fcc Co in their diffraction patterns is not entirely unexpected. As mentioned already above, the different species present in the crystallites assumed to have a double shell-like structure may be difficult to detect as the thickness of each shell and the diameter of the core material may need to be of a certain size. These limitations also led to the challenges faced with obtaining accurate and reliable crystallite size information by Rietveld refinement.

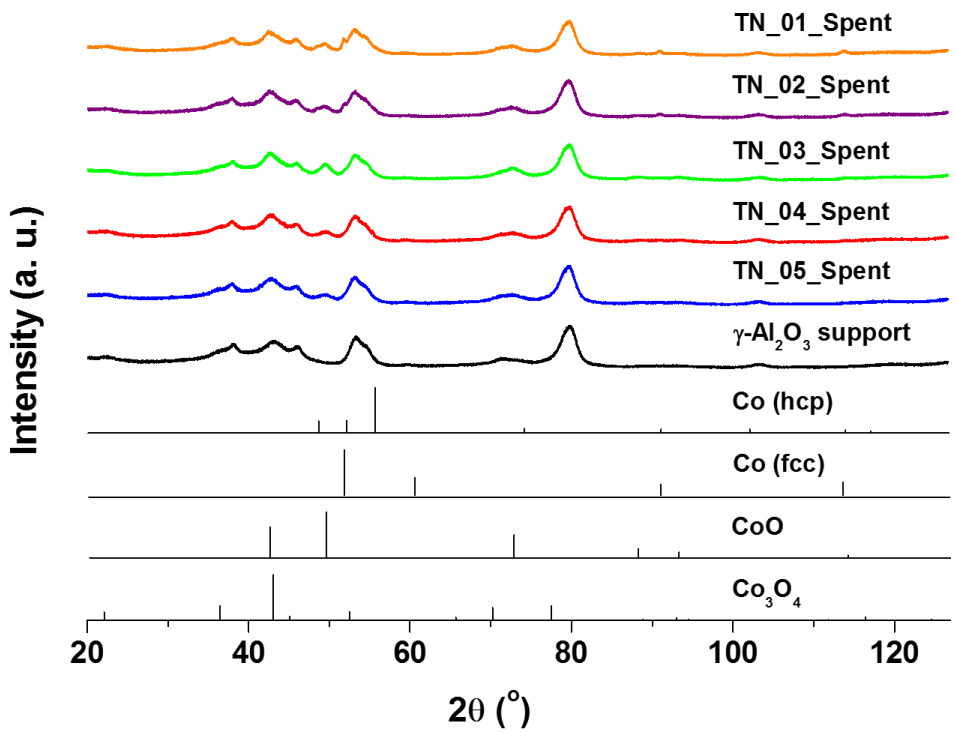

Figure 7.1: *PXRD patterns of the spent catalyst samples of TN_01 - TN_05 obtained after performing magnetic studies.*

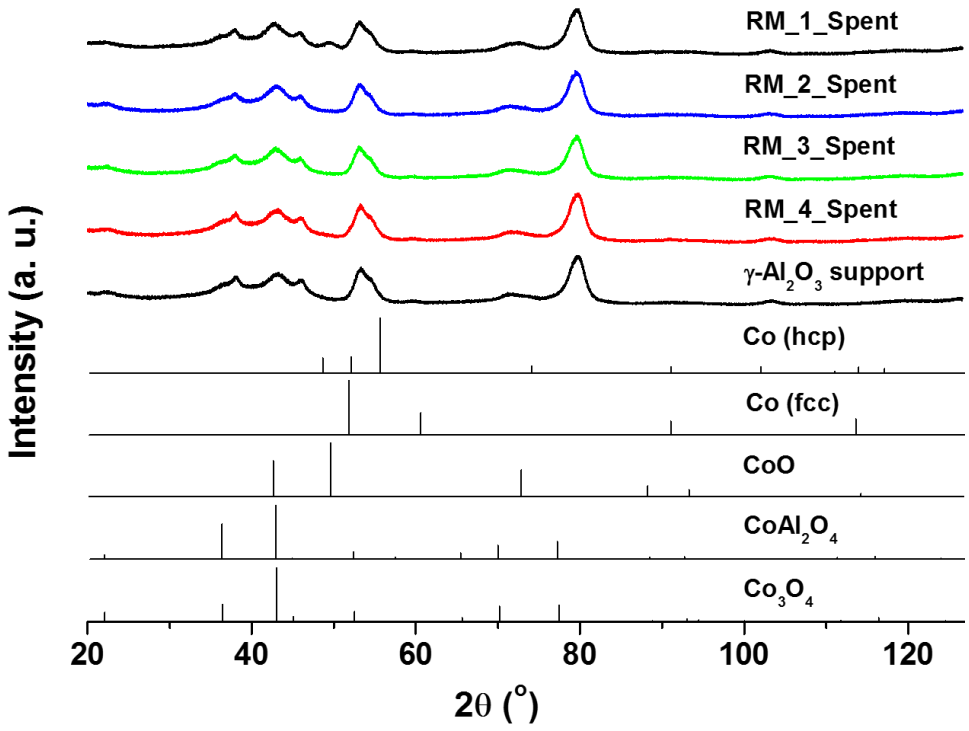

Figure 7.2: *PXRD patterns of the spent catalyst samples of RM_1 – RM_4 obtained after performing magnetic studies.*

Table 7.1: *Degree of reduction and estimated amount of metallic cobalt present at 50 °C post-magnetic studies.*

Sample Name	Degree of reduction at 50 °C post-reaction (%)	Estimated Co mass fraction (wt.-%)
TN_01	37.6	~ 3.0
TN_02	38.1	~ 2.5
TN_03	13.6	~ 0.9
TN_04	12.1	~ 0.8
TN_05 (or RM_1)	19.2	~ 1.3
RM_4	49.0	~ 1.2

7.2. Transmission electron microscopy (TEM)

TEM analysis was also conducted on the spent samples of TN_01 – TN_05 and RM_2 – RM_4 in order to determine whether any sintering had occurred during the catalytic tests in the *in situ* magnetometer instrument. Figure 7.3 shows the selected TEM micrographs of the spent samples of TN_01, TN_03 and TN_05. (See Appendix C for the TEM micrographs of TN_02 and TN_4). The obtained micrographs of the spent catalysts also displayed poor contrast between the cobalt-containing crystallites and those of the γ-Al_2O_3 support which made the identification and counting of the crystallites rather challenging. Despite this set-back, some single cobalt-containing crystallites or clusters of crystallites were identified and are annotated on the micrographs. The obtained micrographs also qualitatively indicate that no significant sintering had taken place during the CO-PROX runs. Obtaining a number-based size distribution for each spent sample of TN_01 – TN_05 was attempted and the size distributions are shown in Figure 7.3. Summarised in Table 7.2 are the number- and volume-based average sizes of the crystallites in the fresh and spent samples of TN_01 – TN_05 and it can be seen that no significant sintering took place during the catalytic tests. It is also worth mentioning that the size distributions remain fairly narrow for these five catalysts.

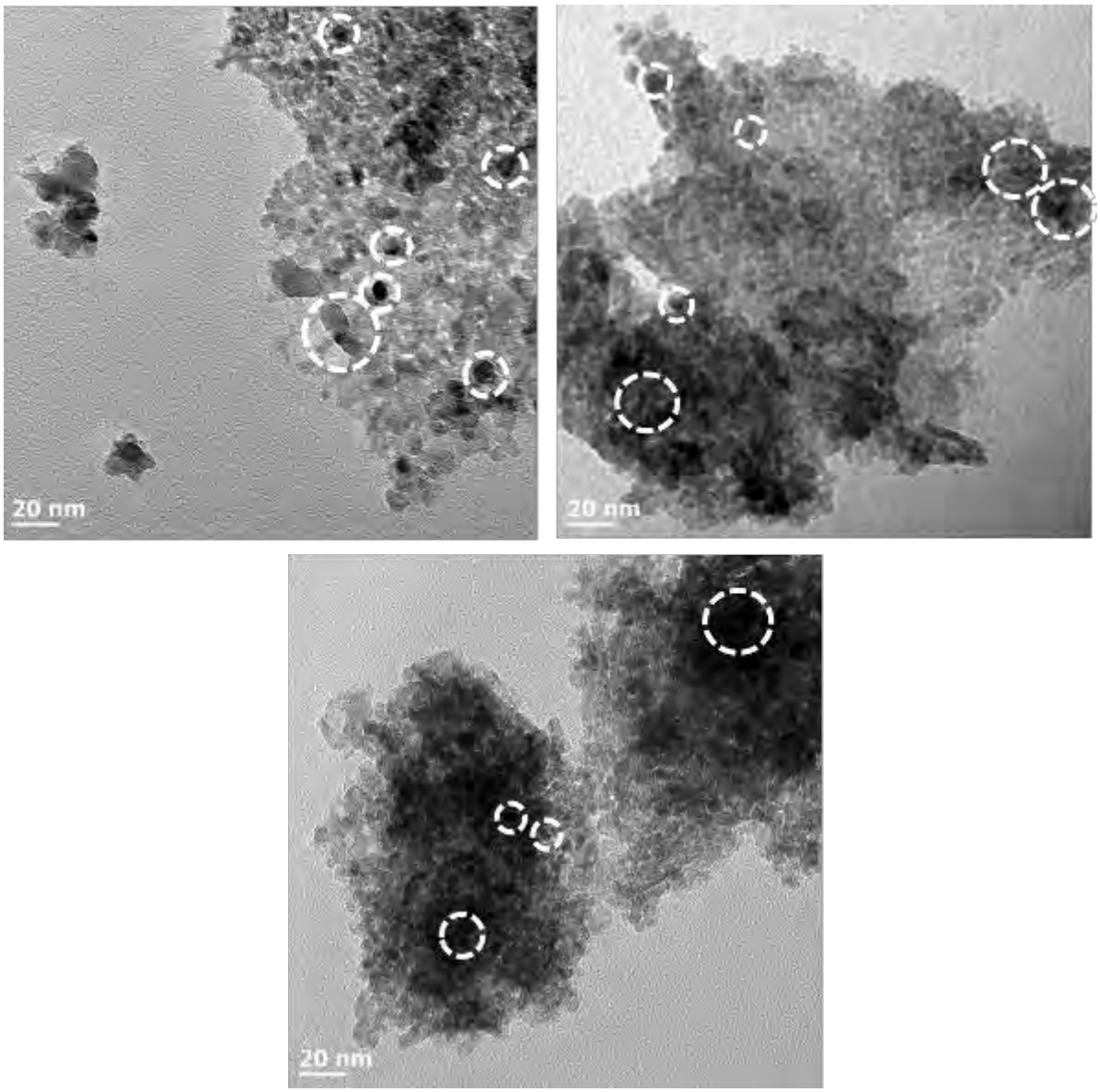

Figure 7.3: *TEM micrographs of the spent samples of (**top-left**) TN_01, (**top-right**) TN_03 and (**bottom**) TN_05. Circled with white dashed lines are some of the cobalt-containing single crystallites or group of crystallites identified.*

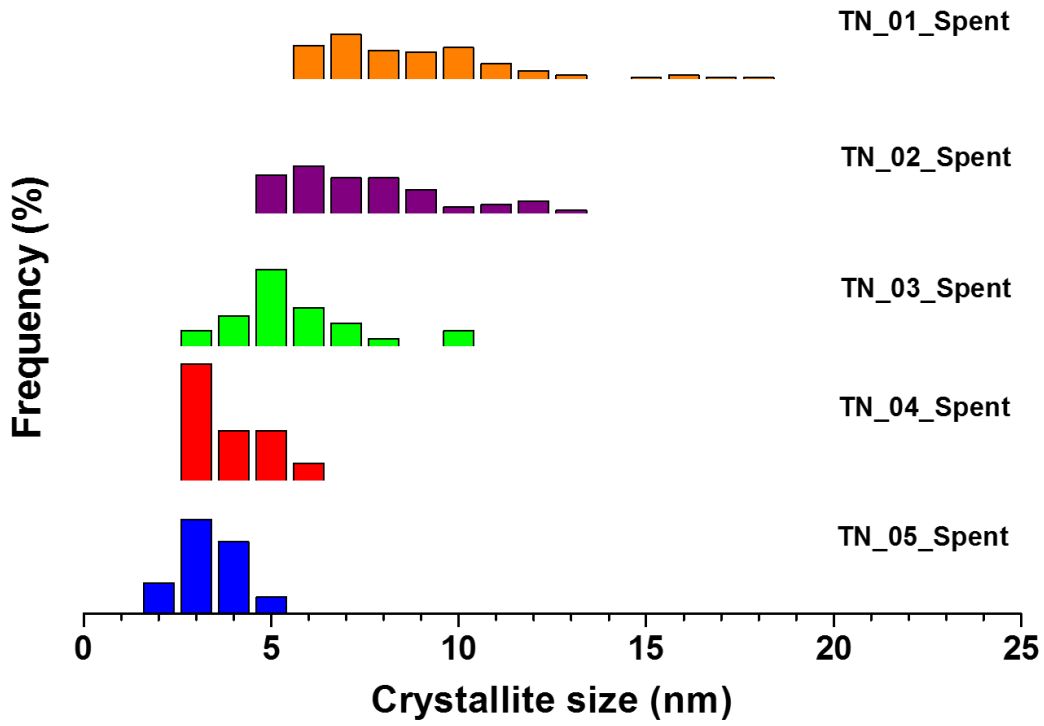

Figure 7.4: *Number-based size distributions of the spent samples of TN_01 - TN_05 obtained by TEM analysis.*

Table 7.2: *Number- and volume-based crystallite sizes of the fresh and spent samples of TN_01 – TN_05 obtained by TEM analysis.*

	FRESH SAMPLES		SPENT SAMPLES	
Sample Name	**Actual size[a] (nm)**	**Actual size[b] (nm)**	**Actual size[a] (nm)**	**Actual size[b] (nm)**
TN_01	10.1 ± 2.8	13.8 ± 3.2	9.5 ± 3.1	14.3 ± 3.8
TN_02	8.5 ± 1.7	9.5 ± 1.9	7.9 ± 2.0	9.5 ± 2.2
TN_03	6.1 ± 1.5	7.2 ± 1.6	6.0 ± 1.7	7.7 ± 2.2
TN_04	3.8 ± 0.8	4.5 ± 1.0	4.4 ± 1.1	5.2 ± 1.2
TN_05	3.3 ± 0.6	3.7 ± 0.7	3.8 ± 0.7	4.2 ± 0.8

[a] TEM number-based average crystallite sizes obtained using Equations 4.1 and 4.3

[b] TEM volume-based average crystallite sizes obtained using Equations 4.2 and 4.4

Figures 7.5 and 7.6 are the TEM micrographs and number-based size distributions of the cobalt-containing spent catalysts of RM_1 – RM_4, respectively. Table 7.3 shows the TEM number- and volume-based average sizes of the crystallites in the fresh and spent samples of RM_1 – RM_4. It can also be seen that no significant sintering or changes in the size distribution of each sample had taken place as also seen with the first series of catalysts.

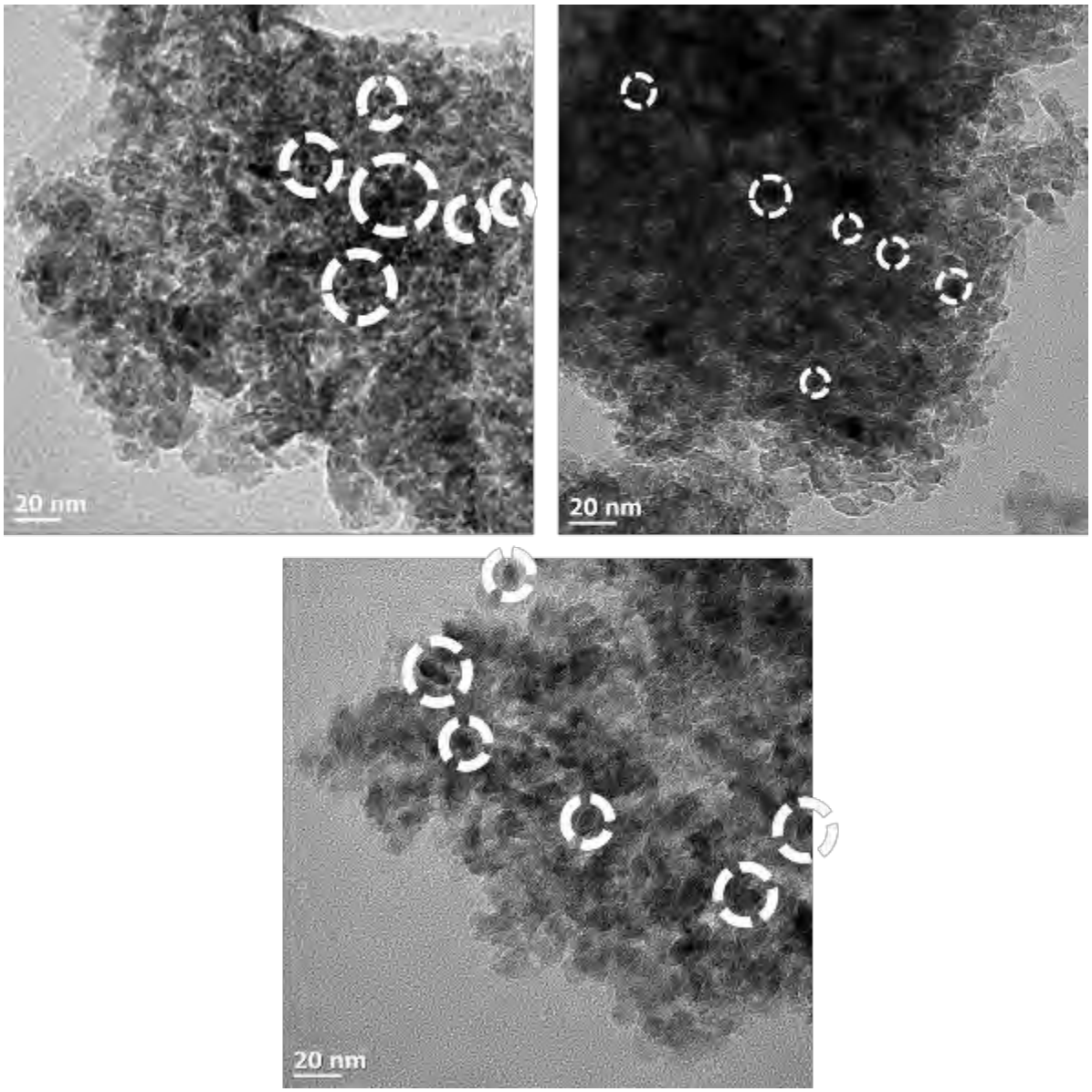

Figure 7.5: *TEM micrographs of the spent samples of (**top-left**) RM_2, (**top-right**) RM_3 and (**bottom**) RM_4. Circled with white dashed lines are some of the cobalt-containing single crystallites or group of crystallites identified.*

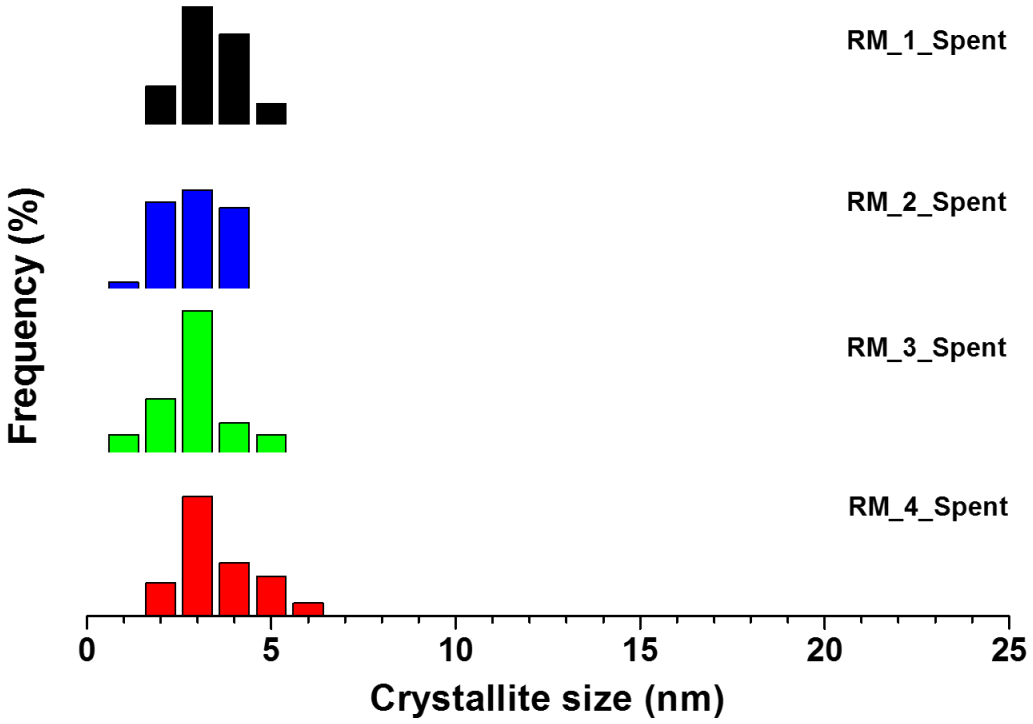

Figure 7.6: *Number-based size distributions of the spent samples of RM_1 - RM_4 obtained by TEM analysis.*

Table 7.3: *Number- and volume-based crystallite sizes of the fresh and spent samples of TN_01 – TN_05 obtained by TEM analysis.*

	FRESH SAMPLES		SPENT SAMPLES	
Sample Name	**Actual size[a] (nm)**	**Actual size[b] (nm)**	**Actual size[a] (nm)**	**Actual size[b] (nm)**
RM_1 (TN_05)	3.3 ± 0.6	3.7 ± 0.7	3.8 ± 0.7	4.2 ± 0.8
RM_2	3.3 ± 0.7	3.7 ± 0.8	3.5 ± 0.7	3.9 ± 0.8
RM_3	3.2 ± 0.8	3.9 ± 0.9	3.4 ± 0.9	4.1 ± 1.0
RM_4	3.8 ± 0.9	4.4 ± 1.0	4.0 ± 1.0	4.8 ± 1.1

[a] TEM number-based average crystallite sizes obtained using Equation 4.1 and 4.3

[b] TEM volume-based average crystallite sizes obtained using Equations 4.2 and 4.4

Chapter 8: General Summary and Conclusions

Producing CO-free hydrogen for fuel cell applications continues to be of great importance as it contributes greatly towards the growth of the fuel cell technology. The preferential oxidation of CO has been identified as the most efficient and cost-effective route to producing cleaner hydrogen in this regard (Gray & Petch, 2000). However, finding a cheap, active and stable catalyst is still a major downside to CO-PROX.

The current study investigated $Co_3O_4/\gamma\text{-}Al_2O_3$ as a cheaper alternative and promising catalyst for the CO-PROX reaction. The specific goals were to closely look at the effect of crystallite size and metal-support interactions on its activity, selectivity and chemical stability under CO-PROX conditions. Model catalysts with varying Co_3O_4 crystallite sizes were synthesised using the reverse micelle method which allowed for reasonably good size control. This method was also used to synthesise catalysts with different metal-support interactions. The *ex situ* techniques used (PXRD, TEM, EDX and H_2-TPR) all gave vital information about the synthesised catalysts which was in line with the primary objectives of the study.

Catalytic tests conducted in the *in situ* magnetometer and PXRD capillary cell reactors, respectively, allowed for the real-time analysis of the prepared catalysts under reaction conditions (Fischer *et al.*, 2014). Tests performed on the first series of catalysts (TN_01 – TN_05) revealed that the mass-specific CO oxidation activity increased with a decrease in the starting crystallite size of Co_3O_4. On the other hand, the surface area-specific rates displayed an opposite trend for crystallites in the 3 – 8.5 nm size range. Above 8.5 nm, the surface area-specific rate decreased because of the low mass-specific surface area of the larger crystallites. Studies in the magnetometer and PXRD capillary cell revealed that the partial reduction of Co_3O_4 occurs in the 200 – 250 °C temperature range along the heating profile with the larger crystallites reducing to a higher degree than the smaller ones. For the first time, the formation

of methane could be directly correlated with the formation of metallic cobalt in real-time. When decreasing the reaction temperature to below 250 °C, the metallic Co formed partially re-oxides to CoO which terminated the formation of CH_4 and restored CO oxidation activity. It is proposed that the partial oxide reduction and successive partial metal re-oxidation of the nanoparticles may have resulted in the formation of nanoparticles with a double-shell structure having a CoO core, metallic Co inner-shell and CoO outer-shell at the end of the catalytic tests.

Catalytic testing on the second series of catalysts (*i.e.,* RM_1 – RM_4) in the magnetometer revealed that the catalysts with relatively weaker metal-support interactions (RM_1 and RM_4) were more active but much easier to partially reduce to metallic Co. RM_4 exhibited higher degrees of reduction compared to RM_1 due to the relatively weaker interactions in RM_4. The catalysts RM_2 and RM_3 showed very little reduction behaviour and as a result, formed less than 20% methane even at 350 °C. Nonetheless, in all four catalysts, methane formation could be directly linked to the formation of metallic Co in real-time. Upon cooling the reactor, RM_1 and RM_4 were partially re-oxidised to CoO possibly leading to the formation of double-shell structured nanoparticles. RM_2 and RM_3 along the cooling profile appeared to be more active compared to their previously observed activity along the heating profile. This could be due to the segregation of the previously strongly-bound cobalt-bearing nanoparticles from the support.

Chapter 9: Recommendations for Future Work

The study presented in this dissertation aimed at looking at two effects with regards to the CO-PROX reaction: i) crystallite size and ii) metal-support interactions. A great deal of new knowledge has emanated from this study and with that said, other avenues have opened up which are worthy to investigate as future studies.

- The same supported Co_3O_4 catalysts (*i.e.,* TN_01 – TN_05 and RM_1 – RM_4) can be used for investigating the effect of crystallite size and metal-support interactions in a realistic CO-PROX environment *i.e.,* in the presence of H_2O and CO_2. This would give a complete idea as to how these catalysts could be further developed for possible use in industry.

- For the catalysts RM_2 – RM_4, higher loadings can be aimed as this could improve their analysis during *ex situ* and *in situ* PXRD studies as well as during the *in situ* magnetic studies.

- Surface-sensitive *ex situ* techniques, including X-ray photoelectron spectroscopy (XPS), can be used for the analysis of all the fresh and spent catalyst samples. It would be worth looking into the Co^{2+}/Co^{3+} and Co^{0}/Co^{2+} ratios on the surface and correlate this to the observed activity of each catalyst and reduction behaviour. The presence of double shell-structured crystallites in the spent catalysts may be confirmed. Also, *ex situ* XPS studies may prove to be useful in understanding the enhanced catalytic behaviour of RM_2 and RM_3 observed upon decreasing the reaction temperature to below 350 °C.

- *In situ* fourier transform infrared (FTIR) spectroscopy or simulated *operando* XPS experiments can potentially be conducted as well. The latter would involve exposing the catalyst to the reacting gas feed mixture for a fixed time and temperature at atmospheric pressure before transferring it into the XPS chamber for surface analysis. These techniques can potentially shed light on the formation of the different kinds of core-shell structures (if there are any) at various temperatures.

- Chemisorption studies on each of these catalysts can be performed at a state where a complete metallic outer-shell is thought to have formed (*i.e.,* where only methane is formed) to obtain a surface area. This surface can be compared to that of a fully reduced catalyst (of similar crystallite size). The surface areas in each case should be identical or very similar especially if there are no cobalt oxides (CoO or Co_3O_4) on the surface.

- The study of metal-support interactions can be extended to other Co_3O_4-based catalysts *i.e.,* Co_3O_4 nanoparticles supported on different conventional support materials (e.g. CeO_2, SiO_2, TiO_2 etc.). The strength of the interaction between the Co_3O_4 nanoparticles and support material in each case can be altered. Again, this could broaden our understanding of the effects of conventional supports on the CO-PROX activity and stability of Co_3O_4. This could also offer new ideas for developing novel support materials which could help enhance the activity of Co_3O_4 and also improve its resistance to reduction.

References

Adams, T. M. & Mickalonis, J. 2007. Hydrogen permeability of multiphase V-Ti-Ni metallic membranes. *Material Letters*. 61(3):817-820.

Adesina, A. A. 1996. Hydrocarbon synthesis via Fischer-Tropsch reaction: travails and triumphs. *Applied Catalysis A: General*. 138(2):345–367.

Adhikari, S. & Fernando, S. 2006. Hydrogen membrane separation techniques. *Industrial & Engineering Chemistry Research*. 45(3):875-881.

Anderson, R. B. 1984. *The Fischer-Tropsch Synthesis*. Academic Press, New York, USA.

Argyle, M. D. & Bartholomew, C. H. 2015. Heterogeneous catalyst deactivation and regeneration: A review. Catalysts. 5(1):145-269.

Armor, J. N. 1999. The multiple roles for catalysis in the production of H_2. *Applied Catalysis*. 176(2):159-176.

Arnoldy, P. & Moulijn, J. A. 1985. Temperature-programmed reduction of CoO/Al_2O_3 catalysts. *Journal of Catalysis*. 93(1):38-54.

Barbier, A., Hanif, A., Dalmon, J. –A. & Martin, G. A. 1998. Preparation and characterisation of well-dispersed and stable Co/SiO_2 catalysts using the ammonia method. *Applied Catalysis A: General*. 168(2):333-343.

Barbier, A., Martin, G. –A., de la Piscina, P. R. & Homs, N. 2001. Co/SiO_2 catalysts prepared from $Co_2(CO)_8$ for hydrogenation into alcohols and hydrocarbons: characterisation by magnetic methods and temperature-programmed hydrogenation. *Applied Catalysis A: General*. 210(1-2):75-81.

Bartholomew, C., Pannell, R., & Butler, J. 1980. Support and crystallite size effects in CO hydrogenation on nickel. *Journal of Catalysis*. 65(2):335-347.

Bean, C. P. & Livingston, J. D. 1959. Superparamagnetism. *Journal of Applied Physics*. 30:S120-S129.

Bergeret, G., and Gallezot, P. 1997. Particle size and dispersion measurements. In *Handbook of Heterogeneous Catalysis 2*. VCH, Weinheim, Federal Republic of Germany. 3:439-464.

Bion, N., Epron, F., Moreno, M., Mariño, F. & Duprez, D. 2008. Preferential oxidation of carbon monoxide in the presence of hydrogen (PROX) over noble metals and transition metal oxides: Advantages and drawbacks. *Topics in Catalysis*. 51(1-4):76–88.

Boubnov, A., Dahl, S., Johnson, E., Molina, A. P., Simonsen, S. B., Cano, F. M., Helveg, S. Lemus-Yegres, L. J. & Grunwaldt, J. –D. 2012. Structure-activity relationships of Pt/Al_2O_3 catalysts for CO and NO oxidation at diesel exhaust conditions. *Applied Catalysis B: Environmental*. 126():315-325.

Boutonnet, M., Logdberg, S. & Elm Svensson, E. 2008. Recent developments in the application of nanoparticles prepared from w/o microemulsions in heterogeneous catalysis. *Current Opinion in Colloid & Interface Science*. 13(4):270-286.

Broqvist, P., Panas, I. & Persson, H. 2002. A DFT study on CO oxidation over Co_3O_4. *Journal of Catalysis*. 210(1):198-206.

Brown Jr., M. L., Green, A. W., Cohn, G. & Andersen, H. C. 1960. Purifying hydrogen by selective oxidation of carbon monoxide. *Industrial and Engineering Chemistry*. 52(10):841-844.

Brown Jr., M. L. & Green, A. W. 1963. *U.S. Patent No. 3,088,919*.

Buffat, P. & Borel, J. –P. 1976. Size effect on the melting temperature of gold particles. *Physical Review A*. 13(6):2287-2298.

Buschow, K. H. J. 2001. *Encyclopedia of Materials: Science and Technology*. Vol. 5. Amsterdam, Netherlands: Elsevier. pp. 5021, Table 1.

Cargnello, M., Doan-Nguyen, V. V. T., Gordon, T. R., Diaz, R. E., Stach, E. A., Gorte, R. J., Fornasiero, P. & Murray, C. B. 2013. Control of metal size reveals metal-support interface role for ceria catalysts. *Science*. 341(6147):771-773.

Cheang, V. 2009. Effect of crystallite size and water partial pressure on the activity and selectivity of low temperature iron-based Fischer-Tropsch catalysts. Ph.D. Thesis. University of Cape Town, South Africa.

Cheney, B. A. 2010. Reverse micelle synthesis and characterisation of supported bimetallic catalysts. MSc. Dissertation. University of Delaware, United States of America.

Claeys, M., Dry, M. E., van Steen, E., van Perge, P. J., Booyens, S., Crous, R., van Helden, P., Labuschagne, J. *et al.* 2015. Impact of Process Conditions on the Sintering Behavior of an Alumina-Supported Cobalt Fischer–Tropsch Catalyst Studied with an *in situ* Magnetometer. *ACS Catalysis*. 5(2):841-852.

Claeys, M., van Steen, E., Visagie, J., & van de Loosdrecht, J. 2010. *Patent No. PCT patent WO 2010/004419 A2*.

Claeys, M. & Fischer, N. 2013. *Patent No. PCT patent WO2013/005180 A1*.

Clapham, B. 2012. The development of an *in situ* X-ray diffraction cell for Fischer-Tropsch catalyst characterisation. MSc(Eng) Dissertation. University of Cape Town, South Africa.

Cohn, J. G. E. 1965. *U.S. Patent No. 3,216,783*.

Cuenya, B. R. & Behafarid, F. 2015. Nanocatalysis: size- and shape-dependent chemisorption and catalytic activity. *Surface Science Reports*. 70(2):135-187.

Dalmon, J. 1994. Magnetic measurements and catalysis. In *Catalyst characterisation: Physical techniques for solid materials*. B. Imelik, B. & Verdrine, J., Eds. New York: Plenum Press. pp. 585

Danielsson, I. & Lindman, B. 1981. The definition of microemulsion. *Colloids and Surfaces*. 3(4):391-392.

Delmon, B. 2008. Formation of the final catalyst. In *Handbook of Heterogeneous Catalysis*. Ertl, G., Knözinger, H., Schüth, F., and Weitkamp, J., Eds. Weinheim, Germany. Vol 1.

Dry, M. E. 1981. *Catalysis Science and Technology*. Springer Verlag, New York, USA.

Eastoe, J., Hollamby, M., & Hudson, L. 2006. Recent advances in nanoparticle synthesis with reversed micelles. *Advances in Colloid and Interface Science*. 128-130, 5-15

Edwards, N., Ellis, S. R., Frost, J. C., Golunski, S. E., van Keulen, A. N. J., Lindewald, N. G. & Reinkingh, J. G. 1998. On-board hydrogen generation for transport applications: The HotSpot methanol processor. *Journal of Power Sources*. 71(1-2):123-128.

Eriksson, S., Nylen, U., Rojas, S. & Boutonnet, M. 2004. Preparation of catalysts from microemulsions and their applications in heterogeneous catalysis. *Applied Catalysis A: General*. 265(2):207-219.

Fischer, N. 2011. Preparation of nano- and Ångstrøm-sized cobalt ensembles and their performance in the Fischer-Tropsch synthesis. Ph.D. Thesis. University of Cape Town, South Africa.

Fischer, N., Clapham, B., Feltes, T., van Steen, E. & Claeys, M. 2014. Size-dependent phase transformation of catalytically active nanoparticles captured in-situ. *Angewandte Chemie International Edition*. 53(5):1342-1345

Fischer, N., Minnermann, M., Baeumer, M., van Steen, E. & Claeys, M. 2012. Metal-support interactions in Co_3O_4/Al_2O_3 catalysts prepared from w/o microemulsions. *Catalysis Letters*. 142(7):830-837.

Fischer, N., van Steen, E. & Claeys, M. 2011. Preparation of supported nano-sized cobalt oxide and fcc cobalt crystallites. *Catalysis Today*. 171(1):174-179.

Fu, L. and Bartholomew, C. H. 1985. Structure sensitivity and its effects on product distribution in CO hydrogenation on cobalt/alumina. *Journal of Catalysis*. 92(2):376–387.

Gamarra, D., Belver, C., Fernandez-Garcia, M. & Martinez-Arias. 2007. Selective CO oxidation in excess H_2 over copper-ceria catalysts: Identification of active entities/species. *Journal of the American Chemical Society*. 129(40):12064-12065.

Gawade, P., Bayram, B., Alexander, A. –M. C. & Ozkan, U. S. 2012. Preferential oxidation of CO (PROX) over CoO_x/CeO_2 in hydrogen-rich streams: Effect of cobalt loading. *Applied Catalysis B: Environmental*. 128:21-30.

Geus, J. & van Dillen, A. 2008. Supported catalysts. In *Handbook of Heterogeneous Catalysis*. Ertl, G., Knözinger, H., Schüth, F., and Weitkamp, J., Eds. Weinheim, Germany. Vol 1.

Ghenciu, A. F. 2002. Review of fuel processing catalysts for hydrogen production in PEM fuel cell systems. *Current Opinion in Solid State and Materials Science*. 6(5):389-399.

Golunski, S. 1998. HotSpot™ Fuel Processor: Advancing the case for fuel cell powered cars. *Platinum Metal Reviews*. 42(1):2-7.

Gray, P. G. & Petch, M. I. 2000. Advances with HotSpot™ Fuel Processing: Efficient hydrogen production for use with solid polymer fuel cells. *Platinum Metal Reviews*. 44(3):108-111.

Greenwood, N. N. & Earnshaw A. 1984. *Chemistry of the Elements*. Oxford, United Kingdom: Pergamon Press.

Guo, Q. & Liu, Y. 2007. Preferential oxidation of CO in H_2 over Co_3O_4-CeO_2 catalysts. *Reaction Kinetics and Catalysis Letters*. 92(1):19-25.

Herranz, T., Deng, X., Cabot, A., Guo, J. & Salmeron, M. 2009. Influence of cobalt particle size in the CO hydrogenation reaction studied by *in situ* X-ray absorption spectroscopy. *Journal of Physical Chemistry B*. 113(31):10721-10727.

Huang, S., Hara, K. & Fukuoka, A. 2009. Green catalysis for selective CO oxidation in hydrogen for fuel cell. *Energy and Environmental Science*. 2(10):1060-1068.

Iablokov, V. 2011. Manganese and cobalt oxides as highly active catalysts for CO oxidation. Ph.D. Thesis. Université Libre de Bruxelles, Belgium.

Jansson, J., Palmqvist, A. E. C., Fridell, E., Skoglundh, M., Osterlund, L., Thormahlen, P. & Langer, V. 2002. On the catalytic activity of Co_3O_4 in low-temperature CO oxidation. *Journal of Catalysis*. 211(2):387-397.

Jia, A. –P., Jiang, S. –Y., Lu, J. –Q. & Luo, M. –F. 2010. Study of catalytic activity at the CuO-CeO_2 interface for CO oxidation. *Journal of Physical Chemistry C*. 114(49):21605-21610.

Joo, S. H., Park, J. Y., Renzas, J. R., Butcher, D. R., Huang, W. & Somorjai, G. A. 2010. Size effect of ruthenium nanoparticles in catalytic carbon monoxide oxidation. *Nanoletters*. 10(7):2709-2713.

Kaneko, T., Derbyshire, F., Makino, E., Gray, D. & Tamura, M. 2001. Coal Liquefaction. In *Ullmann's Encyclopedia of Industrial Chemistry*. Wiley-VCH Verlag GmbH & Co. Germany: Weinheim. Vol. 9, pp. 311-389.

Kang, M., Song, M. W. & Lee, C. H. 2003. Catalytic carbon monoxide oxidation over CoO_x/CeO_2 composite catalysts. *Applied Catalysis A: General*. 251(1):143-156.

Kim, H. D. & Lim, M. S. 2002. Kinetics of selective CO oxidation in hydrogen-rich mixtures on Pt/alumina catalysts. *Applied Catalysis A: General*. 224(1-2):27-38

Kim, H. Y. & Henkelman, G. 2013. CO oxidation at the interface of Au nanoclusters and the stepped-CeO_2(111) surface by the Mars-van Krevelen mechanism. *Journal of Physical Chemistry Letters*. 4(1):216-221.

Kim, Y. H., Park, E. D., Lee, H. C., Lee, D. & Lee, K. H. 2009. Preferential CO oxidation over supported noble metal catalysts. *Catalysis Today*. 146(1-2):253-259.

Kim, Y. H., Park, E. J., Lee, H. C., Choi, S. H. & Park, E. D. 2012. Active size-controlled Ru catalysts for selective CO oxidation in H_2. *Applied Catalysis B: Environmental*. 127:129-136.

Kittel, C. 2005. *Introduction to Solid State Physics*. London: John Wiley & Sons, Inc.

Klier, J., Tucker, C. J., Kalantar, T. H. & Green, D. P. 2000. Properties and applications of microemulsions. *Advanced Materials*. 12(23):1751-1757

Ko, E.-Y., Park, E. D., Seo, K. W., Lee, H. C., Lee, D. & Kim, S. 2006. A comparative study of catalysts for the preferential CO oxidation in excess hydrogen. *Catalysis Today*. 116(3):377-383.

Lisiecki, I. & Pileni, M. P. 1993. Synthesis of copper metallic clusters using reverse micelles as microreactors. *Journal of the American Chemical Society*. 115(10):3887-3896.

Liu, C., Liu, Q., Bai, L., Dong, A., Liu, G. & Wen, S. 2013. Structure and catalytic performances of nanocrystalline Co_3O_4 catalysts for low temperature CO oxidation prepared by dry and wet synthetic routes. *Journal of Molecular Catalysis A: Chemical*. 370:1-6.

Luengnaruemitchai, A., Osuwan, S. & Gulari, E. 2004. Selective catalytic oxidation of CO in the presence of H_2 over gold catalyst. *International Journal of Hydrogen Energy*. 29(4):429-435.

Mabaso, E. I. 2005. Nanosized iron crystallites for Fischer-Tropsch synthesis. Ph.D. Thesis. University of Cape Town, South Africa.

Malwadkar, S., Bera, P., Hegde, M. S. & Satyanarayana, C. V. V. 2012. Preferential oxidation of CO on Ni/CeO_2 catalysts in the presence of excess H_2 and CO_2. *Reaction Kinetics, Mechanisms, and Catalysis*. 107(2):405-419.

Manaslip, A. & Gulari, E. 2002. Selective CO oxidation over Pt/alumina catalysts for fuel cell applications. *Applied Catalysis B: Environmental*. 37(1):17-25.

Mankidy, B. J., Balakrishnan, N., Joseph, B. & Gupta, V. K. 2014. CO oxidation by cobalt oxide: An experimental study on the relationship between nanoparticle size and reaction kinetic. *Austin Journal of Chemical Engineering*. 1(2):1-6.

Marbán, G., López, I. & Valdés-Solís, T. 2009. Preferential oxidation of CO by CuOx/CeO_2 nanocatalysts prepared by SACOP: Mechanisms of deactivation under the reactant stream. *Applied Catalysis A: General*. 361(1-2):160-169.

Marbán, G., López, I., Valdés-Solís, T. & Fuertes, A. B. 2008. Highly active structured catalyst made up of mesoporous Co_3O_4 nanowires supported on a metal wire mesh for the preferential oxidation of CO. *International Journal of Hydrogen Energy*. 33(22):6687-6695.

Marceau, E., Carrier, X., Che, M., Clause, O., & Marcilly, C. (2008). Ion exchange and impregnation. In *Handbook of Heterogeneous Catalysis*. Ertl, G., Knözinger, H., Schüth, F., and Weitkamp, J., Eds, Weinheim, Germany.

Mars, P. & van Krevelen, D. W. 1954. Oxidations carried out by means of vanadium oxide catalysts. *Chemical Engineering Science*. 3(Supplement 1):41-59

Mishra, A & Prasad, R. 2011. A review on preferential oxidation of carbon monoxide in hydrogen rich gases. *Bulletin of Chemical Reaction Engineering & Catalysis*. 6(1):1-14.

Molina, L. M. & Hammer, B. 2003. Active role of oxide support during CO oxidation at Au/MgO. *Physical Review Letters*. 90(20):206102(1)-206102(4)

Monyanon, S., Pongstabodee, S. & Luengnaruemitchai, A. Preferential oxidation of carbon monoxide over Pt, Au monometallic catalyst, and Pt-Au bimetallic catalyst supported on ceria in hydrogen-rich reformate. *Journal of the Chinese Institute of Chemical Engineers*. 38(5-6):435-441.

Moulijn, J. A., van Diepen, A. E. & Kapteijn, F. 2001. Catalyst deactivation: Is it predictable? What to do? *Applied Catalysis A: General*. 212(1-2):3-16.

Mousavand, T., Naka, T., Sato, K., Ohara, S., Umetsu, M., Takami, S., Nakane, T., Matsushita, A. & Adschiri, T. 2009. Crystal size and magnetic field effects in Co_3O_4 antiferromagnetic nanocrystals. *Physical Review B: Condensed Matter and Materials Physics*. 79(14):144411(1)-144411(5)

Naknam, P., Luengnaruemitchai, A., Wongkasemjit, S. & Osuwan, S. 2007. Preferential catalytic oxidation of carbon monoxide in the presence of hydrogen over bimetallic AuPt supported on zeolite catalysts. *Journal of Power Sources*. 165(1):353-358.

National Institute of Standards and Technology. 2013. Dataplot Reference Manual. Available: http://www.itl.nist.gov/div898/software/dataplot/refman2/ch2/homepage.htm. [Accessed on 5 March 2015].

Niu, H., Chen, Q., Zhu, H., Lin, Y. & Zhang, X. 2003. Magnetic field-induced growth and self-assembly of cobalt nanocrystallites. *Journal of Materials Chemistry*. 13(7):1803-1805.

Oh, S. H. & Sinkevitch, R. M. 1993. Carbon monoxide removal from hydrogen-rich fuel cell feedstreams by selective catalytic oxidation. *Journal of Catalysis*. 142(1):254-262.

Omata, K., Takada, T., Kasahara, S. & Yamada, M. 1996. Active site of substituted cobalt spinel oxide for selective oxidation of CO/H_2: Part II. *Applied Catalysis A: General*. 46(2):255-267.

Parinyaswan, A., Pongstabodee, S. & Luengnaruemitchai, A. 2006. Catalytic performances of Pt-Pd/CeO_2 catalysts for selective CO oxidation. *International Journal of Hydrogen Energy*. 31(13):1942-1949.

Park, J. –W., Jeong, J. –H., Yoon, W. –L., Jung, H., Lee, H. –T., Lee, D. –K., Park, Y. –K. & Rhee, Y. –W. 2004. Activity and characterisation of the Co-promoted CuO-CeO_2/γ-Al_2O_3 catalyst for the selective oxidation of CO in excess hydrogen. *Applied Catalysis A: General*. 274(1-2):25-32.

Park, E. D., Lee, D. & Lee, H. C. 2009. Recent progress in selective CO removal in a H_2-rich stream. *Catalysis Today*. 139(4):280-290.

Perry, R. H., Green, D. W. & Editors. 1997. *Perry's Chemical Engineers' Handbook*. 7th ed. New York City: McGraw-Hill.

Perti, D., Kabel, R. L. & McCarthy, G. J. 1985. Kinetics of CO oxidation over Co_3O_4/γ-Al_2O_3. *AIChE Journal*. 31(9):1435-1440

Rameswaran, M. & Bartholomew, C. H. 1989. Effects of preparation, dispersion, and extent of reduction on activity/selectivity properties of iron/alumina CO hydrogenation catalysts. *Journal of Catalysis*. 117(1):218–236.

Ratnasamy, P., Srinivas, D., Satyanarayana, C. V. V., Manikandan, P., Kumaran, R. S. S., Sachin, M. & Shetti, V. N. 2004. Influence of the support on the preferential oxidation of CO in hydrogen-rich steam reformates over the $CuO\text{-}CeO_2\text{-}ZrO_2$ system. *Journal of Catalysis*. 221(2):455-465.

Rehmat, A. & Randhava, S. S. 1970. Selective methanation of carbon monoxide. *Industrial & Engineering Chemistry Product Research and Development*. 9(4):512-515.

Reuel, R. C. & Bartholomew, C. H. 1984. Effects of support and dispersion on the CO hydrogenation activity/selectivity properties of cobalt. *Journal of Catalysis*. 85(1):78–88.

Rodrigues, A., Amphlett, J. C., Mann, R. F., Peppley, B. A. & Roberge, P. R. 1997. Carbon monoxide poisoning of proton-exchange membrane fuel cells. *Energy Conversion Engineering Conference, IECEC-97., Proceedings of the 32nd Intersociety*. 27 July – 1 August 1997. Honolulu, HI. Vol. 2, pp. 768-773.

Sadasivan, S., Bellabarba, R. M. & Tooze, R. P. 2013. Size-dependent reduction-oxidation-reduction behaviour of cobalt oxide nanocrystals. *Nanoscale*. 5(22):11139-11146.

Sakamoto, Y., Chen, F. L., Kinari, Y. & Sakamoto, F. 1996. Effect of carbon monoxide on hydrogen permeation in some palladium-based alloy membranes. *International Journal of Hydrogen Energy*. 21(11-12):1017-1024.

Scarlett, N. V. Y. & Madsen, I. C. 2006. Quantification of phases with partial or no known crystal structures. *Powder Diffraction*. 21(4):278-284.

Schueth, F., Hesse, M. & Unger, K. K. 2008. *Precipitation and coprecipitation*. Wiley-VCH Verlag GmbH & Co. Weinheim, Germany.

Schwuger, M. –J., Stickdorn, K. & Schomaecker, R. 1995. Microemulsions in technical processes. *Chemical Reviews*. 95(4):849-864.

Selwood, P. W. 1975. *Chemisorption and Magnetisation*. 2nd Ed., Academic, New York.

Sewell, G. S., van Steen, E. & O'Connor, C. T. 1996. Use of TPR/TPO for characterization of supported cobalt catalysts. *Catalysis Letters*. 37(3-4):255-260.

Serway, R., & Jewett, Jr., J. 2014. *Physics for Scientists and Engineers with Modern Physics*. Boston: Brooks/Cole.

Sircar, S., & Golden, T. C. 2009. Pressure Swing Adsorption Technology for Hydrogen Production. In *Hydrogen and Syngas Production and Purification Technologies*. Liu,

L., Song, C. & Subramani, V., Eds. Hoboken, New Jersey: John Wiley & Sons, Inc. Vol. 10, pp. 414-450.

Sirijaruphan, A., Horvath, A., Goodwin Jr., J. G. & Oukaci, R. 2003. Cobalt aluminate formation in alumina-supported cobalt catalysts: Effects of cobalt reduction state and water vapour. *Catalysis Letters*. 91(1-2):89-94.

Tang, C. -W., Wang, C. -B. & Chien, S. -H. 2008. Characterization of cobalt oxides studied by FT-IR, Raman, TPR and TG-MS. *Thermochimica Acta*. 473(1-2):68-73.

Teng, Y., Kusano, Y., Azuma, M., Haruta, M. & Shimakawa, Y. 2011. Morphology effects of Co_3O_4 nanocrystals catalysing CO oxidation in a dry reactant gas stream. *Catalysis Science & Technology*. 1(6):920-922.

Teng, Y., Sakurai, H., Ueda, A. & Kobayashi, T. 1999. Oxidative removal of CO in hydrogen by using metal oxide catalysts. *International Journal of Hydrogen Energy*. 24(4):355-358.

Todorova, S., Zhelyazkov, V. & Kadinov, G. 1996. IR, TPR and chemisorption study of alumina-supported cobalt catalysts. *Reaction Kinetics, Mechanisms and Catalysis*. 57(1):105-110.

Tuxen, A., Carenco, S., Chintapalli, M., Chuang, C. –H., Escudero, C., Pach, E., Jiang, P., Borondics, F. *et al.* 2013. Size-dependent dissociation of carbon monoxide on cobalt nanoparticles. *Journal of the American Chemical Society*. 135(6):2273-2278.

Valden, M., Pak, S., Lai, X. & Goodman, D. W. 1998. Structure sensitivity of CO oxidation over model Au/TiO_2 catalysts. *Catalysis Letters*. 56(1):7-10.

Van Steen, E. & Claeys, M. 2008. Fischer-Tropsch Catalysts for the Biomass-to-Liquid (BTL)-Process. *Chemical Engineering & Technology*. 31(5):655-666.

Varghese, S., Cutrufello, M.G., Rombi, E., Cannas, C., Monaci, R. & Ferino, I. 2012. CO oxidation and preferential oxidation of CO in the presence of hydrogen over SBA-15-templated $CuO\text{-}Co_3O_4$ catalysts. *Applied Catalysis A: General*. 443-444:161-170.

Vielstich, W., Lamm, A. & Gasteiger, H. A. 2003. *Handbook of Fuel Cells: Fundamentals, Technology and Applications*. Wiley. USA: New Jersey.

Wang, C. -B., Tang, C. -W., Gau, S. -J. & Chien, S. -H. 2005. Effect of the surface area of cobaltic oxide on carbon monoxide oxidation. *Catalysis Letters*. 101(1-2):59-63.

Wang, C. -B., Tang, C. -W., Tsai, H. -C. & Chien, S. -H. 2006. Characterization and catalytic oxidation of carbon monoxide over supported cobalt catalysts. *Catalysis Letters*. 107(3-4):223-230.

Wang, H. -F., Kavanagh, R., Guo, Y. -L., Guo, Y., Lu, G. & Hu, P. 2012. Origin of extraordinarily high catalytic activity of Co_3O_4 and its morphological chemistry for CO oxidation at low temperature. *Journal of Catalysis*. 296:110-119.

Watanabe, M. & Mooto, S. 1975. Electrocatalysis by ad-atoms: Part II. Enhancement of the oxidation of carbon monoxide on platinum by ruthenium ad-atoms. *Journal of Electroanalytical Chemistry and Interfacial Electrochemistry*. 60(3):275-283

Woods, M. P., Gawade, P., Tan, B. & Ozkan, U. S. 2010. Preferential oxidation of carbon monoxide on Co/CeO_2 nanoparticles. *Applied Catalysis B: Environmental*. 97(1-2):28-35.

Wootsch, A., Descorme, C. & Duprez, D. 2004. Preferential oxidation of carbon monoxide in the presence of hydrogen (PROX) over ceria–zirconia and alumina-supported Pt catalysts. *Journal of Catalysis*. 225(2):259-266.

Yajima, T., Uchida, H. & Watanabe, M. 2004. In-Situ ATR-FTIR spectroscopic study of electro-oxidation of methanol and adsorbed CO at Pt-Ru alloy. *Journal of Physical Chemistry B*. 108(8):2654-2659.

Yan, J., Ma, J., Cao, P. & Li, P. 2004. Preferential oxidation of CO in H_2-rich gases over Co-promoted Pt-γ-Al_2O_3 catalyst. *Catalysis Letters*. 93(1-2):55-60.

Yung, M. M., Zhao, Z., Woods, M. P. & Ozkan, U. S. 2008. Preferential oxidation of carbon monoxide on CoO_x/ZrO_2. *Journal of Molecular Catalysis A: Chemical*. 279(1):1-9.

Zeng, S., Liu, K., Zhang, L., Qin, B., Chen, T., Yin, Y. & Su, H. 2014. Deactivation analyses of CeO_2/CuO catalysts in the preferential oxidation of carbon monoxide. *Journal of Power Sources*. 261:46-54.

Zhao, Z., Lin, X., Jin, R., Dai, Y. & Wang, G. 2011. High catalytic activity in CO PROX reaction of low cobalt-oxide loading catalysts supported on nano-particulate CeO_2-ZrO_2 oxides. *Catalysis Communications*. 12(15):1448-1451.

Zhao, Z., Yung, M. & Ozkan, U. S. 2008. Effect of support on the preferential oxidation of CO over cobalt catalysts. *Catalysis Communications*. 9(6):1465-1471.

Appendices

Appendix A: Magnetometer calibration and calculation of the degree of reduction

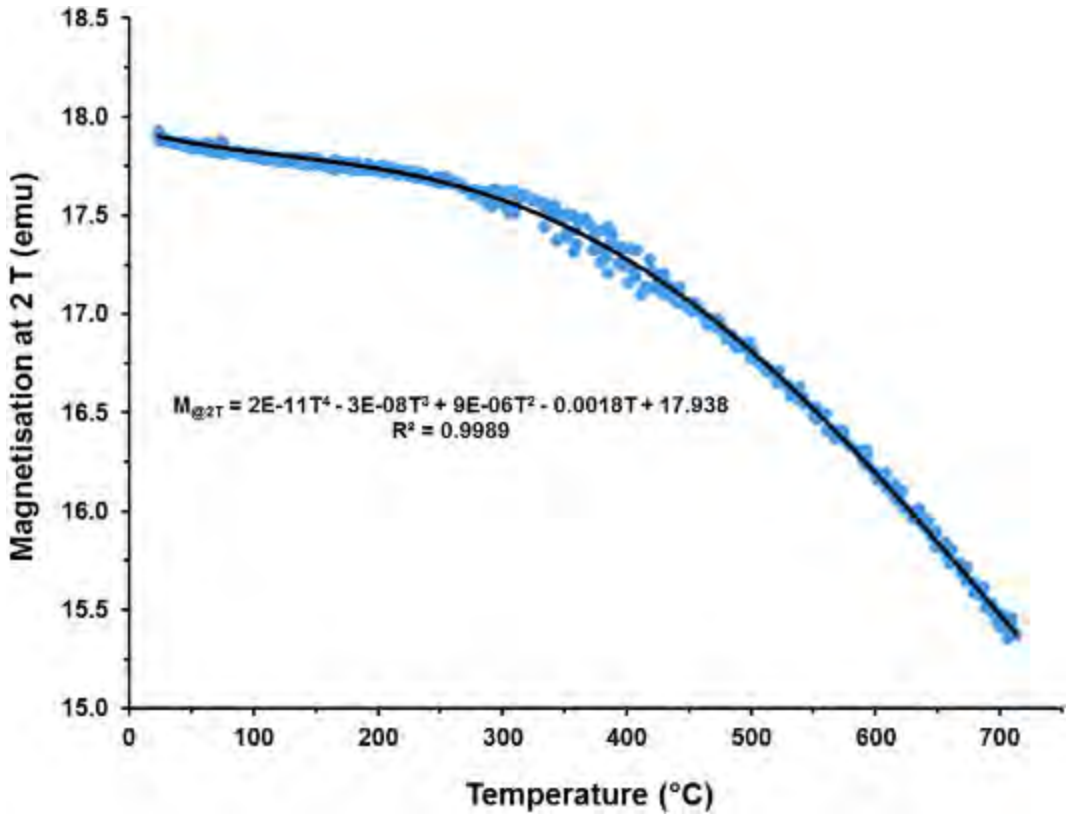

Figure A.1: *Sample magnetisation of a 0.1 g metallic cobalt sample as a function of temperature.*

To calculate the amount of metallic cobalt formed and the degree of reduction, Equations A.1 and A.2 shown on the next page were used.

$$m_{Co\ formed}\ (g) = \frac{M_{experimental} \cdot 0.1\ g}{M_{calibration}} \qquad \textbf{Equation A. 1}$$

$$\textbf{Degree of reduction}\ (\%) = \frac{m_{Co\ formed}}{0.73 \cdot m_{Co_3O_4\ loaded}} \times 100 \qquad \textbf{Equation A. 2}$$

Where $m_{Co\ formed}$ is the mass of cobalt formed at temperature T_i. $M_{experimental}$ is the sample magnetisation measured at temperature T_i during the CO-PROX experiment and $M_{calibration}$ is the magnetisation measured at temperature T_i during the calibration of the magnetometer with a 0.1 g metallic cobalt sample. $m_{Co_3O_4\ loaded}$ is the initial Co_3O_4 loading as determined by EDX.

Appendix B: Gas calibration

Table B.1: *GC-TCD gas calibration results.*

Gas component, i	Volume fraction (%)	TCD peak area (a.u.)			Average peak area (a.u.)	Response factor, F_i
		1	2	3		
N_2 (cylinder 1)	5.2	85.5	85.4	85.2	85.4	1.000
CO	20.1	332	332.4	332.3	332.2	0.993
CO_2	9.8	978.6	978.7	977.8	978.4	0.164
CH_4	15.2	220.4	220.6	220.3	220.4	1.132
H_2	39.6	41342.1	41368.8	41342.3	41351.1	0.0156
Ar	10.1	-	-	-	-	-
N_2 (cylinder 2)	79.0	1165.8	1166.5	1164	1165.4	1.000
O_2	21.0	296.8	297.2	296.8	296.9	1.043

$$F_i = \frac{A_{N_2} n_{i,in}}{A_i n_{N_2,in}} \qquad \textbf{Equation B. 1}$$

Where $\boldsymbol{F_i}$ is the response factor of gas component $\boldsymbol{i}$ with reference to nitrogen. $\boldsymbol{A_{N_2}}$ is the calculated peak area of nitrogen and $\boldsymbol{A_i}$ is the calculated peak area of gas component $\boldsymbol{i}$. The variable $\boldsymbol{n_{N_2,in}}$ is the molar gas flow rate of nitrogen and $\boldsymbol{n_{i,in}}$ is the molar gas flow rate of gas component $\boldsymbol{i}$ entering the system during the calibrations.

Appendix C: TEM micrographs of fresh and spent catalysts

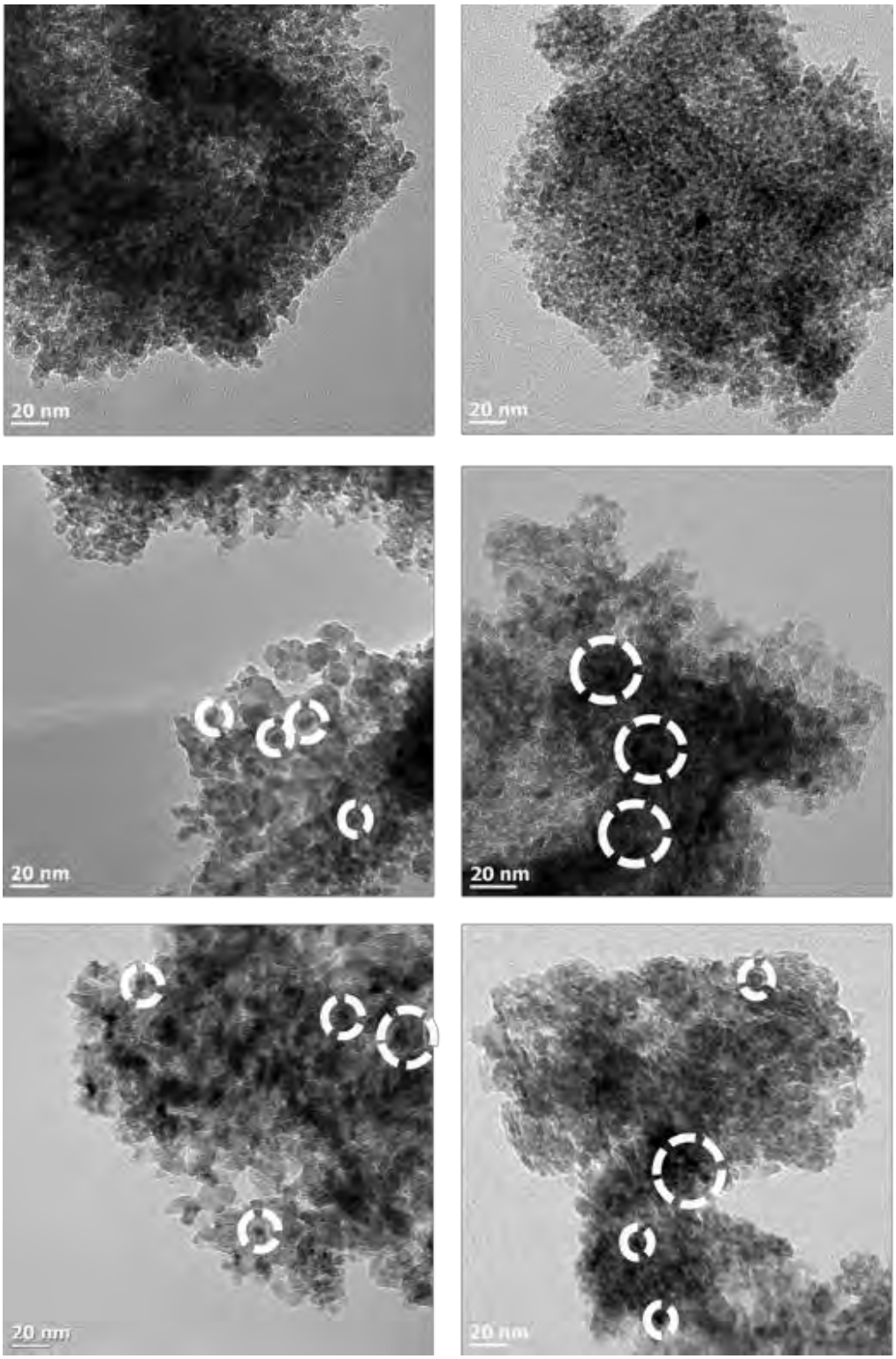

Figure C.1: *TEM micrographs of the fresh samples of (**top-left**) TN_02 and (**top-right**) TN_04 in the unsupported state, (**middle-left**) TN_02 and (**middle-right**) TN_04 in the supported state as well as the spent samples of (**bottom-left**) TN_02 and (**bottom-right**) TN_04.*

Appendix D: Catalytic evaluation results

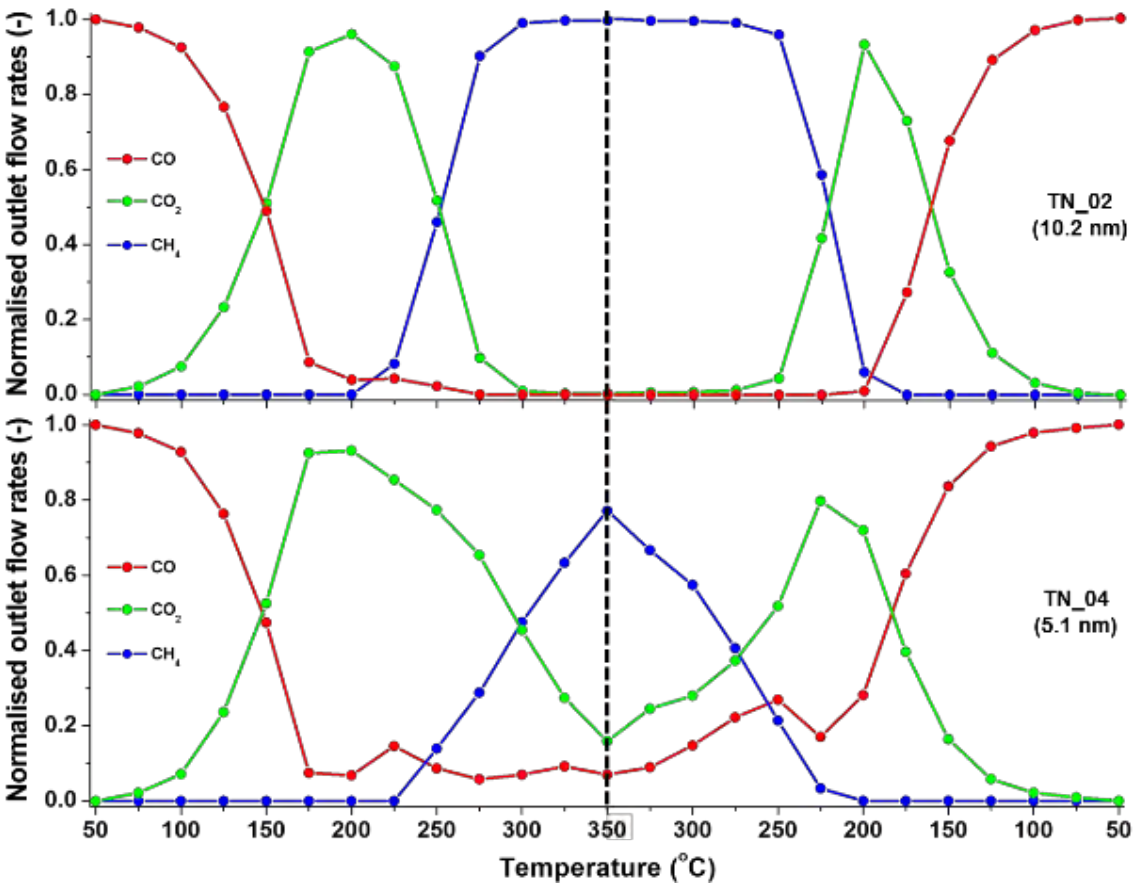

Figure D.1: *Normalised outlet flow rates of CO, CO_2 & CH_4 as a function of temperature for (**top**) TN_02 and TN_04 (**bottom**).*

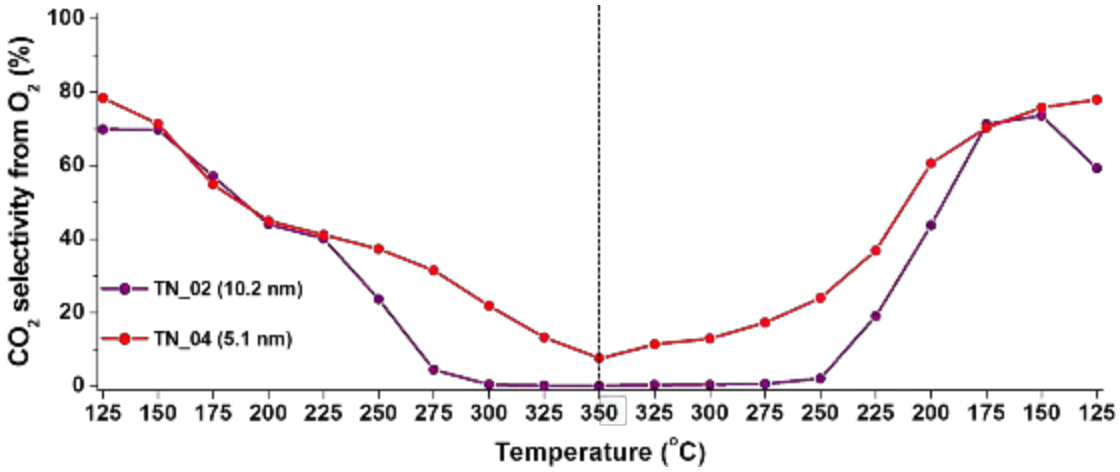

Figure D.2: *CO_2 selectivity based on the conversion of O_2 as a function of temperature for the catalysts TN_02 and TN_04.*

Appendix E: Hysteresis measurements

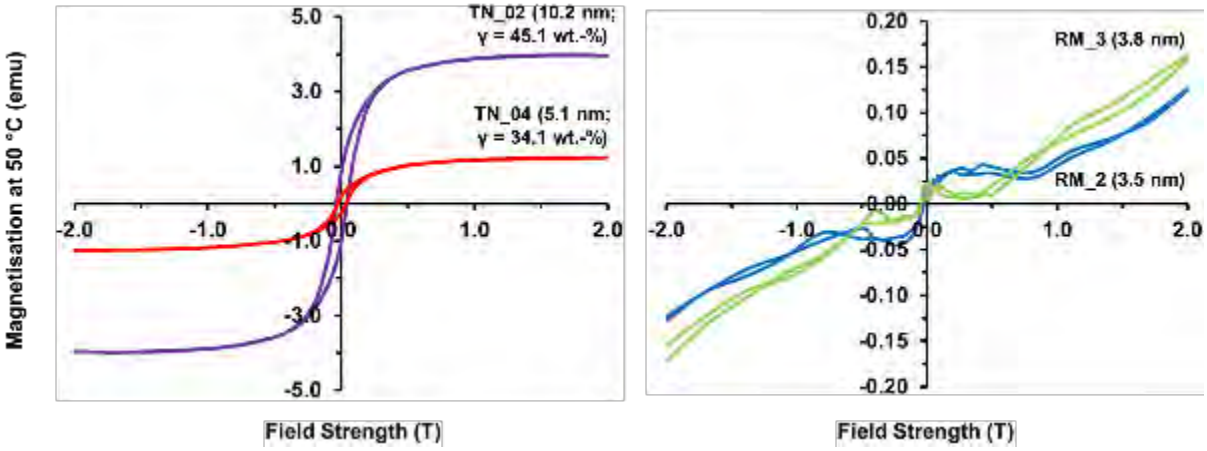

Figure E.1: *Sample magnetisation as a function of the external field at 50 °C for (**left**) TN_02 & TN_04 and also for (**right**) RM_2 & RM_3. For TN_02 and TN_04, the amount of material displaying remnant magnetisation (γ, in wt.-%) is shown in brackets on the figure. RM_2 and RM_3 did not reduce and so no remnant magnetisation could be measured for these two samples.*

Appendix F: *In situ* PXRD patterns

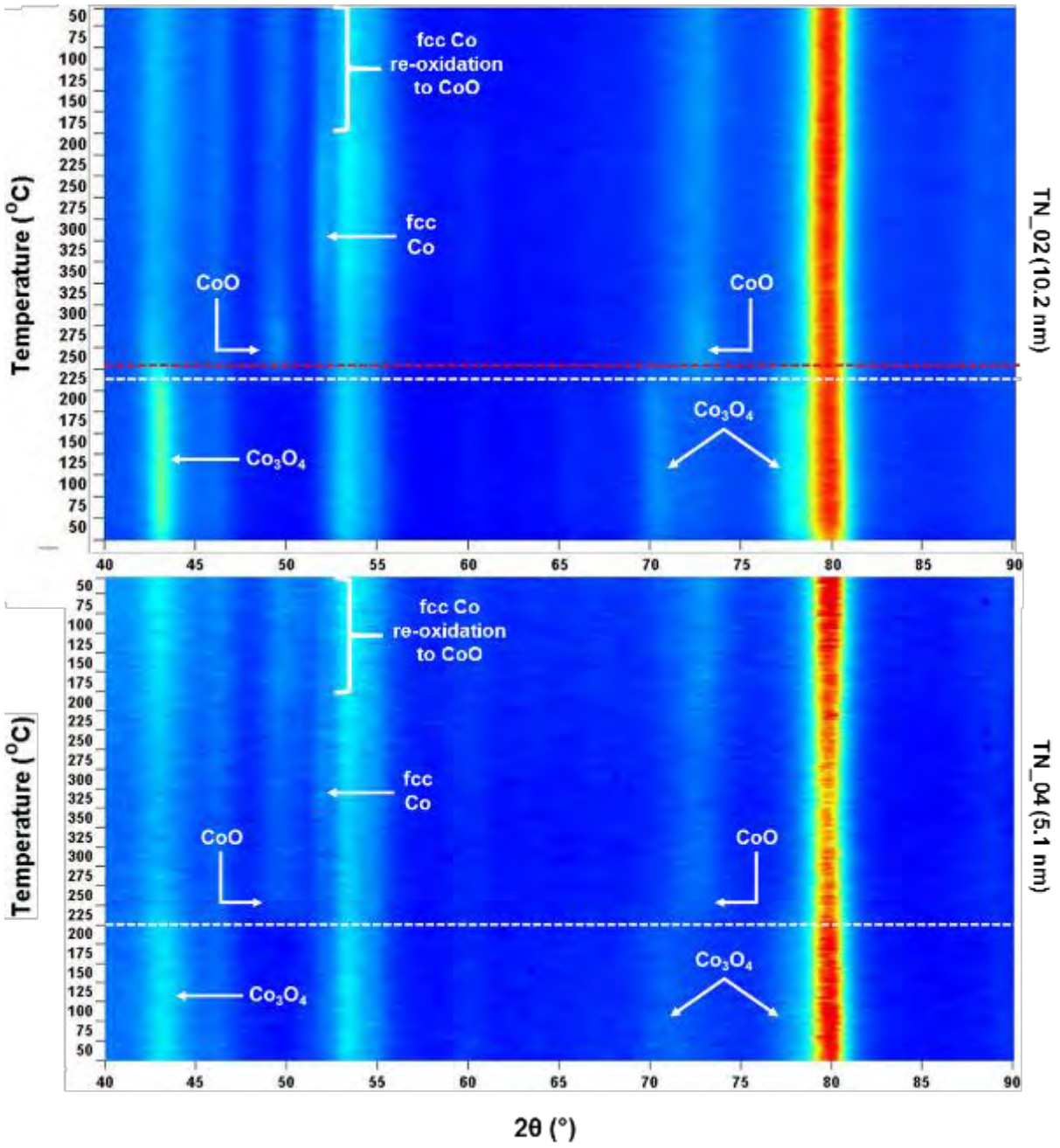

Figure F.1: *On-top view of the in situ PXRD patterns recorded for* ***(top)*** *TN_02 and* ***(bottom)*** *TN_04 as function of temperature. The white and red dotted lines indicate the temperature at which the CoO and fcc Co phases were first observed, respectively.*

Appendix G: Calculation of the surface area-specific formation rates

Region 1, where there were Co_3O_4 crystallites, the CO_2 surface area-specific formation rates were calculated as follows:

$$\boldsymbol{CO_2\ surface\ formation\ rate}\left(\boldsymbol{molec_{CO_2}.nm^{-2}.s^{-1}}\right) = \frac{\boldsymbol{n_{CO_2,\,out}\cdot N_A}}{\boldsymbol{\pi\cdot D^2\cdot N_{Co_3O_4\ crystallites}}} \qquad \textbf{Equation G. 1}$$

Where $\boldsymbol{n_{CO_2,out}}$ is the molar flow rate of CO_2 exiting the reactor (in $mol.s^{-1}$), $\boldsymbol{N_A}$ is Avogadro's number (in molecules per mole), $\boldsymbol{D}$ is the average TEM number-based crystallite size assuming no or negligible sintering (in nm) and $\boldsymbol{N_{Co_3O_4\ crystallites}}$ is the number of Co_3O_4 crystallites in the sample calculated using Equation G.2:

$$\boldsymbol{N_{Co_3O_4\ crystallites}} = \frac{\boldsymbol{6\cdot M_{Co_3O_4\ loaded}}}{\boldsymbol{\rho_{Co_3O_4}\cdot\pi\cdot D^3}} \qquad \textbf{Equation G. 2}$$

Where $\boldsymbol{M_{Co_3O_4\ loaded}}$ is the mass of Co_3O_4 present in the sample as determined with EDX (in g) and $\boldsymbol{\rho_{Co_3O_4}}$ is the density of Co_3O_4 (in $g.nm^{-3}$).

Region 2, where the crystallites are thought to have a single-shell structure (as shown in Figure G.1), the methane surface area-specific formation rates were calculated using Equation G.3:

Figure G.1: *(**left**) Single-shell crystallite with a (**right**) metallic Co shell of thickness "**t**" and a CoO core of diameter "**d**". The whole crystallite has the diameter "**D**". (Note: **D = d + 2t**). The thickness of the shell is directly related to the degree of reduction*

$$\boldsymbol{CH_4\ surface\ formation\ rate}\left(\boldsymbol{molec_{CH_4}.nm^{-2}.s^{-1}}\right) = \frac{\boldsymbol{n_{CH_4,\,out}\cdot N_A}}{\boldsymbol{\pi\cdot D^2\cdot N_{crystallites}}} \qquad \textbf{Equation G. 3}$$

Where $\boldsymbol{n_{CH_4,out}}$ is the molar flow rate of CH_4 exiting the reactor (in $mol.s^{-1}$) and $\boldsymbol{D}$ is the theoretical average diameter of the single-shell crystallites calculated using Equation G.4 (in nm). The calculated diameter for each catalyst is shown in Table G.1 together with the thickness of the metallic Co shell. $\boldsymbol{N_{crystallites}}$ is the number of these single-shell crystallites in the sample which is equal to $\boldsymbol{N_{Co_3O_4\ crystallites}}$ assuming no or negligible sintering.

$$\boldsymbol{D\ (nm)} = \sqrt[3]{\frac{\boldsymbol{6}}{\boldsymbol{\pi}}\cdot\left(\frac{\boldsymbol{m_{Co\ crystallite}}}{\boldsymbol{\rho_{Co}}}+\frac{\boldsymbol{m_{CoO\ crystallite}}}{\boldsymbol{\rho_{CoO}}}\right)} \qquad \textbf{Equation G. 4}$$

Where $\boldsymbol{m_{Co\ crystallite}}$ is the mass of Co present in a single crystallite and $\boldsymbol{m_{CoO\ crystallite}}$ is the mass of CoO present in a single particle as determined. $\boldsymbol{m_{Co\ crystallite}}$ can be directly related to the degree of reduction obtained during the magnetic studies.

Table G.1: *Theoretical average diameters of the single shell-structured crystallites and the thickness of the metallic Co shell in each catalyst.*

Sample Names	Theoretical diameters of crystallites (nm): REGION 2	Theoretical thickness of outer metallic Co shell (nm): REGION 2
TN_01	8.96	0.60
TN_02	7.54	0.50
TN_03	5.70	0.11
TN_04	3.55	0.07
TN_05	3.06	0.08

Region 3, where the crystallites are thought to have a double-shell structure as shown in Figure G.2, the CO_2 surface area-specific formation rates were calculated using Equation G.5:

Figure G.2: *(**left**) Double-shell crystallite with a (**right**) CoO outer-shell of thickness "**t_2**", a metallic Co inner-shell of thickness "**t_1**" and a CoO core of diameter "**d**". The whole double-shell crystallite has the diameter "**D**". (Note: **$D = d + 2t_1 + 2t_2$**). The thickness of the two shells is directly related to the degree of re-oxidation.*

$$\boldsymbol{CO_2\ surface\ formation\ rate}\left(molec_{CO_2}.nm^{-2}.s^{-1}\right) = \frac{n_{CO_2,\,out}\cdot N_A}{\pi\cdot D^2\cdot N_{crystallites}} \qquad \textbf{Equation G. 5}$$

Where ***D*** is the theoretical average diameter of these double shell-structured crystallites calculated using Equation G.4 (in nm). The calculated diameter for each catalyst is shown in

Table G.2 together with the thickness of the metallic Co inner-shell and CoO outer shell, respectively. $\boldsymbol{N_{crystallites}}$ is the number of these double-shell crystallites in the sample which is equal to $\boldsymbol{N_{Co_3O_4\ crystallites}}$ assuming no or negligible sintering.

Table G.2: *Theoretical diameters of the double shell-structured crystallites and the thickness of the metallic Co inner-shell and CoO outer-shell, respectively, in each catalyst.*

Sample Names	Theoretical diameters of crystallites (nm): REGION 3	Theoretical thickness of inner metallic Co shell (nm): REGION 3	Theoretical thickness of outer CoO shell (nm): REGION 3
TN_01	9.15	0.48	0.23
TN_02	7.69	0.41	0.18
TN_03	5.74	0.08	0.05
TN_04	3.59	0.05	0.04
TN_05	3.08	0.06	0.02

Appendix H: *Ex situ* PXRD patterns of fresh and spent catalysts

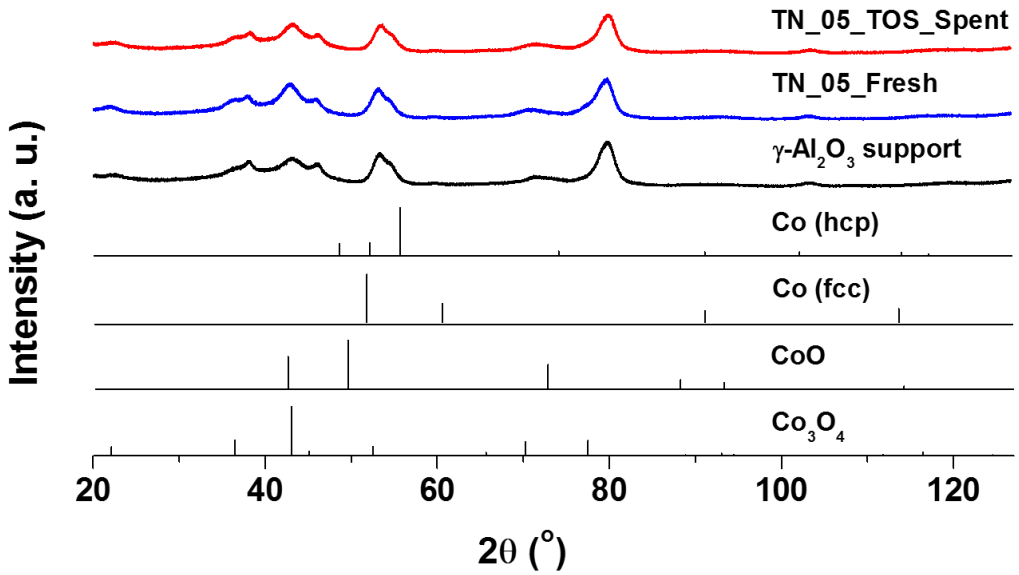

Figure H.1: *PXRD spectrum of the spent catalyst sample of TN_05 obtained after performing the time-on-stream (TOS) experiment. The spectrum of the fresh sample of TN_05 is also included for comparison.*